Assimilating a Higher Fidelity Representation of Wave Energy Converters in a Spectral Model

by

Ewelina Luczko
B. A. Sc, University of Waterloo, 2014

A Thesis Submitted in Partial Fulfillment
of the Requirements for the Degree of

MASTERS OF APPLIED SCIENCE

in the Department of Mechanical Engineering

Assimilating a Higher Fidelity Representation of
Wave Energy Converters in a Spectral Model

by

Ewelina Luczko
B. A. Sc., University of Waterloo, 2014

Supervisory Committee

Dr. Bradley Buckham, Department of Mechanical Engineering

Supervisor

Dr. Henning Struchtrup, Department of Mechanical Engineering

Departmental Member

Abstract

Supervisory Committee

Dr. Bradley Buckham

Supervisor

Dr. Henning Struchtrup

Departmental Member

To accommodate future power demands, wave energy converters will be deployed in arrays, but largely unanswered questions of the annual energy production and environmental impact of such installations present regulatory dilemmas. In recent years, Sandia National Laboratories (SNL) has developed a modified version of the Simulating Waves Nearshore (SWAN) wave model to simulate WEC energy extraction in a propagating wave field. This thesis presents a novel WEC meta-model that calculates the power intercepted by a WEC from the incident wave field. Two representations were developed with which a user could model a WEC's impact on the incident waves in a spectral wave model. These alterations are based on power a WEC captures from the sea and power dissipated by hydrodynamic losses calculated in an external six degree of freedom (DOF) time domain WEC simulation.

The two WEC meta-models were compared in terms of significant wave height reduction in the WEC's lee and annual power production. The first WEC representation removes a constant percentage of power from each frequency bin while the second representation employs frequency dependent energy extraction. The representations were then applied in modelling a 54 MW WEC array off of Amphitrite Bank on the West Coast of Vancouver Island. Over the course of a year, the power captured by a farm when represented with a constant percentage extraction is reduced by 2.9% while a frequency dependent percentage extraction reduced the farm's total captured power by 2.3% when compared to the reference case. Similarly small changes were observed in significant wave height reductions. The significant wave height in the lee of a farm was reduced by less than 2% for both representations at the shoreline, approximately six kilometres behind the farm.

Table of Contents

List of Tables

List of Figures

Acknowledgments

I would like to thank everyone who helped me along the long and arduous journey of conducting a Master's thesis. A special thank you to Dr. Buckham who managed to miraculously finish every meeting on a positive note, Clayton Hiles who helped me overcome the learning curve in coastal modelling, Dr. Bailey: the patient and insightful hydrodynamics wizard, and finally Dr. Robertson: who provided insight when analyzing results as well as when analyzing my bike and finally Barry Kent for all his time and IT expertise. This work would not have been possible without the professional and personal support from my brilliant colleagues at WCWI.

On a personal note I would like to thank my parents, my kind and considerate roommates and friends both at UVic and far away. You have been instrumental in helping me maintain my sanity and motivational when inevitably in research, problems arose.

This research would not have been possible without the financial assistance of Natural Resources Canada, the Pacific Institute of Climate Solutions, the Natural Sciences and Research Council of Canada, and contributions from Cascadia Coast Research Ltd and the computational resources from Ocean Networks Canada.

Dedication

To those who showed me great kindness over the course of this journey.

Nomenclature

Symbol		Definition	Units
A	=	wave amplitude	m
$A(\infty)$	=	added mass at infinite frequency	kg
A_{proj}	=	projected area	m^2
C	=	hydrodynamic stiffness	$\mathrm{kg} \cdot \mathrm{s}^{-2}$
C_d	=	drag coefficient	
$C_{p,d}$	=	Internal drag coefficient	
c_g	=	group velocity	$\mathrm{m} \cdot \mathrm{s}^{-1}$
c_x	=	propagation velocity in spatial x space	$\mathrm{m} \cdot \mathrm{s}^{-1}$
c_y	=	propagation velocity in spatial y space	$\mathrm{m} \cdot \mathrm{s}^{-1}$
c_θ	=	propagation velocity in spectral directional space	$\mathrm{m} \cdot \mathrm{s}^{-1}$
c_σ	=	propagation velocity in spectral frequency space	$\mathrm{m} \cdot \mathrm{s}^{-1}$
d	=	water depth	m
E	=	energy density	$\mathrm{J} \cdot \mathrm{s}$
E_v	=	variance density	$\mathrm{m}^2 \cdot \mathrm{s}$
f	=	frequency	s^{-1}
f_p	=	peak frequency	s^{-1}
F_E	=	excitation force	$\mathrm{kg} \cdot \mathrm{m} \cdot \mathrm{s}^{-2}$
F_{ir}	=	internal reaction force induced by the second body on the first	$\mathrm{kg} \cdot \mathrm{m} \cdot \mathrm{s}^{-2}$
F_m	=	damping force induced by the moorings	$\mathrm{kg} \cdot \mathrm{m} \cdot \mathrm{s}^{-2}$
F_{PTO}	=	damping force induced by the power take-off	$\mathrm{kg} \cdot \mathrm{m} \cdot \mathrm{s}^{-2}$
F_v	=	damping force induced by viscous drag	$\mathrm{kg} \cdot \mathrm{m} \cdot \mathrm{s}^{-2}$
g	=	gravitational constant	$\mathrm{m} \cdot \mathrm{s}^{-2}$
H_s	=	significant wave height	m
i	=	index for the number of frequency bins	
j	=	index for the number of directional bins	

J	=	wave energy transport	$\mathrm{W} \cdot \mathrm{m}^{-1}$
k	=	Wavenumber	
$k(t-\tau)$	=	Impulse response kernel	
K_r	=	radiation coefficient	
K_t	=	transmission coefficient	
L	=	wavelength	m
m_n	=	spectral moment of the n^{th} order	
M	=	Mass	kg
N	=	action density	$\mathrm{J} \cdot \mathrm{s}^2$
n	=	normal vector to the surface	
p	=	pressure	
P_{Abs}	=	power absorbed by a wave energy converter	W
P_{CAP}	=	power captured by a wave energy converter	W
$P_{drag,im}$	=	power associated with drag inducing motion	W
$P_{drag,rm}$	=	power associated with drag resisting motion	W
$\overline{P_I}$	=	total power incident to the wave energy converter	W
P_{INC}	=	power available to a wave energy converter	W
P_{moor}	=	power dissipated due to the mooring	W
P_{LEE}	=	power in the lee of a wave energy converter	W
$\overline{P_R}$	=	total power radiated by the wave energy converter	W
P_{RAD}	=	power transfer due to radiation	W
Q	=	number of frequency bins	
S	=	source terms	$\mathrm{m}^2 \cdot \mathrm{s} \cdot \mathrm{rad}^{-1}$
S_{bf}	=	wave decay due to bottom friction	$\mathrm{m}^2 \cdot \mathrm{s} \cdot \mathrm{rad}^{-1}$
S_{db}	=	wave decay due to depth induced breaking	$\mathrm{m}^2 \cdot \mathrm{s} \cdot \mathrm{rad}^{-1}$
S_{nl3}	=	triad wave interactions	$\mathrm{m}^2 \cdot \mathrm{s} \cdot \mathrm{rad}^{-1}$
S_{nl4}	=	quadruplet wave interactions	$\mathrm{m}^2 \cdot \mathrm{s} \cdot \mathrm{rad}^{-1}$
S_w	=	wave growth by wind	$\mathrm{m}^2 \cdot \mathrm{s} \cdot \mathrm{rad}^{-1}$
S_{wc}	=	wave decay due to whitecapping	$\mathrm{m}^2 \cdot \mathrm{s} \cdot \mathrm{rad}^{-1}$

t	=	time	s
T	=	wave period	s
T_p	=	peak period	s
x	=	state of the wave energy converter	m
x_c	=	spatial co-ordinate	m
y_c	=	spatial co-ordinate	m
γ_{rad}	=	percentage of radiated power exerted in front of the wave energy converter	
η	=	surface displacement	m
ω	=	angular wave frequency	radians
θ_h	=	wave heading (direction)	radians
$\kappa_{t,inc}$	=	intermediate transmission coefficient	
$\kappa_{t,rad}$	=	intermediate radiation coefficient	
ρ	=	water density	$\mathrm{kg} \cdot \mathrm{m}^{-3}$
ϕ	=	wave offset (phase)	radians

Acronyms

AEP	Annual Energy Production
BBDB	Backwards Bent Duct Buoy
BEM	Boundary Element Model
COAMPS	Coupled Ocean/ Atmosphere Mesoscale Prediction System
DHI	Danish Hydraulic Institute
DOE	Department of Energy
DOF	Degrees of Freedom
ECMWF	European Center for Medium Range Weather Forecasts
LIMPET	Land Installed Marine Power Energy Transformer
OWC	Oscillating Water Column
PTO	Power take-off
RCW	Relative Capture Width
RMP	Reference Model Project
SNL	Sandia National Labs
SWAN	Simulating waves nearshore
VFD	Variable frequency drive
WCVI	West Coast of Vancouver Island
WEC	Wave Energy Converter

Chapter 1

Introduction

Humanity has conceived of a number of ways to harness kinetic energy from ocean waves, currents and tides. Marine hydrokinetic technologies extract power from bodies of water in motion – be it the bidirectional flow of tides, the unidirectional flow of a river, or the oscillating fluid flows within waves. Of the various hydrokinetic devices, wave energy converters (**WEC**s) present a promising pathway towards commercial scale clean energy generation since the raw resource has a high energy flux and is relatively insensitive to short term fluctuations in local weather patterns [1]. Energy flux is defined as the average power per meter crest length of wave and is thus usually reported in watts per meter. When energy reaches certain coastlines the average energy flux can be as igh as 100 kW/m [2]. Wave energy also tends to follow seasonal trends in energy consumption: wave energy supply increases in the winter when demands grow [3]. As such, there is hope that WEC supplied power could be integrated with greater ease than wind or solar power [3].

Waves, generated by the resonance between wind-induced pressure waves at the surface of the water, evolve over time and space [4]. Energy is exchanged between individual waves of different frequencies as a group of waves propagates across ocean basins. These small interactions consolidate propagating energy into low frequency, long wavelength ocean waves called swell that are a vast and largely untapped energy resource. The global

potential of ocean swell has been estimated at over two terawatts (TW), of which 4.6% is believed to be extractable [5].

1.1 Background

The wave energy sector's development as a whole can be categorized into two main stages. The first, pre-commercial stage involves the development of an efficient and robust WEC design concept. A single WEC however, will not be sufficient to meet growing electricity demands in the coming years on heavily populated coastlines. As such, the second, commercial stage of the wave energy sector's development concerns arrays. These two stages will be discussed in the remainder of this section.

1.1.1 Wave Energy Converter Development

The concept of harvesting ocean energy is not novel by any means. Thousands of WEC concepts have been patented to date with initial designs being presented as early as 1799 [6]. Figure 1 and Figure 2 demonstrate how WEC companies are presently employing the same design principles that were proposed by individuals in the early 20th century.

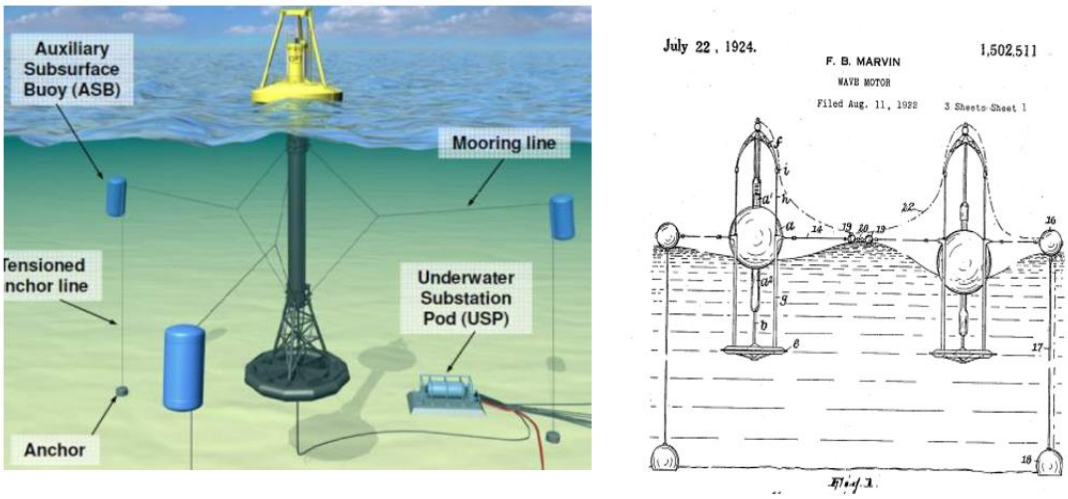

Figure 1: Schematic of a point absorber WEC[1] and a 1924 WEC patent [7] based on the same operating principle of generating power from the relative heaving motions of two floating bodies.

In 1924, Marvin proposed a surface piercing device comprised of a stator and a float, which can be seen on the right hand side of Figure 1. As the device is excited by a wave, the float moves freely along the stator. This relative heaving motion between the two

[1] Ocean Power Technologies: http://www.oceanpowertechnologies.com/powerbuoy/ Last Accessed: 18/07/16

bodies is used to derive useful power [7]. Ocean Power Technology's device harnesses power from the same relative motion of the float and spar (stator) described by Marvin. The similarities between these two designs even extend as far as the bottom mounted heave plates and the envisioned mooring configuration where both devices' spars are attached to adjacent subsurface floats that are then moored to the seabed.

In Figure 2, the Pelamis[2] device is compared to Nelson's 1912 wave motor in which floats are connected in series. As a wave propagates beneath the device, the floats' positions change relative to one another. Hydraulic cylinders installed at the hinge points of connected floats push and pull, compressing a fluid at high pressure driving a pump (in the case of Nelson's design), or hydraulic fluid which is accumulated to drive a hydraulic motor (in Pelamis'case).

In the technical sphere of wave energy conversion, convergence onto a single preferred design that is cost-effective, efficient over a range of excitation frequencies, capable of withstanding extreme weather conditions and able to generate power with utility grade quality has not yet occurred [6], [8].

Before the global threats of escalating carbon emissions and degrading air quality became apparent, fossil fuels were a paragon source of power. These fuels are flexible, reliable and energy dense creating little incentive to invest in the development of alternative power. As global temperatures rise due to anthropogenic causes, researchers and industry alike are working to make renewables a competitive alternative. The field of wave energy conversion is no exception, with government funded research and development programs[3] and competitions[4,5], there is a possibility the wave energy community will converge on a single, effective design. Alternatively, an assortment of devices may become industry standards given the number of phenomenon that can drive a mechanical energy conversion system and the range of suitable depths a device could operate in.

---

[2] Pelamis Wave Power Ltd., presently under the administration of Wave Energy Scotland http://www.hie.co.uk/growth-sectors/energy/wave-energy-scotland/default.html Last Accessed: 18/07/16

[3] Department of Energy Water Power Program: http://energy.gov/eere/water/water-power-program Last accessed: 07/18/16

[4] US Department of Energy's Wave Energy Prize: http://waveenergyprize.org/ Last accessed: 07/18/16

[5] Scotland's Saltire Prize: http://www.saltireprize.com/ Last accessed: 07/18/16

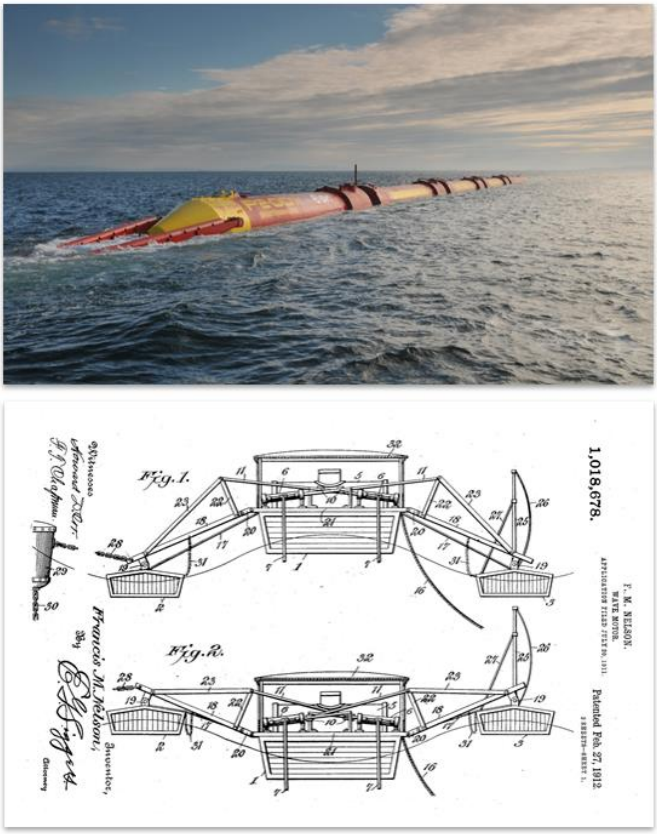

Figure 2: Visual of the Pelamis Wave Power Ltd. device deployed in 2004 (top) and a 1912 patent [9] of a device with the same operational principles (bottom).

In the last twenty years, the wave energy community has progressed in addressing the operational challenges associated with deploying an individual device. Pre-commercial devices - full scale first generation technologies deployed in the ocean - have now been deployed and tested [10], but there remains a wide range of problems to be addressed before wave energy can become a comp4etitive energy source. These challenges can be grouped into two categories: those related to improving design and operation of single, pre-commercial (first generation) devices and those related to the operation of an *array* of multiple commercial (second generation) devices.

At the single device level, current WEC research is focussed on advanced control strategies, and improving operational expertise. At millisecond time scales, observations of the machine state and predictions of the changing wave elevation are used to adapt the WEC's power take off (PTO) system to place the device motion's in phase with that of the wave excitation force thus maximizing power conversion [11]. Control of a WEC is

based on predicting the impending wave excitation force, and changing an intrinsic property of the device to place the device's motion in phase with that of the wave. Generating a resonant condition ultimately maximize the device's power production.

1.1.2 Wave Energy Converter Arrays

A single WEC can produce anywhere from tens of kilowatts to megawatts depending on its design, intrinsic properties and the incident sea conditions [12]. Similarly to the wind industry, devices will need to be deployed in arrays of fifty to even hundreds of devices to meet the growing power demands of coastal populations. Two proposed arrays are depicted in Figure 3 and Figure 4.

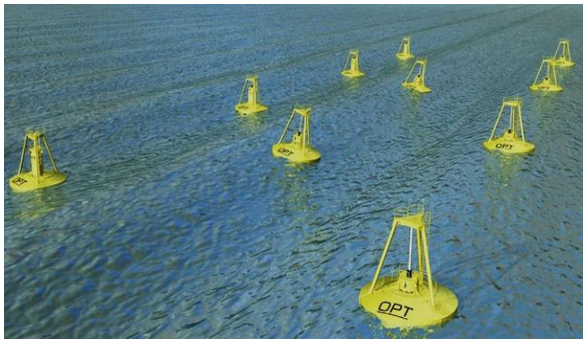

Figure 3: Rendering of an array of Ocean Power Technology's Power Buoy[6]

Figure 4: Rendering of an array of Pelamis devices[7]

Conversely to wind power, the layout of a WEC array can be manipulated to optimize the complete array's energy conversion performance. However, this requires a sound understanding of how each device changes the wave field around it thereby impacting the operations of neighbouring devices. Within the wave energy community, this ability is still evolving.

In 1977 Budal published the first investigation into the theory of power absorption of WEC arrays [13]. Additional studies in the field were conducted in the following years by Evans and Falnes, but most research projects in this field came to an abrupt halt at the resurgence of cheap oil in the 1980s [14]. By the 2000s, increasing oil prices and an ever growing fear of climate change spurred renewed interest in alternative energy research, and by extension, research in commercial WEC arrays [14]. Over time, the questions

[6] http://www.rechargenews.com/news/wave_tidal_hydro/article1295575.ece Last accessed: 18/07/16

[7] http://www.processindustryforum.com/energy/pros-cons-wave-power Last accessed: 18/07/16

surrounding WEC arrays have evolved. The field of research concerning downwave WEC array impacts, commonly referred to as far field effects, have become an area of concern for regulators. This field of array modelling is in its infancy with preliminary studies being published as recently as 2007 [15]–[17]. The models first employed by Budal and Falnes are insufficient to address the impact of commercial scale arrays spanning domains tens of kilometres wide as a result of incompatible spatial and temporal scales. The focus of this thesis lies in developing computational tools that can help regulators and utilities determine the impact an array of devices has on the environment and the power that could be produced from the array. There are a number of aspects to consider when undertaking WEC array modeling with these two specific objectives in mind. First, how do we gather information pertaining to a device's impact on the surrounding wave field? High fidelity time-domain models generate data defining a WEC's dynamics, however most of these time domain models do not consider the feedback of the device on the incident waves given these models are focussed on assessing the performance of that one device [18]. The complete fluid-structure interaction of a WEC and an incident wave is computationally expensive to model, making it impractical to add the calculation of the device's impact on the incident wave to performance assessment exercises. Contrary to the wake of a wind turbine, WECs both absorb energy from incident waves and radiate energy in the form of new waves, changing the wave field around the device in all directions. To model an array, the interaction of each device's modified wave field must be accounted for. However the computational expense of storing and modifying information pertaining to the device and the wave field over tens of kilometres is prohibitive.

1.2 Problem Statement

A WEC is effectively any device that can harness kinetic energy from an incident wave and transform it into another usable form. A standard WEC performance modelling methodology has not yet been determined largely due to the variation in operating principles between devices, as demonstrated in Figure 1 and Figure 2. As the wave energy industry develops, gradual steps need to be taken to address questions surrounding the feasibility of WECs. Initially, we need to be able to accurately characterize the performance of a single device. Several works have described computational modeling

techniques showing great promise for estimating the performance of an individual device [18]–[23]. However, in order to meet growing electricity demands, WECs will need to be deployed in arrays. Investigating WEC performance in arrays is the second critical task the wave energy industry must undertake. In addition to the benefits of increased power production, the deployment of WEC arrays could decrease mooring costs, maintenance costs and above all, electrical connection costs [24]. Notwithstanding its merits, deployment on a large scale faces many obstacles due to a number of unanswered regulatory questions. The energy yield of a WEC array and its ecological impact must be examined in detail before government agencies can move forward with array deployments.

To date, there is a lack of critical mass concerning WEC array modelling and deployment which the work presented in this thesis seeks to address. Array modeling poses the additional challenge of accounting not only for the device's hydrodynamics, but also the modified wave field which will ultimately influence the surrounding devices' performance. Preliminary array studies focused on optimizing power production through constructive wave interaction between devices [13], [24]. As concerns grow with respect to the environmental footprint these arrays have, more studies have been conducted looking at the impact devices will have on the nearshore in coastal models [25]–[28]. A more detailed list of array modelling approaches concerning far field impact are outlined in Chapter 2. Early studies conducted on the environmental impact of devices used constants to characterize the reduction in wave energy as it propagated towards the shoreline [15],[29]. The fidelity of a device's representation in these models increased as WECs were beginning to be modeled with frequency dependent energy extraction [30]–[32]. Ruehl et al. chose to characterize a device within a spectral model (SWAN) using standard WEC performance measures such as relative capture width curves and power matrices [28], [32], [33]. This new module was named SNL-SWAN.

The work presented in this thesis uses pre-existing source code modifications made by the software developers at Sandia National Laboratories (SNL), a US Department of Energy research institution. SNL proposed using a device's power performance measures, calculated externally to the coastal model, to determine the device's far field impact with the added benefit of determining a device's power production potential

through the development of SNL-SWAN. The code modifications made by the author of this thesis further the fidelity in characterizing the far field impact of a device by including the device's hydrodynamics in addition to its power performance. The aggregate hydrodynamic representation of a device draws from previous work done to characterize a single device's performance, which is further described in Section 1.5. The new modifications to SNL-SWAN will allow for a user to take information from a high-fidelity model of a device and assimilate that data into a larger coastal model to ultimately determine the device's impact on the surrounding wave climate.

The previous section has given the reader a brief overview of the state of WEC modelling to date, both as a single device and as an array. However, the specifics concerning how a device extracts kinetic energy from the incoming sea have not yet been discussed. There are a variety of design concepts that are employed. The following section seeks to elaborate on the most common operating principles presently used in the WEC industry.

An overview of the problems surrounding the design and operation of WEC arrays this thesis seeks to address will be presented in this chapter. Furthermore, a brief description of prevalent wave energy converter (WEC) designs that are candidates for case study is presented. To bound the scope of the current study, a reference WEC model is selected and described. The single device modelling architecture used to characterize the reference device is also presented. This single device modelling architecture allows the author to quantify the device's feedback on the incident wave without having to conduct a full calculation of the device-wave fluid structure interaction. The chapter closes with a list of key contributions to be made and a roadmap for the remainder of the thesis.

1.3 Objectives

The recognition of wave energy as an emerging alternative to fossil fuels is subject to the development of reliable tools that utilities and regulators can use to assess a device's far field impact and power performance over long time scales. SNL sought to fulfill this requirement by creating a WEC representation within SNL-SWAN based on a pre-existing functionality for a linear coastal protection structure.

SNL's proposed modules are an improvement on the pre-existing, static representation, however, do not wholly capture the intricacies of the device's hydrodynamic behaviour.

The author seeks to assimilate knowledge previously gathered from high fidelity single device models that developers are already using to characterize their device performance. This information is then processed to generate a static representation of the device's operation in all sea states.

The proposed methodology would allow for large WEC arrays on the order of hundreds of devices, to be simulated in a computationally efficient manner answering questions concerning siting, array layout, farfield impact and annual power product on a time scale compatible with human creativity.

The need to calculate the full fluid structure interaction for a converter is eliminated by assimilating a device's meta-model based on the device's hydrodynamics into SWAN. However, the meta-model is only an approximation to the device's true behavior in each sea. As such, the author seeks to measure the uncertainty in the analyses by examining differences in SNL-SWAN predictions when using different WEC representations. Finally, it is of the utmost importance to determine the utility and limitations of this representation when applied to large computational domains. As such, the author wishes to work with a generic WEC design in that it includes as many of the complicating dynamic factors as possible – moorings, surface piercing, and a full 6 DOF range of motion. An array will also be deployed within a pre-existing SWAN model for a promising WEC location off the West Coast of Vancouver Island. Applying the methodology to a field case ensures the process has potential for long term utility in the industry.

1.4 WEC Design Concepts

This section classifies the types of WECs based on their operating principles. The last design concept discussed, the floating oscillating water column (OWC), will be used as the reference device for the remainder of this thesis. A more detailed description of this reference device is presented, including the specific device dimensions, physical parameters and turbine specifications in Section 1.4.4.

1.4.1 Overtopping Principle

Devices employing the overtopping principle have incoming waves spill over the edge of the WEC where water is held in a reservoir a few metres above sea level. The potential energy of the stored water is converted into useful energy through low-head turbines which generate electricity [8], [34]. These devices are similar to hydroelectric plants but use floating ramps to create an offshore reservoir. Certain devices, such as WaveDragon[8], shown in Figure 6, [35], have wave reflectors which focus the waves towards the device and increase the significant wave height incident to the device. A visual representation of the operating principle is presented in Figure 5.

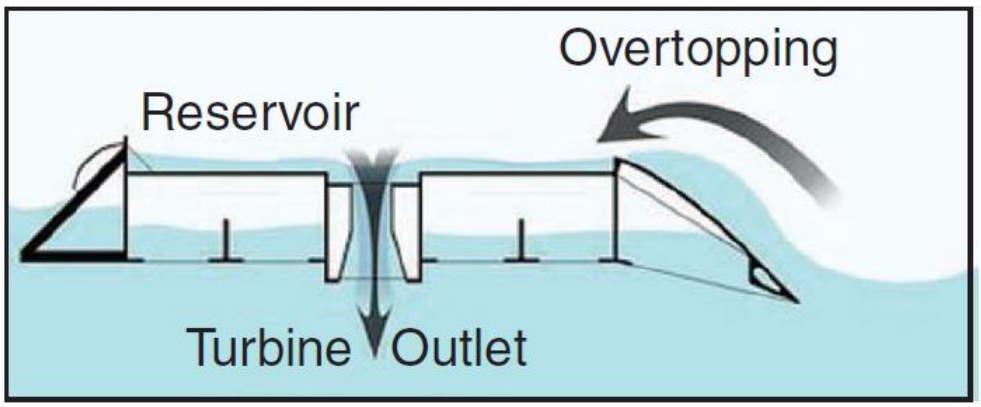

Figure 5: Operating principle of an overtopping WEC [8].

Figure 6: Visuals presenting two WEC designs operating under the overtopping principle: WaveDragon (left) and TAPCHAN[9] (right)

[8] WaveDragon, founded in 2003 http://www.wavedragon.net/

[9] Constructed by NORWAVE, no longer in operation.

1.4.2 Wave Activated Body

Wave activated bodies are WECs composed of several units which are able to move around a reference point. Energy is extracted from the relative motion between the units when the device is excited by a wave [8]. Examples of such devices are pitching flaps, which move around a bottom mounted hinge, and heaving point absorbers where the relative motion between two units is used to power a generator. The aforementioned devices are seen in Figure 7 and in Figure 8 respectively.

Figure 7: Oyster2[10] WEC, a bottom mounted oscillating flap

Figure 8: Ocean Power Technology's[11] PB3 PowerBuoy

1.4.3 Oscillating Water Column

Oscillating water columns (OWCs) feature an internal chamber and oscillating water column within a rigid exterior hull. The device's internal chamber is filled with seawater and air. Waves enter the chamber through an underwater opening causing the air inside the chamber to compress when a wave enters and decompress when it exits [8]. The turbine inside the device is driven by the flow of air caused by the pressure differential created by the relative pressure between the air chamber and external environment [20]. When the seawater leaves the chamber, the cycle repeats itself allowing for bidirectional airflow [8]. The diagram in Figure 9 visually describes the operating principle of an OWC followed by images of device variations installed on and offshore in Figure 10.

[10] Aquamarine Power: http://www.aquamarinepower.com/technology.aspx

[11] Ocean Power Technology: http://www.oceanpowertechnologies.com/pb3//

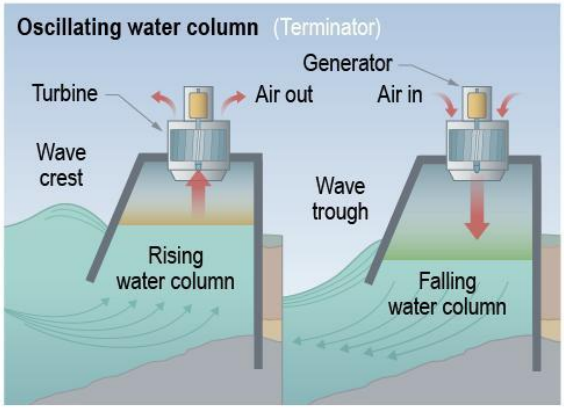

Figure 9: Operating Principle of an OWC [36]

Figure 10: Devices based on the OWC principle. Land Installed Marine Power Energy Transformer (LIMPET) installed in Scotland by WaveGen[12] (left) and greenWave, a device designed by Oceanlinx[13] installed in Port MacDonnell, Australia

1.4.4 Reference WEC Design

The device investigated in the remainder of this work is based on the Backward Bent Duct Buoy (BBDB) as featured in the US Department of Energy's (DOE) Reference Manual [37], [38]. The BBDB is a type of OWC that is used as the reference device for the remainder of this work. From here on, the reference device will be referred to simply as the WEC. The WEC consists of an air chamber, an L-shaped duct, bow and stern buoyance modules, a biradial impulse turbine and a generator. A dimensional drawing is presented in Figure 11 accompanied by a rendering of the device in Figure 12. The mooring system was based on the design proposed by Bull and Jacob using the same

[12] WaveGen,, a subsidiary of Voith Hydro: http://voith.com/en/index.html

[13] Ocealinx: http://www.oceanlinx.com/

mooring line material, lengths and positions of floats [20], [39]. Further physical device dimensions are presented in Table 1.

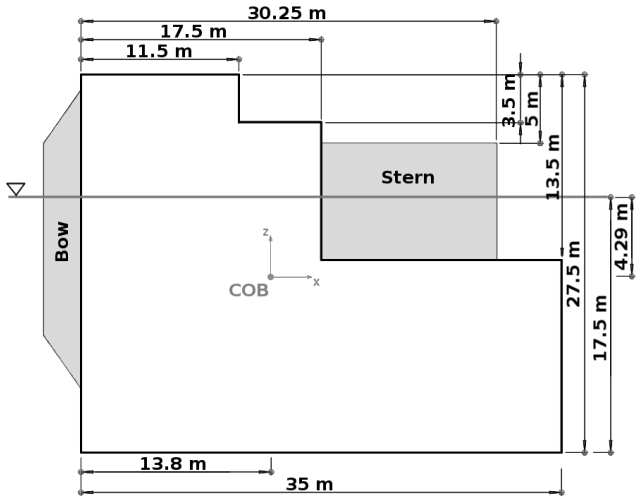

Figure 11: Dimensions of the BBDB OWC Reference Model [20]

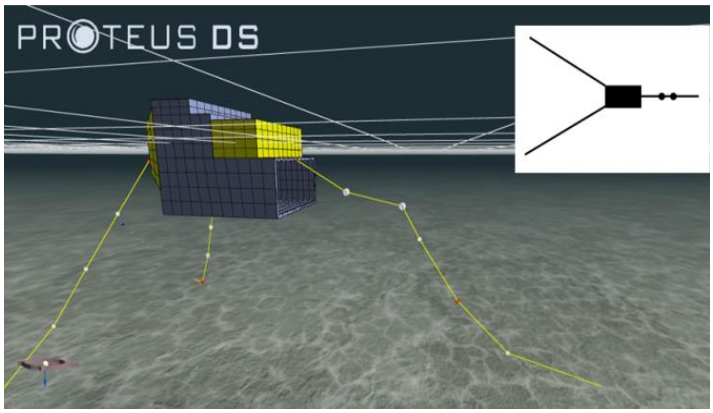

Figure 12: OWC and mooring depiction in ProteusDS[14]

The device's pneumatic system is characterized by a biradial impulse turbine, as presented by Falcao [40] at the interface of the air chamber and the atmosphere. The turbine is symmetric with respect to a plane perpendicular to its axis of rotation. The rotor blades are surrounded by a pair of radial-flow guide-vane rows which are in turn connected to the rotor by an axisymmetric duct whose walls are flat discs [40].

Table 1: OWC Dimensions and Physical Parameters [20]

Property	Value	Units
Width	27	m
Total mass	2.0270e+06 kg	kg
Mass moment of Inertia	Ixx: 3.1825e+08 kgm^2	kgm^2
	Iyy: 4.1625e+08 kgm^2	kgm^2
	Izz: 4.2854e+08 kgm^2	kgm^2
Center of Gravity	x: 16.745m	m
	y: 0 m	m
	z: 4.29 m	m
Center of Buoyancy	x: 16.745m	m
	y: 0 m	m
	z: 3.15 m	m

[14] ProteusDS will be described in further detail in Section 1.5.2.

The device's generator is modeled as a combined variable frequency drive (VFD) and generator that has a rated power that cannot be exceeded. The amount of power the device's turbine transforms from pneumatic into mechanical power is dependent on the turbine's radius, the angular velocity of the turbine set by the VFD and the volumetric flow rate of the air. A 2.5 metre turbine radius is employed with varying angular velocities with each sea state [20]. Numerical sensitivity studies conducted previously by Bailey et al. for this device determined the optimal angular velocity set point for the VFD. These angular velocities are presented in Table 2. The VFD's efficiencies are based on those documented in the DOE Reference Model [41].

Table 2: Optimal angular velocity set point for the VFD of the BBDB OWC [20].

Significant Wave height [m]	4.75	14.4		15.4	16.5		16.4		16
	4.25								
	3.75	12.8	13.7		14.8		14.4		14.3
	3.25								
	2.75	10		12.3		12.6		12	12.3
	2.25								
	1.75	6.8	8		9.7		9.4		8.5
	1.25								
	0.75	5.5							
	0.25								
	Peak Period [s]	6.1	7.2	8.3	9.4	10.5	11.6	12.7	13.8	14.9

1.5 Reference WEC Simulation Architecture

The reader is reminded that the focus of this thesis lies in modelling multiple devices by drawing upon previously calculated high fidelity data sets that define the dynamics of a single device in all possible environmental conditions. Thus, before proceeding to the development of a candidate WEC array model, a description of the high-fidelity analysis tool that underpins that work must first be provided.

The following section outlines the methodology used to simulate the WEC's hydrodynamics, and by extension the power performance of a single WEC. The device modelling architecture is referred to as the pre-processing step given the outputs will be used in the work presented later on in this thesis. The WEC simulation architecture is composed of three software packages:

1. WAMIT - a linear potential flow model used to establish frequency dependent hydrodynamic coefficients that are determined based on the device's geometry.
2. ProteusDS - a time domain simulator used to calculate a device's dynamics over time using both linear and non-linear force contributions.
3. Simulink – a graphical solver and dynamic simulation tool that is coupled with ProteusDS to characterize the thermodynamics and air turbine dynamics within the OWC's air chamber [20].

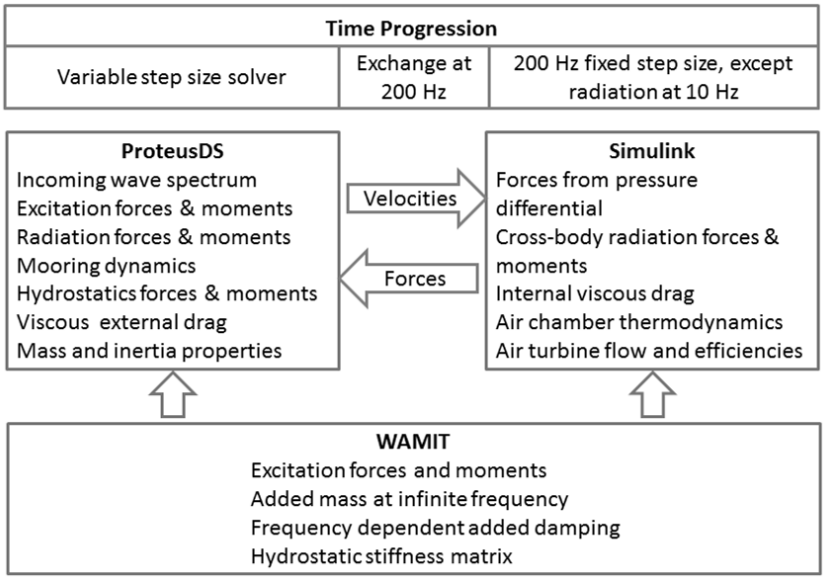

Figure 13: Summary of the complete device modelling architecture and the different software packages used to implement it [20].

The model architecture and information passed between the three models used is summarized in Figure 13. This section is concluded with a description of the environmental conditions used to force the device's time domain simulations. The environmental conditions are based on the most commonly occurring sea states at a promising WEC farm location off the west coast of Vancouver Island [42].

1.5.1 Calculation of Inviscid Forces

Linear potential flow is widely used to model wave-structure interaction in an incident wave field. These models are based on the assumptions of inviscid, incompressible and irrotational flow as well as linearity assumptions such as: the wave height to wave length and wave height to depth ratio are less than one, and the body motions are small [43].

WAMIT is a linear potential boundary element method (BEM) code which solves for the velocity potential and fluid pressure on submerged bodies [44]. The diffraction problem and radiation problem [45] for the user defined prescribed modes of motion are solved at each panel in the user defined mesh. The diffraction problem is based on solving the potential flow field for a fixed WEC in an incoming wave field. Diffraction accounts for forces derived from the waves moving around the stationary object (scattering forces) and the forces from the dynamic pressures on a surface of the WEC's mesh, the Froude-Krylov force. Hydrodynamically transparent devices, are only affected by the Froude-Krylov force. The radiation problem consists of solving for the potential flow field surrounding a moving WEC in still water and then integrating the resulting pressure field over the hull to recover the fluid force and moment. The force on the WEC is separated into two components: added mass and damping. These components are in phase with the WEC's acceleration and velocity respectively. The hydrodynamic stiffness matrix is based on the static pressure on the WEC's mesh and the centre of mass. These hydrodynamic parameters are calculated in WAMIT and are used later by the time domain simulator to determine the device's response to an incident wave.

The OWC's wave structure interaction is unique in that there is an oscillating free surface within the OWC's air chamber [46]. In order to account for this second free surface that has a different dynamic response to the external free surface, the device employs different panels across the mesh as well as a generalized mode [20], [44]. Standard panels are used around the buoyancy chambers which have both a wet and a dry side. Dipole panels are wet on both sides and represent the hull shape which is modeled as a thin structure. Finally, there is a panel on the water surface inside the OWC's air chamber [20]. This panel, which is also referred to as a light piston, is modeled with an additional generalized mode which was previously used to model moonpools in the *Navis Explorer I* drillship [47]. Generalized modes allow for additional degrees of freedom due to articulated bodies which in this case represents the water surface within the air chamber.

In summary, The BEM code WAMIT is used to calculate the excitation forces and moments, frequency dependent added mass, added damping and the hydrostatic stiffness matrix which are all used within the time domain simulator [20].

1.5.2 Calculation of Hydrodynamics

ProteusDS is a time domain simulation package that has been experimentally validated for WECs [19], [48]. The simulation includes a six degree of freedom (DOF) floating OWC hull with the water elevation within the air chamber represented as an additional one DOF light piston. A brief description of the six DOF modelled is presented in Table 3. A detailed and realistic mooring is also included in the simulation architecture, as seen in Figure 12. The hydrodynamic excitation, radiation, viscous drag and buoyancy forces are calculated for both bodies as well as the force between the bodies and the moorings on the hull. Hydrodynamic and hydrostatic parameters calculated in WAMIT, as described in Section 1.5.1, are used as inputs in the software to propagate the WEC's dynamics over time using an adaptive, variable step Runge-Kutta solver [49], [50]. The hydrodynamic forces acting on the device are calculated for each DOF. The excitation force is the summation of the dynamic pressure across the stationary body from the incoming wave and the resulting diffracted waves [45] obtained directly from WAMIT for different wave frequencies, directions and each DOF [20]. The mooring forces are calculated using a cubic-spline lumped mass cable model presented by Buckham [51]. Finally, viscous drag is calculated by finding the total viscous drag force on each panel of the OWC's mesh based on Morrison's equation, for each translational degree of freedom. The reader is directed to the ProteusDS manual for any further inquiries regarding how ProteusDS calculates its forces [50].

Table 3: Description of the six degrees of freedom modeled in the time domain simulations of the OWC

Type	Degree of Freedom	Motion
Translational	Heave	Vertical (up and down)
	Sway	Lateral (side to side)
	Surge	Longitudinal (front to back)
Rotational	Pitch	Up and down rotation about the lateral axis
	Roll	Tilting rotation about the longitudinal axis
	Yaw	Turning rotation about the vertical axis

1.5.3 Calculation of Thermodynamics

In addition to the hydrodynamic forces induced by the surrounding fluid, the OWC's biradial impulse turbine, which sits between the air chamber and the atmosphere, restricts the flow of air into and out of the chamber. As the internal water column rises and falls, a differential air pressure develops in the chamber which creates force on both the OWC hull and the water column. These reaction forces influence the device's dynamics and must be accounted for. To track the thermodynamic state (temperature, pressure and density) of the air in the chamber, the ProteusDS simulation was coupled with a Simulink model of the air chamber and turbine

Simulink is a block diagram programming environment for multi-domain simulations [52], and Simulink dynamic models can be linked to ProteusDS at run time. The Simulink air chamber model uses knowledge of the platform and water column motions to set the volume of the air chamber.

The mass flow rate through the turbine is modelled based on the first law of thermodynamics, and assuming the air in the chamber behaves adiabatically and as an ideal gas, A parametric model was developed by Josset and Clement for setting the mass flow rate into and out of the device based on the pressure differential [20], [53]. This method includes a number of assumptions: an ideal gas; isentropic compression and expansion; negligible kinetic and potential energy changes inside the chamber during operation, negligible momentum for the air passing though the turbine and homogeneous composition of the gas in the chamber. The isentropic assumption allows the density within the air chamber to be calculated from the absolute pressure [20].

The thermodynamic properties of the air chamber were calculated in Simulink. These properties include: the absolute pressure within the air chamber, the differential pressure induced forces on the hull and water column and finally, the volumetric air flow rate though the air turbine. As mentioned in Section 1.4.4, a VFD is required at the interface between the turbine and the device's generator to keep a constant angular velocity and vary the turbine's torque. The angular velocity of the VFD was set according to the optimal velocity in Table 2 from which the Simulink model was able to calculate the mechanical power produced by the device's generator [20].

Simulink sends forces corresponding to the device's air chamber thermodynamics and turbine flow to ProteusDS. These forces are applied to the hydrodynamic model as internal reactions. ProteusDS sends kinematic information in the form of velocities which set the changing volume of the chamber. As a result of the coupled nature of the air chamber dynamics and the device's hydrodynamics, the Simulink and ProteusDS models were coupled, exchanging force and velocity information between the two models at 200 Hz in real time [20].

In addition to the thermodynamics of the air chamber, the Simulink model is used to calculate the cross-body radiation forces and moments that result from absolute motions of the OWC hull and water column. The two bodies radiate waves that apply force to the other body. The radiation forces within the chamber are calculated using a convolution of the velocity time histories of both the water column and the hull with impulse response kernels calculated from WAMIT [54]. The cross-body radiation force on the water column is produced through a subset of the OWC hull DOFs. Only the OWC surge, heave and pitch DOFs produce radiation forces on the water column [20].

1.6 Environmental Conditions

To define the fluid structure interaction of the OWC with a range of possible irregular wave conditions, a series of time domain simulations was completed. The range of 'possible' wave conditions was determined by using wave buoy measurements recorded at Amphitrite Bank (48.88N, 125.62W), a promising WEC installation location off the west coast of Vancouver Island [55] shown in Figure 14 and Figure 15. Each node connected by the mesh presented in Figure 14 contains energy density that is distributed across frequency and directional bins. Energy density is propagated across the links presented in this mesh. The free surface condition of the sea, commonly referred to as a sea state, is typically characterized by wave statistics. The bivariate histogram in Figure 16 presents the most prevalent sea states at Amphitrite Bank charted by significant wave height and energy period. Sea states were only included in this study if they occurred for more than 24 hours over the course of the year in order to reduce computational overhead – a total of 44 sea states satisfied this criterion. Twenty-two additional sea states were distributed around the periphery of the bins in Figure 16 to ensure that interpolation of

device performance across the bins did not suffer from errors due to the truncation of data.

A directional spectrum was formed for each bin in Figure 16 using a Pierson-Moskowitz spectrum. The Pierson Moskowitz spectrum is an idealized sea state which assumes winds have blown over an area over five thousand wave lengths long on either side for several days [56]. This spectrum has previously been established as a good model for the spectral distributions observed at this location [55]. A cosine squared directional spread was applied about the primary direction as suggested by DNV standards [57]. Custom wave segments were used to represent a Pierson Moskowitz spectrum in ProteusDS characterized with a significant wave height, peak period and a directional spreading factor of two. The model input for each wave segment requires a wave amplitude, heading, and phase. The user-defined wave segments are summed to find the water surface profile propagated towards the device in each simulation using Eq. (1) [50]. For each sea state, OWC operations were simulated 20 minutes, as recommended by IEC standards [33] with 140 different wave segments constituting the spectrum [58].

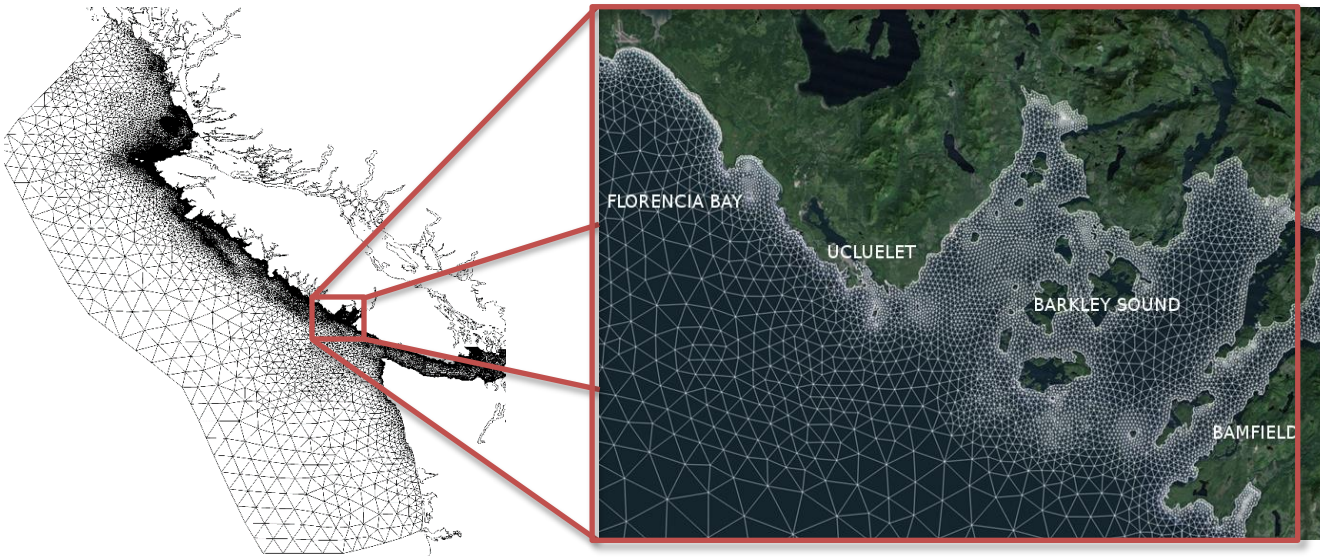

Figure 14: Mesh of the West Coast of Vancouver Island extending from the southern tip of the Haida Gwaii islands to the Washington-Oregon border and includes the Strait of Juan de Fuca [42], [55], [59]

Figure 15: Nearshore mesh of Amphitrite Bank from the WCWI SWAN model of the West Coast of Vancouver Island [42], [55], [59].

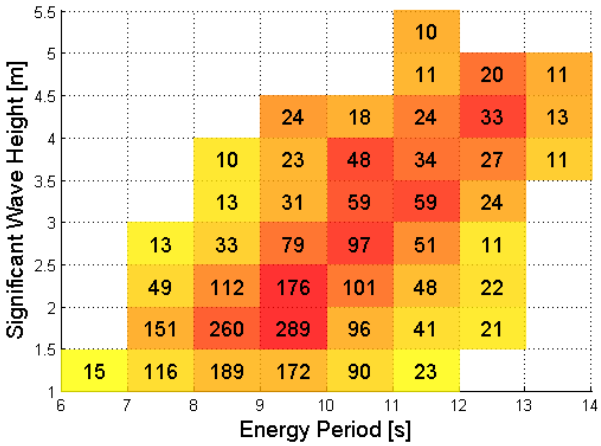

Figure 16: Number of times each sea state occurred at Amphitrite Bank in 2006 at a three hour resolution. Sea states that occurred for less than 24 hours have been truncated.

1.7 Preprocessing Simulations and Results

Each sea state identified in Figure 16 was simulated using the simulation architecture previously described. Both of the ProteusDS and Simulink output data were consolidated to produce a complete history of the motions of the OWC, hull, the three mooring lines and the massless piston (representing the internal water column) as well as all the forces and moments acting on these bodies. The kinematic data sets included output for each relevant DOF of each body. Relevant DOFs are those in which significant energy transfer occurs.

The author has extracted as much information as possible regarding the WEC's operation and response to incident wave conditions from the time domain simulators. Detailed force and velocity time series were collected from the incident wave, the OWC hull, the water column, PTO and moorings allowing the author to calculate the transfer of energy between these components.

If one examines Figure 17 and takes the time series on the left (force in heave) and conducts an element by element multiplication with the values on the right (velocity in heave), the product of these values is a time series of power which integrated over time results in an energy.

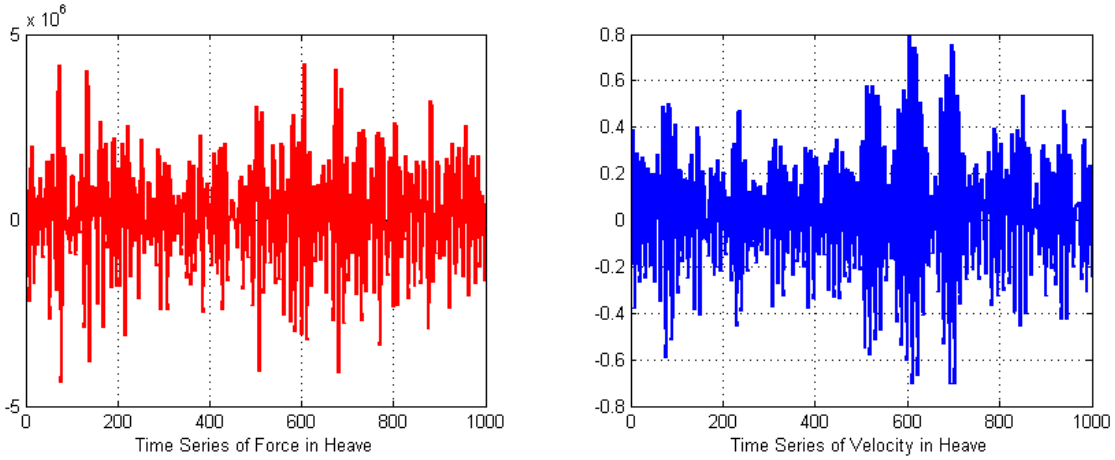

Figure 17: Time Series of the Incident Loading (right) on the OWC body in heave and the velocity of the body (left) in heave

The forces calculated within the time domain can be used to determine the device's net force contribution on the surrounding fluid domain. These contributions are then translated into an energy can be incorporated into a spectral model, such as SWAN as will be further discussed in Section 3.5.7.

1.8 Key Contributions

Although we have amassed high fidelity datasets with respect to the WEC, no information pertaining to the device's impact on the wave or how the surrounding fluid domain is being impacted is explicitly provided. The work presented in this thesis suggests taking the dynamics of a single WEC modelled in the time domain and back calculating the device's hydrodynamic losses and net force contribution onto the surrounding sea. A meta-model capable of representing the interaction between the device and the surrounding fluid domain is generated for the reference WEC allowing for a better representation of devices deployed in an array. This static representation can then be applied in between nodes within SWAN allowing for the device's impact on the surrounding wave field to be realized within the wave model.

By developing and testing candidate meta-models of the reference WEC, the current work will contribute to the field of wave energy conversion in the following ways:

1. Developing a computational framework for transforming the simulated dynamics of a single WEC (i.e. time histories of forces and velocities) into both temporally

and spectrally resolved descriptions of the power transfer (both directions) between the incident waves and the WEC.

2. Establishing candidate tabular representations, or meta-models, of the spectral power transfer that occurs over a variety of wave conditions that are compatible with coastal wave models, such as that shown in Figure 14. Here, a "representation" includes the tabulated results and a physically justified means of inserting those tabulated results into the governing equations of the coastal model.
3. Establishing the sensitivity of the final system outputs (i.e. the far field impacts and the WEC array power production) on the choice of candidate WEC representation. Through these sensitivity studies, the work also contributes an estimate of the uncertainty in the process.
4. Implementing the candidate meta-models within an existing large scale coastal model based on the SWAN software and for a case of a very large commercial scale farm (tens to hundreds of WECs), identifying any technical impediments and testing means of negotiating these challenges.

1.9 Thesis Outline

The remainder of this thesis is laid out as follows:

Chapter 2 includes an overview of previous work that has been conducted in the field of array modeling. The works are divided by the governing equations for each of the models. In conclusion, a brief description of the model physics used to model arrays for the remainder of this thesis is presented.

Chapter 3 outlines how a device is characterized within SNL-SWAN. Previous device characterizations developed by SNL are described. This is followed by a detailed account of where power is transferred when a device extracts power from an incident wave. This power transfer demarcation is then used to generate a hydrodynamic meta-model for the device. Chapter 3 is concluded with a description of the author's newly proposed methods to characterise a device within SNL-SWAN.

Chapter 4 presents the methodology used to compare the different methods used to characterise a device, as presented in Chapter 3. The difference in annual power

production and far field impact of a device in each of these characterizations is analysed in a numerical test basin as well as applied to a field case.

Chapter 5 reviews unresolved issues in the present work.

Chapter 6 summarizes the key conclusions of this thesis and presents recommendations for future work in the development of a spectral wave array modelling tool.

Chapter 2

Literature Review

The wave energy community has progressed in addressing the operational challenges associated with single device deployment. The advances made to date are sufficient for the pre-commercial stage of device development but the installation of a single device will be insufficient to meet the power production needs of larger communities. To truly make WECs commercially viable, tens to hundreds of WECs will need to be deployed in an array. The installation of WECs in farms would result in cost savings associated with moorings, electrical connections and maintenance [24]. However, as with any emerging technology there are a number of unanswered questions regarding the operation of arrays that need to be addressed.

Power production from an array may be smaller or larger than the sum of the power produced by an equivalent number of independently sited WECs due to the power absorbed and radiated by the hydrodynamic interaction of closely spaced devices [24], [60]–[63]. Utilities are interested in determining how much these array interactions impact the total power produced by the array and what configuration would ultimately produce the most power. Wave energy developers are conversely interested in how a control strategy can be adopted to produce the most power in an array. Additionally, numerical and scale model tests of small WEC arrays have demonstrated wave height attenuation between the WEC array installation site and a downwave location [26], [27],

[62], [64]. Wave field modifications caused by WEC array installations can influence neighbouring coastal ecosystems, coastal defence structures and industries [62]. Regulators are concerned with the extent of wave height attenuation at the shoreline and how this attenuation will impact pre-existing uses. As the field of WEC array design and analysis advances, it is growing more evident that one universal computational framework cannot effectively address all these concerns.

It appears that even within the narrow field of WEC array modeling, there exists a creative choice a modeller must make to address the research question at hand. Previous works have proposed frameworks that best address the primary concerns of electric utilities and regulators - namely the energy yield and far-field impact of an array. Given the large time scales and spatial domains utilities and regulators are interested in, a computationally inexpensive model is crucial for these analyses.

Prior research largely draws from coastal wave models previously used to quantify the wave attenuation associated with natural or manmade obstructions in the nearshore. These models obtain realistic wave parameters in coastal areas and estuaries from given wind, bottom and current conditions [65]. The definition of an obstruction, or obstacle has changed as wave models have developed. Third generation wave models such as SWAN were originally developed to model how waves change as they approach a shoreline [66]. Obstructions, or obstacles, can be defined as a number of things. Natural obstructions such as submerged reefs can reduce the wave energy transmitted to shore. Man-made structures such as groins or breakwaters are built to prevent sediment transport and consequently beach erosion as waves break along the shore [67]. Significant changes to the nearshore wave field are made by both natural reefs and breakwaters as a result of wave overtopping, breaking over the crest, permeability through the structures and wave diffraction [67]. The main physical processes involved in wave transformation over and around submerged breakwaters are wave shoaling, reflection, refraction, diffraction and breaking. Transmission coefficients used to characterise these structures in nearshore wave models have typically been calculated for such obstacles by using empirical formulae dependent on the incident wave height, structure width, depth, etc. [68], [69].

A constant transmission coefficient may be appropriate for a static structure however, the response of a moored, wave-generating device will change depending on the incident wave condition. As a result, the transmission coefficient representation previously adopted for static structures cannot sufficiently represent the dynamic responses associated with WECs. The representation of an obstacle for breakwaters and WECs alike varies from one coastal model to the next.

This chapter provides an overview of literature in which arrays of WEC devices have been modeled in an effort to quantify the far field impact of a device. The benefits and short comings of these models are presented followed by a discussion of the model chosen for the remainder of this work.

2.1 Fundamentals of Wave Modelling: Airy Waves

Over the past 150 years deep water surface gravity waves have been conveniently characterized with Airy wave theory based on both the conservation of mass and momentum upon which kinematic and dynamic boundary conditions are imposed. The conservation of mass is the foundation of the Laplace Equation [4]. The velocity potential function is a scalar function describing the particle velocity of the water. Particles cannot leave the surface of the fluid or penetrate the bottom as specified by the kinematic boundary conditions. An analytical solution to the Laplace equation with the aforementioned kinematic boundary conditions is a harmonic wave as described in Eq. (1) [50]. The free surface displacement, η, is defined as:

$$\eta = A\,cos(\omega t - k(x_c cos(\theta_h) + \mathrm{y_c}\sin(\theta_h) + \phi) \qquad (1)$$

where A is the wave amplitude, ω is the angular wave frequency, k is the wave number, θ_h is the wave heading (direction), ϕ is the wave offset (phase) and x_c, y_c are the coordinates with respect to a user-defined reference frame.

This convenient representation comes as a result of fundamental simplifications. It is assumed the fluid medium is incompressible, inviscid, maintains a constant density and is continuous[15] [4]. Wave amplitudes are also assumed small compared to the wave length and the water depth. These assumptions are violated in shallow water conditions where

[15] Water can be discontinuous if there are air bubbles present, often occurring when waves break.

waves are steeper and viscous effects such as bottom friction impact a wave's motions [4].

Representing ocean waves as harmonic and independent waves has conveniently allowed for the use of mathematical tools such as Fourier transformations and the representation of polychromatic seas by wave spectra. A wave spectrum is a representation of the sea surface at any instant in time by characterising the waves at a particular location with respect to their amplitude, frequency and direction. The sea surface at any point in time and at any location can be reproduced as a sum of a large number of harmonic wave components which represent the surface displacement, as seen in Eq. (2):

$$\eta = \sum_{j=1}^{Q_d} \sum_{i=1}^{Q_f} A_{i,j} cos(\omega_i t - k(xcos(\theta_{j,h}) + \mathrm{ysin}(\theta_{j,h}) + \phi_{i,j}) \quad (2)$$

where η is the surface displacement, A is the wave amplitude, ω is the angular wave frequency, k is the wave number, θ_h is the wave heading, ϕ is the wave offset (phase) and x, y are the coordinates with respect to a user-defined reference frame, i is the index for the number of frequency bins, Q_f, and j is the index for the number of directional bins, Q_d. Even though there may be an infinite number of frequencies and directions that characterize a sea state, these properties must be discretized into a certain number of bins for feasible computation. By applying a Fourier analysis, the values of the amplitude and phase can be determined for each frequency, as can be seen in Figure 18. For most deep water wave records the phase information will have values varying between 0 and 2π without any preference for one value. The phase information is discarded and a uniform distribution for phase is assumed. To reduce sampling bias, the Fourier analysis is repeated over a number of observations and the mean amplitude spectrum is used to characterize the sea condition [4].

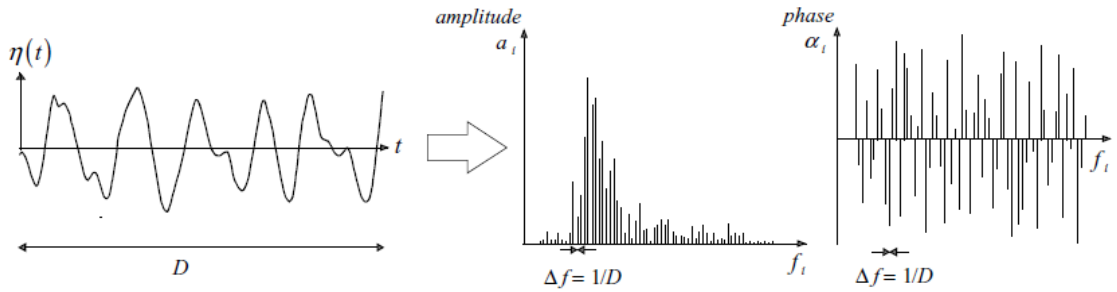

Figure 18: An observed, one dimensional surface elevation profile (left) and the spectral representation as an amplitude and phase spectrum [4]

Wave amplitude is an intuitive means by which to measure waves because of its physical significance. A second parameter with which waves are measured is variance, which by definition is the time-averaged squared surface elevation relative to its mean:

$$\sigma_{i,j}^2 = \frac{1}{2} A_{i,j}^2 \tag{3}$$

where σ^2 is the variance. Spectra are commonly represented with variance opposed to amplitude for two reasons. First, variance is a flexible statistical parameter. The sum of the variances is the variance of the sum, which is not true for the wave amplitudes of the same wave record. The summative property of variance is especially useful when rebinning wave spectrums. Secondly, the linear theory for surface gravity waves shows that the energy within waves is proportional to the variance [4]. The variance spectrum is discrete, however all frequencies are present at sea. In an effort to characterize the continuous nature of the wave spectrum, the variance can be distributed over the frequency interval at each frequency. The variance density spectrum, E_v, is defined for all frequencies but is still discontinuous from one frequency band:

$$E_{v,i} = \frac{1}{2} \sum_{j=1}^{M} A_{i,j}^2 / \Delta f_i \tag{4}$$

where f is the frequency corresponding to the bin across which the variance is distributed. As the frequency bin width becomes infinitely small, the variance density spectrum will become continuous. Variance can also be used to determine useful bulk parameters such as the significant wave height, peak period and mean energy period. Even though the variance density spectrum is a useful statistical representation of the sea surface, it lacks physical significance. By multiplying the variance density spectrum by

the water density and the gravitational constant the energy density spectrum, E_i, is obtained:

$$E_i = \rho g \, \frac{1}{2} \sum_{j=1}^{M} A_{i,j}^2 / \Delta f_i \quad (5)$$

where ρ is the water density, g is a gravitational constant. The energy density spectrum demonstrates how wave energy is distributed across different frequencies. Overall, the sea surface representation used by coastal wave models varies depending on the specific phenomena (wave shoaling, refraction, diffraction, etc.), spatial and temporal resolution required for a particular analysis. Wave models are typically categorized as either phase-resolving (where the water surface elevation, wave amplitude, direction and phase are tracked for each node in the grid) and phase-averaged (where the wave spectrum is recorded at each node). The following section will review both kinds of models in further detail.

2.2 Boussinesq Models

The Boussinesq equations originally developed in 1872 are capable of accounting for the vertical structure of both the horizontal and vertical flow velocities in a wave field. The derivation begins with the depth-integrated continuity equation and the Bernoulli equation for surface velocity which are closed with a relation between the depth-averaged velocity and the surface velocity [70]. The equations went largely unused until the advancement of computing in the mid 90's and onwards [71]. Since the original development of the Boussinesq equations, more robust forms have been developed to account for varying bathymetry and to operate in deep water [72], whereas before solutions were limited to intermediate to shallow water before the surf zone [67]. These models calculate the instantaneous water surface elevation at each point in the domain, Certain software suites such as MIKE 21 BW will also calculate the phase averaged statistical parameters and wave disturbance parameters [73]. Boussinesq models are most appropriate when modeling waves with strong nonlinearities, otherwise the mild-slope equation, addressed in Section 2.3, is preferred [67]. A more detailed derivation of a recent and commonly used form of the Boussinesq equations is provided by Madsen et al. [70]. This series of equations is largely of interest to those modeling harbour resonance,

seiches (standing waves), wave-wave and wave-current interaction because the horizontal plane of wave propagation can be well resolved without having to account for the vertical coordinate from the Navier-Stokes flow equations [74]. Boussinesq models are phase-resolved, as a result wave phenomena such as shoaling, refraction, diffraction and wave breaking can be represented making the model suitable for analyzing the impacts a WEC array would have on the nearshore wave climate. While these models do predict nearshore hydrodynamic effects well at a small scale (domains of ten wavelengths [75]) , they are too computationally intensive for modeling larger areas or long periods of time (typical time steps on the order of minutes) [43]. An array of five interacting devices was modelled by Venugopal and Smith near the Orkney Islands using an enhanced Boussinesq solver [17]. The devices were modeled as both reflecting and absorbing sponge layers, but porosities and reflection coefficients were not related to specific devices – hypothetical porosities of 0,0.6, 0.7, 0.8 and 0.9 were applied. In conclusion, Boussinesq models are favourable for analyzing device interactions on a small scale since they can represent phase dependent wave transformation processes, such as radiation and diffraction. Boussinesq models however, become too computationally expensive in domains larger than a few kilometres or temporal durations greater than tens of hours.

2.3 Mild slope Models

Mild slope equations are based on the Hamiltonian theory of surface water waves where the vertical coordinate has been eliminated for faster computation time [76]. These equations describe the transformation of linear irregular waves across a slowly changing bathymetry and have been used to compute wave transformations near offshore structures for at least 40 years [77], [78]. Mild slope models calculate the instantaneous surface elevations throughout the domain, with a relatively low computational and accuracy cost and high stability [62].Two separate techniques have been used to represent WECs in mild slope models.

Beels studied the wake effects of a single device and an array of overtopping WECs using a mild slope model in both uni- and multidirectional waves [30], [77] where a device is represented as a sponge layer covering the spatial extents of the WEC. Absorption functions define the absorption of the device at each cell of the WEC in both the x and y direction. Coefficient values were determined through tests in a numerical

wave tank where previously derived equations determining the overtopping discharge were used to determine the device's efficiency in different irregular seas [77].

Most recently, Babarit et al. [79] modelled a WEC within ARTEMIS, a mild-slope model [79]. Babarit characterized the far field effect of a device with a Kochin function - an asymptotic expression for an outgoing wave which superposes circular diffracted and radiated waves generated by a device. This formulation was originally derived by Kochin in 1940 but has found use in more recent naval architecture applications [45], [80]. The Kochin function is found using the diffracted and radiated velocity potential associated with the WEC calculated from a BEM solver. Given a particular incident wave condition, a device will generate its own radiated and diffracted wave. The Kochin function sums the complex amplitudes of the waves generated by the device at a user-defined far-field point (or circle) [45]. The total far field potential is then converted to variance and input back into the wave model. Mild-slope models have a low computational cost relative to Boussinesq models with relatively high accuracy [43], but they still suffer from numerical instabilities that arise due to rapidly varying topography and when waves shoal in shallow waters [67], [81]. Mild slope models are also limited to smaller domains. Generally, at least ten gridpoints per wave length are recommended and time steps should be chosen based on a Courant number criterion, limiting the application of the model to simulations on a minute to hourly scale [82].

2.4 Spectral Action Density Models

Rather than accounting for each wave individually, spectral action density models follow the evolution of an entire wave spectrum across the model domain. At each spatial node, the variance (or action density in the case of currents) is computed opposed to the instantaneous water surface elevation which is calculated in both the Boussinesq and mild slope models. Tracking the water surface elevation and phase is important for characterizing wave phenomena such as diffraction and radiation however, the spectral action density approach allows for a quick and numerically stable solution to wave propagation by tracking variance and assuming a uniform probability distribution for phase.

The model is capable of representing most wave nonlinearities such as wave breaking and wave-wave interactions, as seen in Eq. (6). However, it cannot explicitly model

diffraction and thus employs a phase-decoupled numerical approximation for this phenomenon [83], which is described further in Section 2.5. The governing equations present how a wave spectrum evolves over the computational domain. The first three terms on the left hand side of Eq. (6) denote the propagation of the wave energy spectrum over time, *t*, and space *x,y* respectively. The fourth term represents the depth and current induced refraction. Finally the fifth term on the left represents the effect of shifting frequencies due to variations in depth and mean currents. The right hand side of Eq. (6) contains source and sink terms that non-linearly redistribute energy. Action density is conserved in the presence of currents, opposed to energy density and as such, the evolution of action density over the computational domain is defined as:

$$\frac{\partial N(\sigma,\theta)}{\partial t} + c_x \frac{\partial N(\sigma,\theta)}{\partial x} + c_y \frac{\partial N(\sigma,\theta)}{\partial y} + c_\theta \frac{\partial N(\sigma,\theta)}{\partial \theta} + c_\sigma \frac{\partial N(\sigma,\theta)}{\partial \sigma} = \frac{S}{\sigma} \qquad (6)$$

$$S = S_w + S_{nl3} + S_{nl4} + S_{bf} + S_{wc} + S_{dp}$$

where *N* is the action density spectrum, c_x and c_y are the propagation velocities in spatial x-y space, c_θ and c_σ are the propagation velocities in directional (θ) and frequency (σ) space respectively [84]. The source terms (*S*) that are accounted for in most third generation spectral action density models include wave growth by wind (S_w), triad wave interactions (S_{nl3}), quadruplet wave interactions (S_{nl4}), wave decay due to bottom friction (S_{bf}) and whitecapping (S_{wc}) and finally wave decay due to depth induced wave breaking (S_{dp}).

Spectral action density models have been used to calculate wave transformations over large areas in order to find accurate wave conditions near shorelines [85]. In recent years, the use of these models has been extended to the study of a WEC array's far field impact particularly in the MIKE spectral wave model, TOMAWAC and Simulating WAves Nearshore (SWAN) where WECs have been represented as bathymetric features, source and sink terms at a node or as linear energy transmitting obstructions.

Greenwood et al. simulated WECs within the Danish Hydraulic Institute's (DHI) MIKE 21 spectral model using three techniques to simulate a WEC: a source term, an artificial island and a reactive polygon. The reactive polygon was found to be the most realistic method because it accounted for device specific frequency and directional impact on the waves. |Downstream wave power was decreased by 5% on average and

upstream values increased by 7.5% on average indicating the importance of including reflection within the representation of a WEC [86].

Folley and Silverthorne represented WECs as source and sink terms within TOMAWAC, a spectral action density model developed at the Electricité de France's Studies and Research Division. Frequency-dependent reflection and absorption are characterized by these simulations based on a device's hydrodynamic coefficients [31]. Silverthorne and Folley used a frequency dependent function to represent a WEC within the model. The device's inertial, radiation and damping forces were determined for the case of maximum energy extraction and used as inputs into the model [31]. The authors were able to capture radiation effects within the WEC array, enhancing a spectral wave model's capacity to calculate an array's power performance.

The most advanced wave array depictions to date have been implemented in the software SpecWEC, a module of the spectral domain model TOMAWAC developed by the PeraWAT project between 2009 and 2013. This spectral domain model captures the non-linear effects of a wave energy converter and uses phase-averaged approximations to represent radiation. The SpecWEC software has been cross-validated with both the numerical time-domain model WaveDyn as well as tank tests conducted at the Queens University Belfast's Portaferry wave tank [87],[63]. Child and Weywada compared the performance of a 24 unit array of point absorbers in the SpecWEC model to experimental results in a variety of spectral sea states. The difference in yield between the spectral-domain and experimental results is between 3.6 and 14.4% with an average of 7.9% which the authors considered a good level given the uncertainties in the experimental tests. This study has confirmed that phase-averaged models can be reliable tools for modelling WEC arrays [63].

SWAN has been used to model WEC arrays as both a single obstacle and a number of obstacles [43], using a transmission coefficient specifying the percentage of energy absorbed by the device [15], [88]. Millar et al. investigated the effects of WEC arrays in SWAN by modelling entire arrays as four kilometre long partially transmitting obstacles at the Wave Hub test site. These arrays were given transmission coefficients of 0, 70, 90 and 100%. The aforementioned transmission coefficients vary between complete absorption of wave energy to zero absorption. Even in the worst case, where all wave

energy before the obstacle was absorbed, the maximum reduction in significant wave height at the shoreline was 21.7%. Device specific parameters were not used in the study and individual devices were not modelled [15]. Iglesias and Veigas confirmed Millar et al.'s sensitivity analysis by conducting a similar analysis at a wave farm in Tenerife, Canary Islands, Spain. Transmission coefficients of 0, 25, 75 and 90% were modeled to see whether there were drastic changes in significant wave height (H_s), energy dissipation due to bottom friction and directional spreading. The most drastic change in H_s was observed between transmission coefficients of 75 and 90% with respect to changes in H_s and energy dissipation. Directional spreading was increased in the central wake of the farm and decreased around the edges [29]. Further nearshore wave climate studies were conducted by Smith et al. in 2012. The authors modified the SWAN source code in order to allow for user input of frequency and direction dependent coefficients within the obstacle command. The authors of this study generated hypothetical power transfer functions as input for transmission coefficients [88]. Porter modelled the far field impact of a WEC array using nested grids within SWAN's computational domain. Longshore transects were chosen in between the rows of devices within an array. A spectral file was output and modified outside of SWAN using a device specific transfer function. The modified wave spectrum was used as the input for the next row of wave energy converters within the array [89], which became the proof of concept for SNL-SWAN.

Recently, SNL-SWAN has improved the characterization of a device within a wave model by modifying the standard obstacle command in SWAN to allow for both sea state-dependent and frequency-dependent absorption characteristics emulating the behavior of a device deployed in the ocean [28],[32]. The software contains an obstacle switch command declared near the beginning of an input file identifying which device parameterization will be employed for the simulation. The user can choose to implement a constant transmission coefficient which reduces the wave spectrum by a uniform percentage based on the wave spectrum's significant wave height and peak period, or have each frequency bin individually modified within the spectrum. The results of the SNL SWAN software are validated with experimental array tests of 1:33 scale models of the Columbia Power Technologies' Manta 3.1 device [28]. Future releases of the

software will capture the effects of reflection and radiation [90]. A more in-depth review of SNL-SWAN's features is discussed in Section 3.2.

2.5 Model Selection

The spectral action density model was chosen as the most appropriate to model a WEC array's far field impact largely because it can propagate waves over a large domain with low computational expense. The aforementioned Boussinesq and Mild slope models solve for the instantaneous water surface elevation and resolve the complete horizontal and vertical flow velocity structures for each constituent wave. While the Boussinesq and mild slope models are suitable candidates for resolving radiation and diffraction around wave energy converters, their computational expense limits their use to domains a few kilometres wide, smaller WEC arrays and shorter time durations [31].

Resource assessments executed on large domains using these phase resolved models will be compromised by slow execution speeds. In addition to the high associated computational expense, these models suffer from numerical instabilities due to the stiff nature of their governing equations. The computational domains studied in Boussinesq and mild slope models are much smaller than those conducted in spectral action density models. For instance, the wave resource assessment conducted for the West Coast of Vancouver Island, Canada extends from the bottom of the Olympic Peninsula to just below Haida Gwaii. The area covers over 410,000 square kilometres with over 130,000 computational nodes [55]. The model is capable of simulating a full year of boundary conditions at a three hour resolution in less than two days on an eight core processor. In addition to the spectral action density model's computational efficiency, it is a tool that is familiar to the wave energy industry. Present day wave energy resource assessments are typically produced using spectral action density models [49], [55], [91]–[94].

As such, developing new methods for including WEC arrays within these models presents a natural progression in accepted practices for wave energy resource assessment [95]. Spectral action density models are capable of accounting for non-linear wave phenomena such as bottom friction, wave breaking, quadruplet and triad wave interactions. The use of source and sink terms to represent the aforementioned wave phenomenon can similarly be extended to the representation of a WEC within a spectral model.

The fundamental equations of all third generation spectral wave models (WAM, WaveWatch III, SWAN, etc.) are in essence the same. The most prominent difference between SWAN and the other spectral models is the numerical scheme used to solve the spectral action balance equation. SWAN's implicit formulation allows for larger time steps and higher spatial resolution across both structured and unstructured grids. SWAN is typically used for nearshore regions while the other models have been applied by meteorological agencies on a global scale [96]. In addition to the suitability of SWAN's model physics and computationally efficient numerical scheme, the software is open source which has resulted in its extensive academic and industrial use [87].

One of the largest criticisms faced by the selection of the SWAN model is that it is phase-averaged and hence cannot accurately represent a WEC's operation. Phase-averaged models by definition do not store information regarding whether two waves are in or out of phase with one another making phase-dependent processes such as radiation and diffraction difficult to represent explicitly within spectral-domain solvers such as SWAN [95]. Computing diffraction from fundamental phase dependent relationships requires considerable computing effort. However, a phase-decoupled approach [97] is employed in the SWAN model, which has been shown capable of portraying the spatial redistribution of waves caused by the phenomenon. The approximation is based on the mild-slope equation for refraction and diffraction omitting phase information [98].

Given advances made in modelling diffraction, it is conceivable that future work may identify candidate techniques for mimicking the effects of radiation in spectral action density models like SWAN with similar success if information of a WEC's motion could also be incorporated in the model's governing equations. Even without these future developments in hand, studies have suggested that phase information is irrelevant when realistic wave conditions and array configurations are considered [99].

Folley and Whittaker conducted a statistical analysis of WEC array interaction factors to determine how accurately phase information could realistically be calculated. Incident waves, the WEC array layout and the devices' dynamics were considered in this analysis. The authors determined incident waves are typically represented with two-parameter spectra which poorly represent bimodal sea states underlining the uncertainty in the model's boundary conditions [49], [99], [100]. In cases where wave spectra are generated

using a wave model, it should be noted that models are typically calibrated using H_s where uncertainties are typically 5% and wave periods have a root-mean squared error of approximately two seconds [99]. In real deployments, there will be uncertainty in the WEC's exact positions due to device drift and moorings. Furthermore, environmental conditions such as tides and currents can affect the transit time for a wave traveling towards a device changing the wave's phase relationship [99]. Lastly, variation in individual device motion can be restrained by differences in manufacturing tolerances and marine growth.

Given the uncertainty associated with a device's operation in real seas, it appears randomized phase is an adequate assumption when modelling WEC arrays under realistic conditions. In conclusion, the SWAN model is computationally efficient, capable of covering large domains and employing long time steps, familiar to the industry and has been proven to be adequate for modeling WECs given its phase-averaged nature. As such, the WEC characterization proposed in this thesis is implemented within SWAN.

Chapter 3

Wave Energy Converter Characterization

The obstacle command in SWAN was originally designed to represent breakwaters as straight line barriers that could be placed between gridlines within the modeled domain. An obstacle modifies the propagation of energy across a line proportionally to a user defined parameter. In the present SWAN formulation, this parameter is a simple percentage of energy transmitted, which can be arrived at either experimentally or with empirical formulations [68], [69].

In the case of WECs, numerically generated time series data (such as that generated in Section 1.7) provide a good understanding of how energy is removed from the incident wave field [18]–[22]. However the challenge arises in being able to chart this understanding in a simplified representation (something at the fidelity of a SWAN model's representation of the wave conditions) that can be used to adjust the obstacle's parameters on-the-fly to model the frequency and direction dependencies of the WEC's performance.

This chapter presents a detailed review of how a WEC is presently represented in SNL SWAN. The remainder of this Chapter develops a method with which to increase the

fidelity of the device's energy conversion process, ultimately capturing the interaction between the incident wave and the primary interface. In Section 3.4 an energy balance analysis is presented that examines how time domain data defining the forces acting between the WEC, the incident waves and the radiated waves can be processed to determine the total energy transfer to the WEC, the energy lost to dissipative effects (eg. drag) and the energy returned to the surroundings as radiated waves. An overview of the different forces acting between the wave, and the subsequent exchanges of mechanical work between the two entities, and the WEC are presented in Section 3.5. In Sections 3.6 and 3.7, the outputs of the energy balance analysis are transformed into two new proposed obstacle cases – obstacle case five and obstacle case six which are each a form of meta-model of the wave-WEC interaction.

3.1 Existing Methods for WEC performance characterization

Within SNL SWAN, a wave energy converter's representation has been crafted based on WEC performance data generated by a WEC developer. This data is generally in the form of power matrices or relative capture width curves (RCWs). A power matrix is a table of average mechanical power produced by a WEC over a range of sea states. Sea states are typically characterized by parameters derived from spectral moments (defined below). Power matrices for WECs have been characterized by the significant wave height and peak period of the incident sea in order to work within the framework previously outlined by Sandia National Labs, although energy period has been recommended by IEC standards [33]. The significant wave height was traditionally defined as the mean wave height of the highest third of waves, however, as sea states are being resolved by their wave spectra, it is defined as four times the standard deviation of the water surface elevation [4]:

$$H_s = 4\sqrt{m_0} \tag{7}$$

where the spectral moment of n^{th} order, m_n, uses Eq. (8) when calculating from the non-directional variance density spectrum using:

$$m_n = \sum_i f_i^n S_i \Delta f \tag{8}$$

where Δf is the frequency increment and f_i^n is the i^{th} frequency to the n^{th} power.

The peak period, T_p is the wave period with the highest energy and is defined as:

$$T_p = \frac{1}{f_p} \tag{9}$$

where f_p is the frequency bin with the greatest variance density in the spectrum. RCW curves present a WEC's relative power absorption at different frequencies [65]. Each entry in a RCW curve is a ratio of the power absorbed to the incident power available in the sea [65]. Each entry in a performance matrix is for a group of irregular waves while the RCW curve tracks performance across a series of independent, regular waves.

An example of the performance matrix and the RCW curve are presented in Figure 19 and Figure 20 respectively. The data provided in Figures 19 and 20 is only a portion of the energy extraction completed by the WEC; these figures show the power produced by the PTO – not the power that was extracted from the wave itself. As they do not show the full value of power extracted from the incident wave, these tabulations cannot wholly account for a device's hydrodynamics in a coastal model.

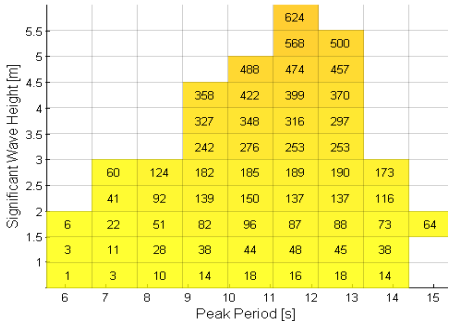

Figure 19: Typical power matrix in which the power captured by the device is reported in a bin corresponding to a sea state characterized by an H_s and T_p

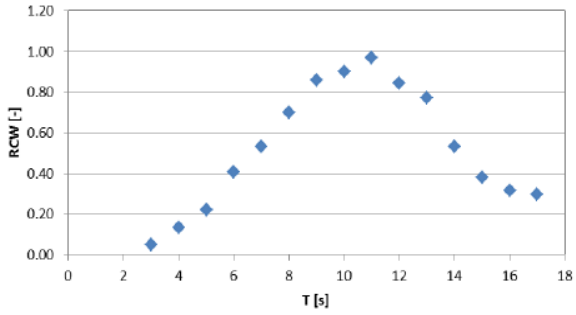

Figure 20: Typical RCW where the percentage of power captured by the device is reported as a function of incident wave frequency [65]

RCW curves are typically generated by performing regular wave tank tests for waves of different frequencies. From these tests, a monochromatic or polychromatic capture width curve can be derived [11]. Price has demonstrated the capture width in irregular seas is lower than in a monochromatic sea of corresponding period [11]. As such, directly employing an experimental monochromatic RCW curve would overestimate the device's power capture in an irregular sea.

Within the wave energy community at large there is a tendency to use the term ‘power absorbed’. This term can be used to describe a number of power phenomena – be it the power that is transferred to the device’s exterior hull (manifesting in kinetic energy), or the power captured by the device’s PTO (manifesting in a useful energy commodity like electricity or pressurized fluid). This overarching use of power absorbed has resulted in confusion as to which power capture stage is being referenced. In an effort to settle any confusion surrounding the discussion of power capture, Price outlines four stages over which a device captures power [11], as pictorially represented in Figure 21.

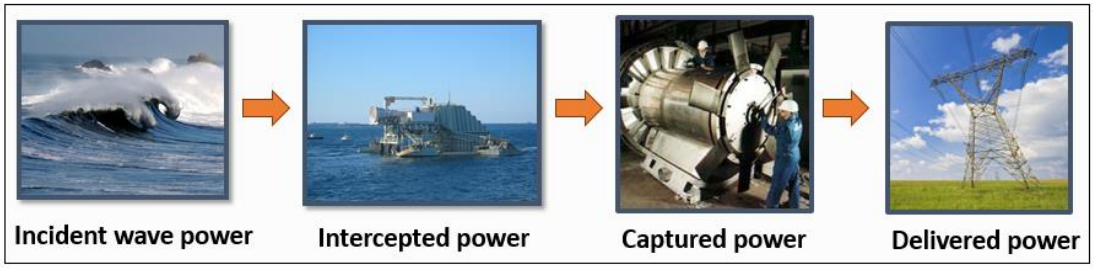

Figure 21: Power transfer stages of a WEC [11]

The ‘intercepted power’ is defined as the power flow between the incident wave and the device’s primary interface [11]. Kinetic and potential energy in the incident wave perform work on the hull of the WEC creating kinetic energy in the WEC structure. The WEC’s kinetic energy does work on the surrounding fluid and radiates new waves while non-linear hydrodynamic forces (drag) dissipate kinetic energy from both the incident wave and the WEC.

Some kinetic energy in the WEC is subsequently stored in the short term as potential energy and some is fed into the PTO. The energy flow through the PTO is defined as the ‘captured power’. Captured power is the rate of production of a useful energy commodity.

Finally, there is the power flow between the PTO output and the final product used by the consumer, the ‘delivered power’, which is generally electricity but other commodities could be pressurized air, desalinated water, pressurized hydraulic fluid, etc. A WEC’s delivered power is the final output of a series of energy conversion processes.
When attempting to model the interaction of a WEC with the incident wave, it is obvious that the hydrodynamic losses and the power transferred back into the water via radiated

waves must be accounted for if a WEC array is to be modeled accurately. Unfortunately, these energy fluxes are either not tabulated by WEC developers, or not made publically available.

This chapter seeks to address two central challenges outlined in the preceding paragraphs. For one, a new device representation is proposed to capture the varying degrees of complexity in a WEC's operation. While a linear, offshore structure can be effectively represented in the spectral domain with a single percentage of energy transmitted or reflected, a dynamic device is more difficult to accurately represent since the levels of intercepted, captured and delivered power vary greatly with the incident wave conditions (eg. frequency, direction, wave height, etc.). Secondly, the metrics with which the device's power capture is reported is placed under critical review. The author proposes the use of the intercepted power as a means with which to characterize the device's impact on the surrounding waves. Using intercepted power to represent the WEC device includes hydrodynamic losses and the power radiated by the device back into the fluid domain.

3.2 Existing SNL SWAN Obstacle cases

In SWAN, the location of an obstacle is defined by a sequence of node points used to represent line segments. Obstacles interrupt the propagation of the waves from one grid point to the next [101]. This interruption can be in the form of wave reflection, wave absorption or even a wave source, such as the injection of energy at a new frequency when a device radiates waves.

In SWAN's representation of static obstacles, the transfer of energy through an obstacle is defined by the user with a transmission and or reflection coefficient. A transmission coefficient extracts a ratio of incident wave energy in space, as seen in Eq. (10). This coefficient is traditionally the ratio of H_s incident to the obstacle and H_s in the lee of the obstacle [102]. However, given energy is proportional to H_s^2, the transmission coefficient, K_t is also squared in Eq. (10). The transmission coefficient is applied at linkages between nodes across which action density propagates, as such it is applied to the spatial derivatives of the action density formulation previously employed in Eq. (6):

$$\frac{\partial N(\sigma,\theta)}{\partial t} + c_x \frac{K_t^2 \partial N(\sigma,\theta)}{\partial x} + c_y \frac{K_t^2 \partial N(\sigma,\theta)}{\partial y} + c_\theta \frac{\partial N(\sigma,\theta)}{\partial \theta} + c_\sigma \frac{\partial N(\sigma,\theta)}{\partial \sigma} = \frac{S}{\sigma} \qquad (10)$$

where K_t is the transmission coefficient.

SNL-SWAN currently characterizes a WEC using either the aforementioned power matrix or RCW curve. Each obstacle case uses one of these data sets to generate a transmission coefficient allowing for the extraction of energy from the incident sea [103]. When a captured power matrix is employed, the wave energy transport at the node incident to the obstacle line is first calculated. The H_s and T_p are calculated from the incident spectrum. Bilinear interpolation is used to find the respective power captured for the corresponding sea state [65]. The energy flux incident to the obstacle is the sum of the potential and kinetic energy being transported by a wave in the direction of wave propagation:

$$\mathrm{J} = \int\int c_g E(\sigma,\theta) d\sigma d\theta \tag{11}$$

$$E(\sigma,\theta) = \frac{\rho g}{2}\eta^2(\sigma,\theta) \tag{12}$$

where J is the omnidirectional wave power transport also referred to as energy flux. The energy density can be derived from the spectral action density equation. Action density is typically used in SWAN's formulations as it is conserved in the presence of currents while energy density is not [84]. Action density and energy density are related by frequency:

$$N(\sigma,\theta) = \frac{E(\sigma,\theta)}{\sigma} \tag{13}$$

The transmission coefficient (K^2_t) [32] is used to characterize the device's power capture for a particular wave condition. The transmission coefficient is simply a ratio:

$$K_t^2 = \frac{P_{Lee}}{P_{Inc}} = 1 - \frac{P_{cap}}{J \cdot w} \tag{14}$$

where P_{Inc} is the energy flux incident to the device, and P_{Lee} is the remaining energy flux in the lee of the device, P_{cap} is the power captures by a device's power take-off and *w* is the width of the device. Within the calculations of a SWAN model, the transmission coefficient is calculated by interpolating the captured power from a power matrix. The captured power is normalized against the total incident wave energy flux. The total incident wave energy flux is scaled by the characteristic width of the device. The width parameter is subject to debate as a device can intercept more power than is present in the

length of wave crest corresponding its own width. The remainder of the energy flux is assumed to pass through the device thus defining the percentage of power transmitted. When an RCW curve is employed to characterize device performance, the transmission coefficient is found by subtracting one from the relative capture width indexed for the T_p incident to the WEC. By employing a RCW curve, the device developer has already decided what *w* should be as RCWs are reported as a percentage of the incident energy captured from the surrounding sea as a function of frequency.

The way the transmission coefficient is used in SNL-SWAN depends on the obstacle case selected. Within SNL-SWAN, the user has the option to use one of five WEC representations, referred to as *obstacle cases*.

Obstacle case zero corresponds to the standard SWAN obstacle command which extracts a certain percentage of the incident wave energy applied across all sea states and frequencies.

Obstacle case one uses a power matrix to calculate a transmission coefficient dependent on the significant wave height and peak period of the incident sea state. The same coefficient is applied uniformly across all frequencies in the energy density spectrum [65].

Obstacle case two employs an RCW curve to calculate a constant transmission coefficient across all frequencies [65]. The peak frequency (T_p^{-1}) incident to the device is found within the RCW curve input by the user. Obstacle case two was not investigated in this analysis. Although regular wave simulations could have been run in the time domain simulator, the computational expense of these tests was deemed too high given these tests would not be representative of a device's behaviour at sea.

Obstacle case three employs a revised power matrix to determine the transmission coefficient for each frequency bin in the incident energy spectrum. The input to this module differs from that of obstacle case one. The axes along the edges of the power matrix are H_s and period (T), opposed to the H_s and T_p used in obstacle case one. SNL-SWAN determines the H_s incident to the device. The row in the power matrix is then used as an RCW curve. A separate transmission coefficient is determined for each entry in the RCW curve and then applied to the respective frequency in the incident variance

density spectrum [90]. Obstacle case three requires the construction of a modified power matrix generated from experimental tests that are not commonly used in practice [104].

Obstacle case four employs an RCW curve to determine a transmission coefficient for each individual frequency bin. These values are independent of the incident sea state [65]. As previously outlined, applying a monochromatic RCW curve will overpredict the device's optimal performance at certain frequencies [11]. A more detailed description of each of the existing obstacles are present in the SNL-SWAN User Manual available on the SNL-SWAN website [32].

In general, the author has concluded power matrices better characterize a device's performance because they are indexed against more spectral characteristics of the incident, polychromatic sea state, and thus a power matrix should give a more accurate measure of captured power. The new WEC representations presented later on in this chapter will only be compared to obstacle case one.

3.3 Limitations in Existing SWAN WEC Representations

There are three chief weaknesses in the representation of WECs in SNL SWAN, the first stems from the device's geometric representation while the second and third result from the data used to characterize the device. The device is represented with a line of a specified device width orthogonal to a grid node. Given directionality is not considered in this analysis, having the user input angled devices into the model domain could lead to erroneous results. During SNL-SWAN execution, a directional spectrum is stored at the incident node. For each bin of the incident spectrum, the directional energy transport can be calculated and projected into x and y Cartesian components, as presented by the dark blue vectors in Figure 22. A transmission coefficient is applied between two adjacent nodes, representing the WEC partially absorbing the energy moving between those two nodes. The WEC only affects the energy incident to the device and as such, the transmission coefficient is applied only to the x-projection of the wave energy vectors presented in Figure 22. The representation of a WEC as a line becomes problematic for certain geometries or device configurations. For attenuator devices such as Pelamis for instance, the device is narrow but very long, when represented as a line, the device will inevitably absorb more power than is available at the incident node since the total incident energy flux is set by the node spacing of the SWAN grid. That node spacing is

set based on preconceived notions of what the WEC device's actual width *w* is. As mentioned earlier, for some choices of *w* the RCW can be greater than one. This shortcoming will be further discussed in Section 5.1.1 and will not be addressed in this thesis.

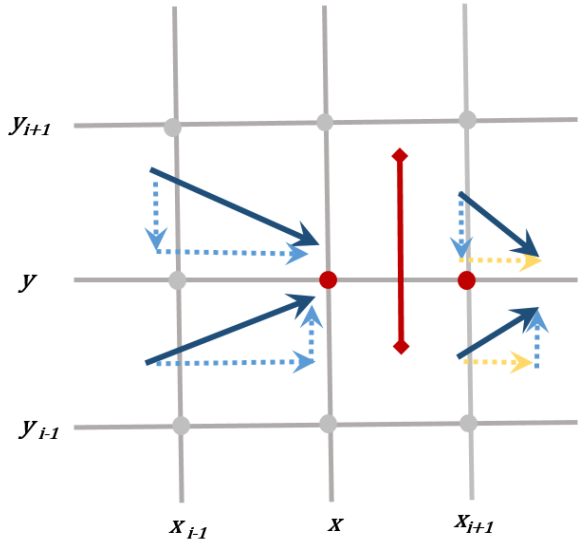

Figure 22: Representation of an obstacle within SWAN. The device is represented as a line across which energy can be transferred. A transmission coefficient is applied to the x projection of the incident energy (energy propagated perpendicular to the obstacle) while energy in the y-projection is not impacted by the device's operation.

The second limitation in the device's representation is that directional information concerning the incoming waves is ignored. The omnidirectional power transport is used to determine a transmission coefficient which is then applied to each of the directional bins in the energy spectrum. A further discussion on how the incident power transport in *obstacle case five* and *six* is presented in Sections 3.6 and 3.7 respectively.

The third limitation in the device's representation is the user provided information used to characterize the device. The reliance of Obstacle cases 0 through 4 on developer supplied captured power matrices and RCW curves raise questions concerning the accuracy of the existing SNL SWAN WEC representations. Developers must supply performance information to clients and regulators to develop projects and thus this level of data is easy to attain. The derivation of a transmission coefficient from this data alone assumes that any effect the WEC has on the surrounding sea state is represented solely by

the captured power. In short, by using these pre-existing parameterizations perfect conversion from incident to mechanical power is assumed, and the energy removed from the incident waves is likely to be underestimated.

3.4 Device Power Balance

The contributions of power leaving and entering the WEC device are presented in Figure 23. The power contributions on the left hand side correspond to the power entering the device from the fluid domain. The power contributions on the right correspond to power leaving the device. There are two pathways that can be taken when power leaves the device. Firstly, power can permanently leave the system, as is done when mechanical power is extracted through the PTO. Second, power can be transferred back to the device. For instance, a device can work off of its own radiated wave, or in the case of drag, the direction of power transfer depends on the device's relative velocity to the surrounding fluid.

Within the control volume of the reference WEC there are also internal oscillation of potential and kinetic energy between the device's two bodies. Even though this internal energy transfer can be extracted from the time series data, there is no need to do so as no additional information concerning the device's impact on the surrounding fluid is gained.

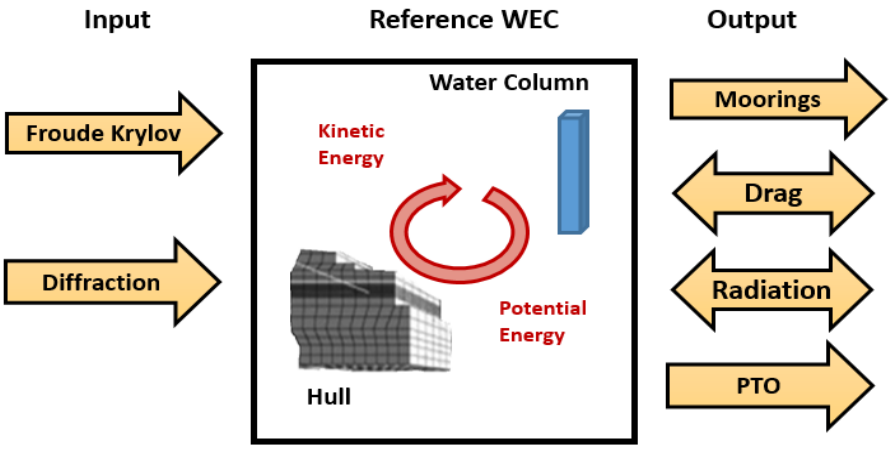

Figure 23: Visual representation of a device's power transfer. Kinetic and potential energy is transferred between the reference WEC's two bodies. The yellow arrows indicate the direction of power transfer into and out of the reference WEC.

3.5 Force and Power Contributions during Device Operation

The following section describes the nature of the models employed by the time domain simulator to calculate the forces acting on the reference WEC. This is necessary in order to give the reader a sense of the inevitable modelling errors and how they may influence the final power balance. First, the Equations of Motion for a surface piercing rigid body is described in Section 3.5.1. This explanation is followed by a description of the individual force calculations and their extension to power transfer.

3.5.1 Equations of Motion

The dynamics of a semi-submerged WEC can be described by the Equations of Motion for a floating, surface piercing, rigid body. Equation (15) describes the equations of motion for each of the reference WEC's two bodies:

$$\boldsymbol{M}\ddot{\boldsymbol{x}}(t) + \boldsymbol{A}(\infty)\ddot{\boldsymbol{x}}(t) - \int_{\boldsymbol{0}}^{\boldsymbol{t}} \boldsymbol{k}(t-\tau)\dot{\boldsymbol{x}}(\tau)d\tau - \boldsymbol{C}\boldsymbol{x}(t) - \boldsymbol{F_{PTO}}(t) \\ -\boldsymbol{F_m}(t) - \boldsymbol{F_v}(t) - \boldsymbol{F_{ir}}(t) = \boldsymbol{F_E}(t) \tag{15}$$

where $\boldsymbol{M}$ is the mass of the object, $\boldsymbol{A}(\infty)$ is the object's added mass at infinite frequency. Both these variables are 6 x 6 matrices indicating the body's mass and added mass in each DOF. The degrees of freedom include three translational modes and three rotational modes which are described in further detail in Table 3. The variable $\boldsymbol{k}(t-\tau)$ is an object's impulse response kernel, $\boldsymbol{C}$ is the object's 6 x6 hydrodynamic stiffness matrix, and finally $\boldsymbol{x}$ is a 6 x 1 vector indicating the device's position in six DOF. $\boldsymbol{F_{PTO}}$ represents the damping forces and moments induced by the power take-off (PTO). $\boldsymbol{F_m}$ represents the damping forces exerted by the moorings in the translational degrees of freedom. $\boldsymbol{F_v}$ represents the damping forces and moments induced by viscous drag. $\boldsymbol{F_{ir}}$ represents the internal reaction forces induced by the second body on the first which can at times lead to energy permanently being dissipated due to internal drag. Finally, $\boldsymbol{F_E}$ corresponds to the excitation force and moments induced by the incoming wave. Each of the terms $\boldsymbol{F}$ are 6 x 1 vectors with the first three entries corresponding to forces acting on the device in surge, sway and heave, and the last three entries corresponding to moments acting on the device in roll, pitch and yaw. Certain rotational degrees of freedom may have negligible moment contributions due to the irrotational fluid assumption, which will be further addressed in the remainder of Section 3.5. The power transfer due to these

loads is calculated by an inner product on the instantaneous force and velocity. The power transfer and equations of motion for the hull are demonstrated in the heave degree of freedom in the following section and can be applied by analogy to the light piston representing the internal water. The equations can be applied to each relevant degree of freedom, as specified in the following sections.

3.5.2 Power Transfer due to Wave Excitation

The excitation force is the sum of the pressure exerted across the body due to the presence of the incident and diffracted wave which can also be defined as the sum of the Froude-Krylov and scattering forces. The Froude-Krylov force, defined as the force due to the pressure field of an undisturbed wave[45], while the scattering force is the pressure field due to the wave diffracting around the body. Due to linear superposition, these combine to form the excitation force:

$$F_E = \int_{\boldsymbol{s}} p(s)\, n dS \tag{16}$$

where $p(s)$ is the pressure across the surface of the object[16], n is the normal vector to the surface, and s is the surface of the body. The excitation force is only applied in the translational degrees of freedom as flow is assumed to be irrotational. ProteusDS calculates the incident loading at any given moment in time, based on the wave amplitude, relative heading, phase offset and wave frequency of the incident wave for each degree of freedom [50]. The incident loading generated from each regular wave component of the irregular sea state and the total incident wave spectrum is summed together to generate a time series of the excitation force. This excitation force, F_E, is then multiplied by the velocity of the body:

$$P_{inc,b} = F_E \cdot \dot{x}_B \tag{17}$$

to determine the power from excitation imparted on each body (the hull or the piston).

3.5.3 Power Transfer due to Radiation

The radiation force results from the body oscillating in the absence of an incident wave [45]. The radiation force at any given moment in time is calculated from the convolution

[16] The pressure is the sum of the pressure from the incident wave and the scattered wave.

of body motions at previous time steps with impulse response kernels and the added mass at infinite frequency multiplied by the acceleration of the body [54]. The total radiation force is the sum of two calculations done in parallel. The radiation force exerted by the body and the piston onto the external waves is calculated within ProteusDS. The second radiation force is calculated within Simulink and corresponds to the internal radiation force between the piston and the body and the radiation force exerted by the body onto the piston. The radiation components are delineated in the heave equation of motion:

$$M\ddot{x}(t) + \underbrace{A(\infty)\ddot{x}(t)}_{R1} - \int_0^t \underbrace{k(t-\tau)\dot{x}(\tau)d\tau}_{R2} - Cx(t) - F_{PTO}(t) \\ -F_m(t) - F_v(t) - F_{p,v}(t) = F_E(t) \tag{18}$$

where R_1 is the radiation component corresponding to the added mass at infinity and R_2 is the force calculated with the impulse response kernel from the added damping values. Radiation is present in all six degrees of freedom. The added damping and added mass at infinity parameters are calculated in WAMIT, as outlined in Section 1.5.1. WAMIT returns 6 x 6 matrices for $\boldsymbol{A}(\infty)$ and the kernel functions to calculate the force and moment acting on the body due to radiation at any point in time. The motion of the water column within the OWC's air chamber results in a force radiated onto the hull as well as a force exerted onto the water column as it induces motion in the otherwise still water. Separate added mass and damping coefficients determined through generalized modes, as described in Section 1.5.3, were entered into Simulink in order to determine the radiation contributions between the hull and the water column. The total radiation forces acting on the OWC are a sum of the radiation produced by the hull, and the radiation produced by the piston. The power associated with radiation is found by multiplying the radiation forces by each body's respective velocity to determine the radiated power exerted on each body:

$$P_{RAD,b} = (R_1 + R_2) \cdot \dot{x}_B \tag{19}$$

The radiated power is negative when it is acting on the fluid surrounding the device.

3.5.4 Power dissipated through Moorings

Mooring forces are calculated in ProteusDS using a cubic-spline lumped mass cable model [51]. The model accounts for each cable segment's material properties such as the bending, flexural, torsional and axial rigidity [20]. The finite element discretization

evaluates viscous drag forces, and internal bending, torsional and axial forces at each node point within a cable for its mass and frequency independent added mass. A more detailed account of the cable dynamics can be found in the ProteusDS manual [50], [51]. This mooring force is multiplied by the cable's velocity where it is attached to the body for each linear DOF. The power dissipated from the moorings is found with:

$$P_{moor} = F_{moor} \cdot \dot{x}_C \tag{20}$$

Where P_{moor} is the power dissipated through the moorings and $\dot{x}$ describing the velocity of the cable at its insertion points at the device. The force and power associated with the moorings is only found in the translational degrees of freedom in ProteusDS.

3.5.5 Power Transfer due to the PTO

The OWC is modeled as a dynamic system that is coupled to the thermodynamics of an air chamber. The hull of the device is modeled as a six DOF body and the water column within the chamber is simulated as a piston resting on the water column [20]. The hull and piston were modeled in the time domain. The mean mechanical power produced by the OWC in each sea state was determined from the product of the force between the two bodies and their relative velocity. The force on the water column was calculated from the area of the air chamber and the pressure differential between the air chamber and atmosphere, with the force on the hull being equal and opposite to this.

3.5.6 Power Transfer due to Viscous Drag

The drag forces experienced by the OWC are calculated for each panel of the body's mesh that is below the undisturbed water surface elevation. The force of drag is calculated using the relative velocity between the fluid and the device. Empirical coefficients are used within ProteusDS in order to calculate the drag force. Given the OWC's typically low Keulegen-Carpenter number, a drag coefficient of three is used based on experimental results for a rectangular cylinder in oscillatory flows [20], [105]. The drag force acting on the device is defined by:

$$F_v = \frac{1}{2}\rho C_d A_{proj}(\dot{x}_B - \dot{x}_W)|\dot{x}_B - \dot{x}_W| \tag{21}$$

where A_{proj} is the projected area of the mesh panel, C_d is the drag coefficient, $\dot{x_B}$ is the velocity of the device and $\dot{x_W}$ is the velocity of the water. The drag force is found in all

translational and rotational degrees of freedom however the angular velocity of the water was assumed to be zero as a result of the irrotational flow assumption.

The direction in which the drag force is acting depends on the relative velocity between the device and the surrounding fluid. Drag is inherently different from the other forces previously discussed in this section because it transfers power not only between the wave and the body, but also dissipates power to the surrounding fluid in the form of a wake.

Power transfer is dependent on the magnitude of the power associated with each agent as well as the direction in which each agent is moving, as is illustrated in Figure 24.

In order to isolate the energy that is being transferred to the device from the fluid and vice versa, the time series of the power induced by drag was separated into contributions inducing motion and contributions resisting motion as a result of three power transfer scenarios which are dependent on the relative velocity between the device and the water. Power is always transferred from the medium with greater energy to that of lower energy. An equivalent magnitude force is applied upon either agent (body or water), with only a change in direction implying the direction of power transfer (body to water, or water to body) which can be determined based on the relative velocity of these bodies.

The general power transfer equation is presented in Eq. (22). When the velocity of the water is greater than that of the body the fluid is transferring power to the body, thus inducing motion (*im*). In the second scenario presented in Eq. (22), the velocity of the water is less than that of the fluid, meaning the device is resisting the motion of the fluid and power is being transferred back into the wave. In each case, some of the power transferred between the fast body and the slower body is being permanently dissipated to the ambient fluid. In the third scenario, if at any point in time the velocity of the body and fluid are the same, no power is transferred between the two mediums.

$$P_{drag,y} = F_v \cdot \dot{x}_B \begin{cases} y = im & (\dot{x}_w - \dot{x}_B) > 0 \\ y = rm & (\dot{x}_w - \dot{x}_B) < 0 \end{cases} \quad (22)$$

In addition to the drag associated with the body, there is an additional drag force associated with the fluid. The fluid drag is defined as:

$$P_{drag,f} = F_v \cdot \dot{x}_W \quad (23)$$

where power is being transferred back into the fluid as a wake. The direction of power contributions from the body and the water based on the direction and magnitude of each body's velocities are illustrated in Figure 24.

It should be noted that work that is done on the incident wave, is lost within the present formulation in the time domain simulator. ProteusDS does not increase the energy in the incident wave based on the drag force, which may be a source of error in the power balance presented in Section 3.5.7.

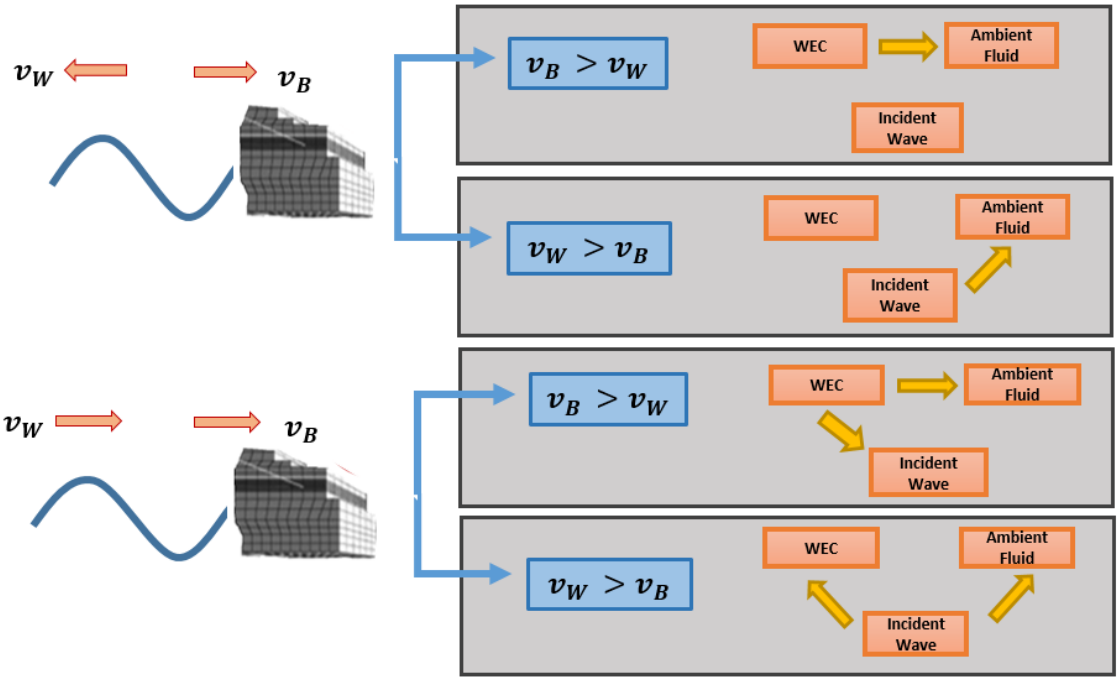

Figure 24: Scenarios in which power can be transferred from one medium to another as a result of drag. v_B is the velocity of the body, v_W is the velocity of the water.

3.5.6.1 Power from Internal Reaction Forces

The internal drag of a fluid within the OWC's body is comprised of viscous losses, turbulent losses and vortex transport [20]. A representative drag coefficient of 0.02 was used to represent the drag experienced by oscillating flows in a cavity without significant wake [20], [106]. The cavity drag was calculated within Simulink and is defined as:

$$F_{p,v} = -\frac{1}{2}\rho\, A_{B,int} C_{p,d} \left(\dot{x}_p - \dot{x}_B\right)|\dot{x}_p - \dot{x}_B| \tag{24}$$

where $A_{B,int}$ is the area of the wetted interior in the OWC, $C_{p,d}$ is the internal drag coefficient, $\dot{x}_p$ is the velocity of the piston and $\dot{x}_B$ is the velocity of the body. The power that is dissipated by internal reaction forces (drag transferring power between the two bodies) is then dissipated to the ambient fluid as a wake is calculated using:

$$P_{int,p} = F_{p,v} \cdot \left(\dot{x}_p - \dot{x}_B\right) \tag{25}$$

The heave force and power presented here can be further extended to the internal reactional forces in all translational degrees of freedom.

3.5.7 Device Meta-model

The hydrodynamic impact of the device on the surrounding fluid can be characterized by the power absorbed by the device which is defined as the difference between the power incident to the device, and the power radiated from the device:

$$P_{Abs} = \overline{\overline{P_I}} - \overline{\overline{P_R}} \tag{26}$$

where the total power incident to the device is defined in Eq. (27) and the total radiated power is defined by Eq. (28). The total wave power incident to the device is a sum of the incident wave contributions and the power contributions of drag inducing motion:

$$\overline{\overline{P_I}} = P_{inc,p} + P_{inc,h} + P_{drag,im} \tag{27}$$

where $P_{inc,p}$ is the product of the incident loading force on the piston and the velocity, $P_{inc,h}$ is the product of the incident loading on the OWC hull and the velocity of the hull, $P_{v,pos}$ is the product of the positive contribution of the viscous drag on the body and the body's velocity. The total power radiated by the device into the surrounding fluid domain is the sum of the radiation and cross radiation power contributions defined by

$$\overline{\overline{P_R}} = P_{rad,p} + P_{rad,h} + P_{rad,p2h} + P_{rad,h2p} \tag{28}$$

where $P_{rad,p}$ is the product of the radiated force of the piston and the velocity of the piston, $P_{rad,h}$ is the product of the radiated force of the body and the velocity of the body, $P_{rad,p2h}$ is the product of the radiated force the piston exerts on the body within the OWC air chamber and the velocity of the piston, $P_{rad,h2p}$ is the product of the radiated force the OWC body exerts on the piston and the velocity. The cross radiation terms are only present in the translational degrees of freedom.

The total incident and the total radiation power terms are input into SNL-SWAN as separate input files. The power absorbed is determined internal to SNL-SWAN based on the parameters set by the user. As previously presented in Figure 23, the power absorbed (which includes power dissipated and mechanical power produced) includes:

$$P_{ABS} = P_{PTO} + P_{drag,f} + P_{drag,rm} + P_{moor} + P_{int,p} \quad (29)$$

The total power absorbed by the device and its constituents are the foundation upon which obstacle cases five and six were built. Theoretically, either side of the power balance can be used represent a device's hydrodynamics.

3.5.8 Validation of the Power Flow Calculation

The power balance presented in Eq. (26) was carried out for each sea state in which the reference device was modelled. In general, there was good agreement between the two methods with an average root mean squared error of 4.0% between the left and right hand sides of Eq. (26). Most of this error is present in sea states with low H_s values (less than two metres). A portion of the errors reported in Figure 25 can be attributed to the inexact calculation of the fluid drag force. The velocity of the water could only be obtained at the device's center of gravity which in reality varies along the different panels of the device's mesh.

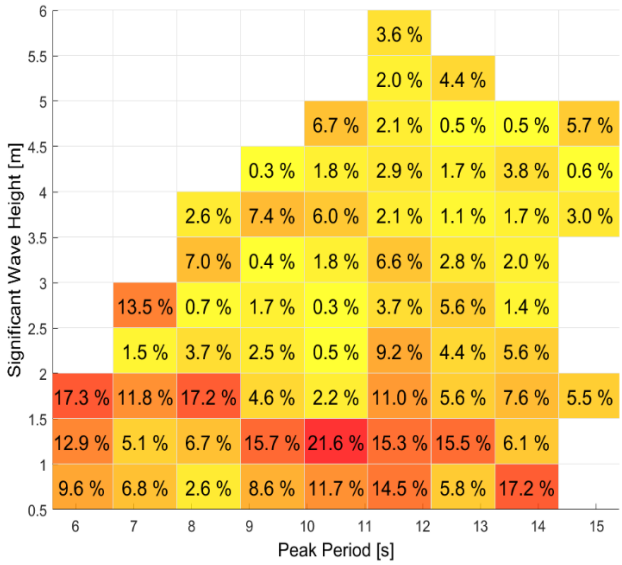

Figure 25: Root mean squared error between the right and left hand sides of the power balance formulation

3.6 Obstacle Case Five

Applying a transmission coefficient calculated from the ratio of the incident wave power and captured power implies perfect conversion from incident to mechanical power. In real seas, this assumption can lead to erroneous representations of the far field impact of a WEC array. *Obstacle case five* seeks to remedy this oversight by using the device meta-model generated in Section 3.5.7 to represent a device in a way that is simple enough to keep SWAN computationally efficient but also capture's the device's hydrodynamic impact on the surrounding fluid domain.

Obstacle case five is very similar in structure to that of the previous obstacle cases created by SNL. The device is represented as a line, as depicted in Figure 22 and applies a constant transmission coefficient across each frequency and directional bin of the variance density spectrum propagating incident to that line. The difference in the newly proposed obstacle case lies in which parameters are used to calculate the obstacle transmission coefficient. The transmission coefficient is determined by the ratio between the total power absorbed by the device and the power in the waves. The power absorbed can be defined as either the right hand side or left hand side of Eq. (26), depending on the information the user has available. The power in the waves is calculated by taking the projection of the incident wave energy flux in the direction perpendicular to that of the obstacle in SWAN.

Theoretically, the user could characterize radiation as a process that occurs both incident to and in the lee of the device. Representing a device as both a source and a sink more realistically describes the device's behaviour by expressing the device's absorption and radiation of power. This method is invoked when the user specifies the inclusion of radiation in the model's start-up switches. An addition radiation case (*radcase*) switch has been added to the SNL-SWAN control file for this purpose.

When the radiation case switch is enabled, the transmission coefficient is alternatively defined as:

$$K_{t,F} = \kappa_{t,inc} - (1 - \gamma_{rad}) \cdot \kappa_{t,rad} \tag{30}$$

where $\kappa_{t,inc}$ is calculated from the ratio of the incident power to the device and the power in the waves, $\kappa_{t,rad}$ is calculated from the ratio of the radiated power, specified in the

radiated power matrix and the power in the waves and finally γ_{rad} is the user-specified percentage of power radiated back towards the incident wave.

Additionally, K_r is calculated which is defined as the percentage of power in the waves that is reflected from the device. The reflection coefficient is used to represent power that is being put back into the fluid domain by the device through radiation and is defined as:

$$K_r = \gamma_{rad} \cdot \kappa_{t,rad} \tag{31}$$

This approach is consistent with the way energy transmission is represented in SWAN, however not necessarily consistent with the way radiated power is transferred physically. As a result, the shape of the radiated wave field will be a scaled representation of the incident wave field.

There are logistical constraints associated with employing *obstacle case five* where too much power can be removed from the system if not enough radiation is put into the lee of the device and the transmission coefficient exceeds one. A transmission coefficient greater than one implies that the device is taking more power out of the sea than is physically available. As such, in order to properly employ the radiation case programmed in by the author, the condition presented in Eq. (32) must be true.

$$K_r + K_t < 1 \tag{32}$$

The power absorbed by the device is determined by calculating the difference between the energy available at the incident node and the energy radiated or transmitted to the next node. If $\gamma_{rad}$is set to one, the device acts as a sink, and will only be able to take energy from the waves propagating towards the device. In this characterization, two transmission coefficients are calculated. The traditional power matrix used in obstacle case one, is used to determine the captured power produced by a device. This transmission coefficient $K_{t,PTO}$ is used by SNL-SWAN to determine the captured power produced by each device in the simulation and is output to the user in a text file. A second transmission coefficient $K_{t,F}$ is calculated using the novel power absorbed matrix. The ratio between the power absorbed and power in the waves is used to generate a transmission coefficient which is applied to the wave spectrum as it crosses an obstacle and is used to determine the far field impact of the device.

3.7 Obstacle Case Six

While *obstacle case five* is able to represent the device's hydrodynamic impact on the surrounding wave climate, it still cannot resolve how a device responds to waves of different frequencies. Since most devices are tuned to a particular frequency bandwidth, frequency dependence is crucial when characterizing the performance of a device. RCW curves were previously used by SNL to characterize devices in obstacle cases two and four which parameterize a device's performance in regular waves according to its frequency. Even though a device is represented as a linear system, it is difficult to justify using an RCW curve to characterize a device's performance in irregular waves. In regular waves, resonance at certain oscillation frequencies can overestimate a device's performance.

As a device encounters different sea states, it is expected that its performance at each frequency will also change. In order to account for this variability in operation, an RCW matrix is proposed as an input into obstacle case six which captures the frequency dependent performance of a device in each incident sea state. Given the performance of a device is based on the H_s, T_p and now frequency/period, an additional dimension is added to the power matrix. The relative capture width matrix can be most simply described as a three dimensional array as presented in Figure 26.

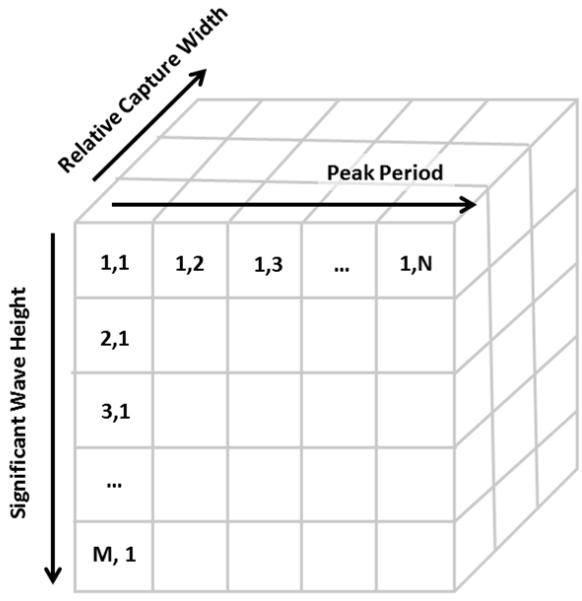

Figure 26: Visual representation of the relative capture width matrix structure

The variables M, and N correspond to the number of H_s and T_p bins used to characterize the sea states that occur over the course of a representative year. The RCW matrix stores transmission coefficients for a user-defined number of periods along the axis extending into the page. The periods specified by the user can vary between sea states and do not have to be evenly distributed. A transmission coefficient is linearly interpolated from the curve for each frequency bin within the SWAN simulation. Section 3.7 describes how the RCW matrix is generated.

Obstacle case six is very similar to *obstacle case five*. Both modules characterise a device based on the total power intercepted by the device, rather than the captured power. The two modules differ primarily in that *obstacle case six* assigns a different transmission coefficient, $K_{t,F}$ to each frequency, and that the RCW matrix is a pre-calculated ratio when it is input into SNL-SWAN, opposed to absolute power stored in the power absorbed matrix.

In *obstacle case six*, a transmission coefficient $K_{t,PTO}$ is calculated using a power matrix, as outlined in Section 3.6. The second transmission coefficient $K_{t,F}$ is found by bilinearly interpolating the first two dimensions of the RCW Matrix. A row corresponding to the device's frequency dependent operation has been identified. A transmission coefficient $K_{t,F}$ is interpolated for each frequency bin used in the SNL-SWAN model

3.7.1 Relative Capture Width Matrix Generation

The following section provides a detailed description of how one can generate an RCW Matrix from the time series data provided by the device architecture models outlined in Section 1.3. Traditionally, an RCW curve presents the ratio of captured power produced by a device to the power available in the waves at that frequency. In an irregular sea, there is a different amount of power available at each of the frequency bins. WEC developers tune their devices to operate optimally within a certain frequency range. As a result, a device will not extract the same percentage of power from each frequency bin. An RCW curve is generated for each sea state to determine what percentage of the power in the waves is absorbed (or radiated). The structure and procedure to generate an RCW curve is universal but the contents of the RCW Matrix depend on the input data (ie.

incident power, radiated power or power absorbed). For the purposes of demonstration, the remainder of this section describes the generation of an RCW curve for the power incident to a device.

First, Section 3.7.1.1 describes how the incident power in the waves at each frequency is determined, which is the denominator for the RCW presented in Eq. (14). Second, Section 3.7.1.2 describes how the power incident to the device is transformed from the time domain into the frequency domain, providing the numerator term in Eq. (14). Finally, Section 3.7.1.3 will conclude the section by demonstrating how the two frequency representations of power are used to determine the RCW curve for a sea state.

3.7.1.1 Wave Power in the Frequency Domain

Each time domain simulation is forced with individual sinusoidal waves with varying amplitudes, frequencies and directions to represent an incident wave spectrum which are converted into energy fluxes used as the denominator term in Eq. (14).

The wave amplitude associated with each frequency bin in the wave spectrum is converted to a variance. Variance associated with waves of different directions but falling within the same frequency bin were summed ultimately leaving the wave spectrum dependant only on frequency. The group velocity associated with the mean frequency of each frequency bin changes according to the depth across which a wave propagates and the dispersion relation [107]. Group velocity in intermediate water depth is defined as:

$$c_g = \frac{L}{2T}\left[1 + \frac{4\pi d}{L\sinh\left(\frac{4\pi d}{L}\right)}\right] \tag{33}$$

where L is the wave length, T is the wave period, d is the depth of water. The wave energy transport associated with each frequency bin is calculated using the discretized form of Eq. (11). The reader should note that all directional components of the incident wave spectrum are used to calculate the power incident to the device, while in *obstacle case five* only the orthogonal components of the energy flux were used to calculate the power in the waves.

3.7.1.2 Representation of Device Power in the Frequency Domain

A generic approach to determining the frequency dependent device power in a given sea state is presented. The device power can be either: the power absorbed by the device,

or a combination of the power incident to and radiated from the device depending on the input file the user wishes to generate. The following section will use the power transfer due to the wave excitation force as a case study to demonstrate how a force and velocity time series can be reconstructed into a frequency domain representation of power. Power is a product of an instantaneous force and velocity which are both readily available from the time domain simulation results generated in Section 1.5. The incident force exerted across each panel in a device's mesh is recorded for each time step and DOF over the course of the simulation. Velocity is similarly recorded for each body in the device and each DOF. The first 200 seconds of each times series is removed to eliminate start-up transients. The left hand side of Figure 17 presents the incident loading time series for the OWC body in heave. The right hand side of Figure 17 presents the velocity time series for the OWC body in heave.

Second, a Fast Fourier Transform (FFT) is conducted for the force and velocity time series data. The number of samples in the FFT is equivalent to the number of time steps in the signal. A high sample number was employed in order to resolve high frequency oscillations, ensuring the original signal variance is conserved. The FFT decomposes the time series signal into regular sinusoids. The FFT assigns an amplitude and phase to each frequency present in the time series signal. The amplitude spectrum corresponding to a device's incident loading in heave is presented on the left hand side of Figure 27 while the spectrum associated with the device's velocity in heave is presented on the right.

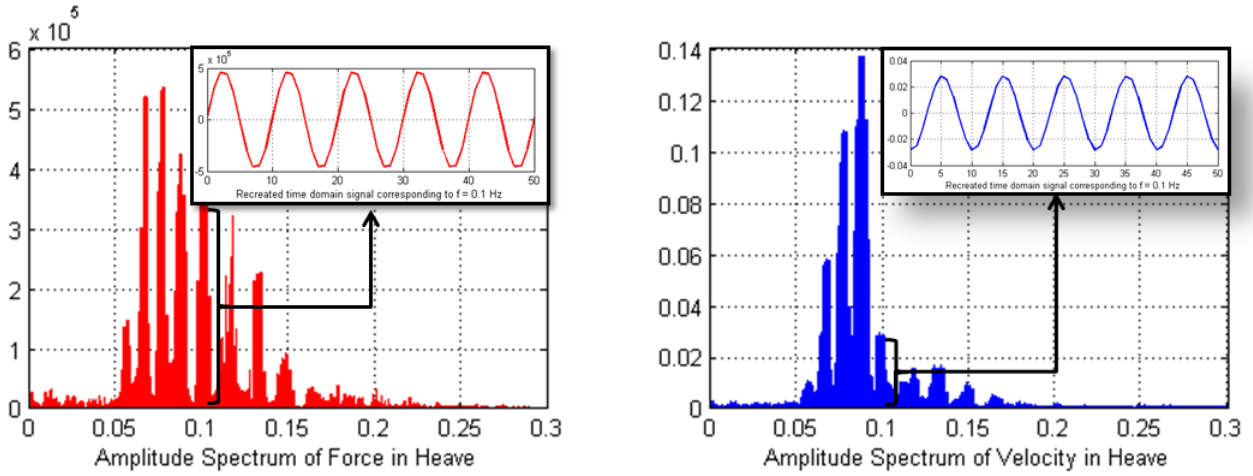

Figure 27: Force and Velocity Amplitude Spectrums for a single DOF in a sea state of H_s = 1.75 m and T_p=11.1 s.

The inset in the left and right hand side of Figure 27 show the sinusoidal wave associated with each of the frequency bins in the amplitude spectrum which have been recreated for each frequency bin in the spectrum. The water surface elevation is calculated using the non-directional form of Eq. (1):

$$\eta_i = A_i \cos(\omega_i t + \phi_i) \tag{34}$$

A power signal is generated by taking the product of the time series force and velocity signals presented both in Figure 28 and in each of Figure 27's insets. The mean value of this power signal corresponds to the power absorbed by the device at that frequency, as depicted in Figure 29.

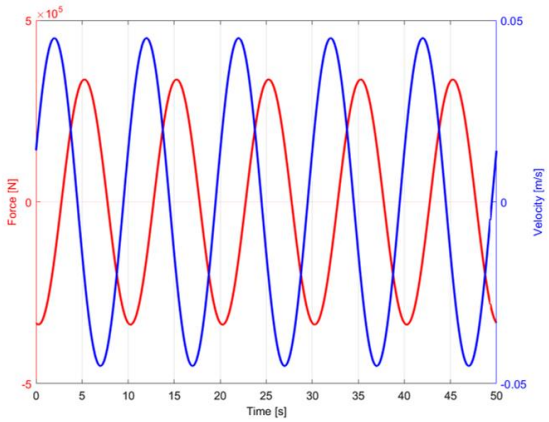

Figure 28: Force and velocity time series signal associated with a frequency of 0.1 Hz for a body in heave

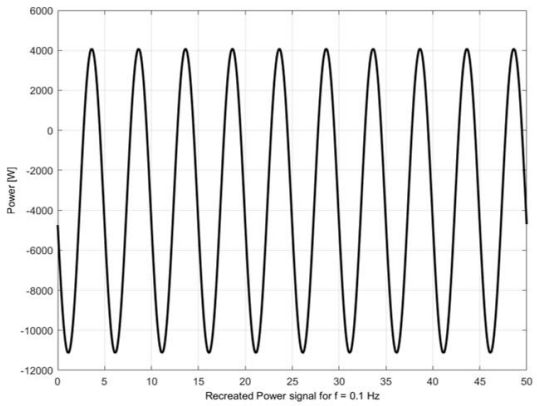

Figure 29: Power time series signal generated as a product of the force and velocity time series signals in Figure 28

It should be noted that after performing an FFT, the number of frequency bins produced by the transformation is equivalent to the number of samples in the input time series. As a result, the number of frequencies associated with the device's incident power spectrum is greater than that of the wave power (since SWAN works with a user specified number of frequencies, which in this study is 40). In order to generate an RCW curve, the incident power spectrum must be rebinned to correspond to the same frequency bins propagated through the ProteusDS simulation domain.

In order to rebin the signal, each of the incident spectrum frequency bins is assigned and grouped into a wave power frequency bin. Each grouped bin is worked with individually. The sinusoidal power signals associated with each of the frequencies within

the grouped bin are summed to generate a cumulative power signal. The grouping of bins and summation of signals for the power signal data is pictorially represented in Figure 30.

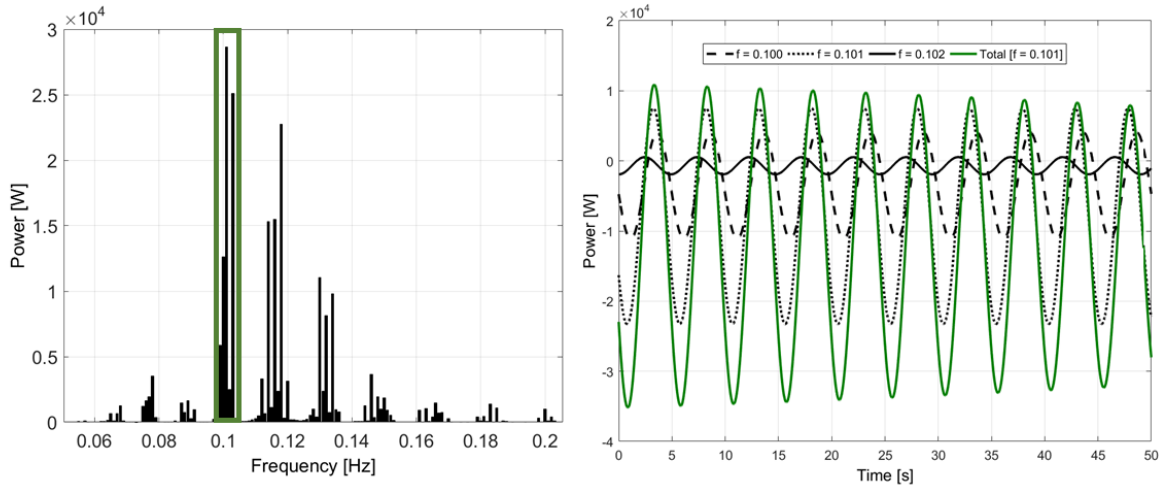

Figure 30: Summation of power signals to rebin into the same frequency bins as used in the incident wave spectrum.

The mean of this cumulative power signal is assigned to the grouped frequency bin. The methodology outlined above was conducted for a single incident loading force on the OWC's hull in heave. Section 3.7.1.3 describes how the rebinned frequency domain power signal is used to generate an RCW curve.

3.7.1.3 RCW Matrix Generation

An RCW curve is the ratio of the frequency resolved device power, for which the procedure was described in Section 3.7.1.2 and the frequency resolved wave power found in Section 3.7.1.1. In order to account for all the power incident to the device, the procedure outlined in Section 3.7.1.2 must be repeated for each force incident on the device in each DOF. The total power incident to the device is a summation of power contributions previously noted in Equation 15. Each of these power contributions is related to a force and velocity time series found in the time domain simulations. The time series data is processed using the methodology presented in Section 3.7.1.2 and summed. Once the total power incident to the device is found, a ratio of the wave power spectrum and the incident power spectrum is taken. The two power spectrums are presented on the left hand side of Figure 31 with the resulting RCW curve on the right.

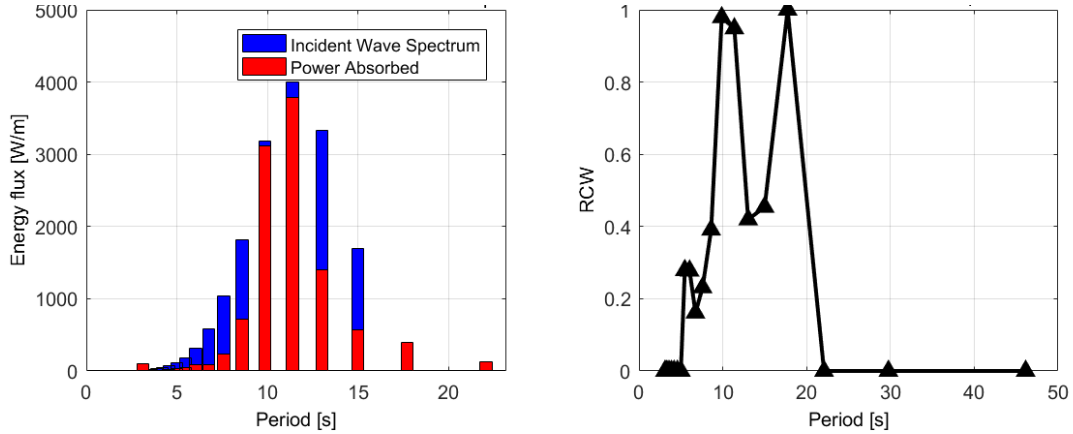

Figure 31: Power in a Hs = 1.75m and Tp = 11.1s sea state and power absorbed by the device overlayed on the left. RCW curve associated with this sea state on the right.

The RCW curve associated with a particular sea state is placed in the third dimension of the RCW matrix where the first two dimensions are chosen based on the index of the H_s and T_p characterizing the sea state.

Theoretically, either side of the power balance in Eq. (26) can be used to generate an RCW curve, as was previously described in Section 3.5.7. For the purposes of this work, the RCW curve for each sea state was generated from an average of the two curves. The approach presented in Section 3.7 allows the user to spectrally resolve the power transfer between the device and the surrounding fluid for each particular power contribution. However, by applying an FFT, we assume that the force assigned to a particular frequency bin has been generated as a result of the wave power in the same bin. Generating an RCW curve involves summing the spectrally resolved power of the contributions outlined in Figure 23. The power contained in each frequency bin can be either positive or negative depending on whether the power in this bin is leaving or entering the device. Even though this method can establish a general representation of the device's dynamics, the transfer of power from one frequency bin to the next due to nonlinear forcings cannot be resolved. As such, there are instances in which the power in certain frequency bins exceeds the energy flux associated with the incident wave spectrum, described in further detail in Section 5.1. It is beyond the scope of this thesis to determine the origins of this excess energy, but in an effort to make the proposed method tractable, power in excess of the incident wave spectrum was redistributed to neighbouring bins. This procedure was applied for two reasons. First, at these

frequencies, it is implied that the device is extracting more power than is physically available in the incident wave spectrum, violating the conservation of energy within SWAN. Second, in order to make *obstacle case five* and *six* consistent, the power absorbed by the device in each obstacle case would need to be the same (ie. the sum of each spectral power component must be the same as the total power absorbed by the device in a particular sea state in obstacle case five).

A post-processing step was employed where the RCW curve for each sea state was analyzed. If at a particular frequency the power exceeded that of the incident wave spectrum, the excess power at that frequency would be distributed to the frequency bins to the left and right. In cases where the neighbouring bins are already saturated, power would be shifted to the next neighbouring bin. The nearest bins would always be saturated first, followed by the successive neighbouring bins. Three illustrative cases for rebinning excess power in a particular frequency bin are presented in Figure 32 to Figure 34. First, if there is excess power absorbed by the device, depicted by the red cross-hatched area in Bin 13, and there is wave energy available in the two neighbouring bins (12 and 14), the excess power absorbed will be evenly distributed across the two bins.

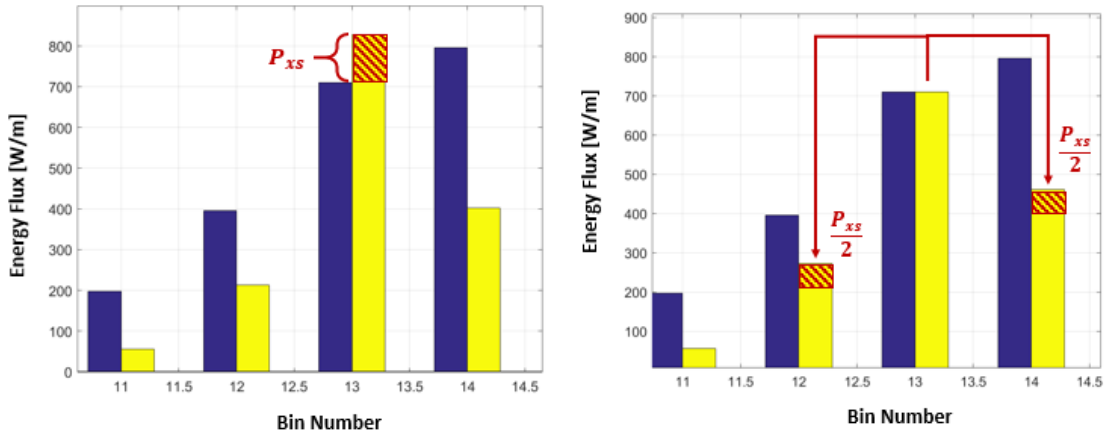

Figure 32: Redistribution of energy flux when there is enough available wave energy transport available in both neighbouring bins. The blue bins are the wave energy transport in the incident sea. The yellow bins correspond to the relative capture width at that period.

In the second case presented in Figure 33, if there is power absorbed by the device in excess of the available wave energy (Bin 16), and one of the neighbouring bins is already saturated (Bin 17), the excess power is transferred into Bin 15. The final case in which energy is rebinned is presented in Figure 34. The excess power absorbed by the device in

Bin 15 is first shifted into its two immediately neighbouring bins (Bin 14 and 16). After the neighbouring bins are saturated, the rebinning algorithm moves into the next neighbouring bin, Bin 13.

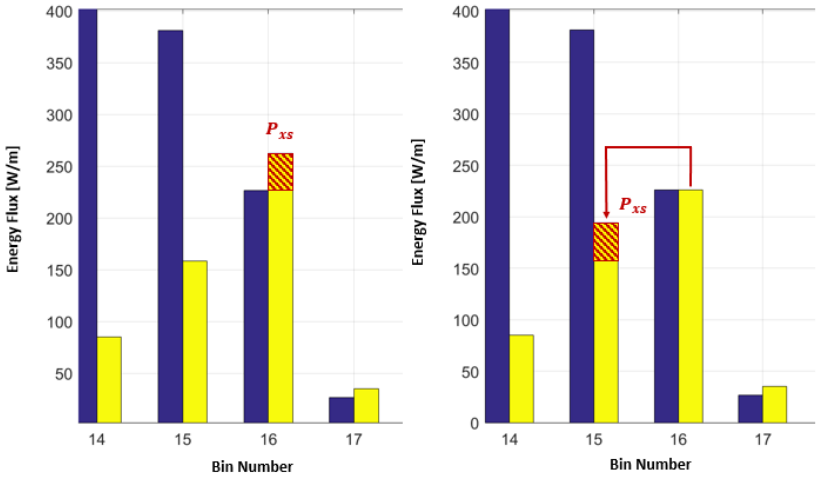

Figure 33: Redistribution of energy flux when there is only enough available wave energy transport in one of the two neighbouring bins. The blue bins are the wave energy transport in the incident sea. The yellow bins correspond to the relative capture width at that period.

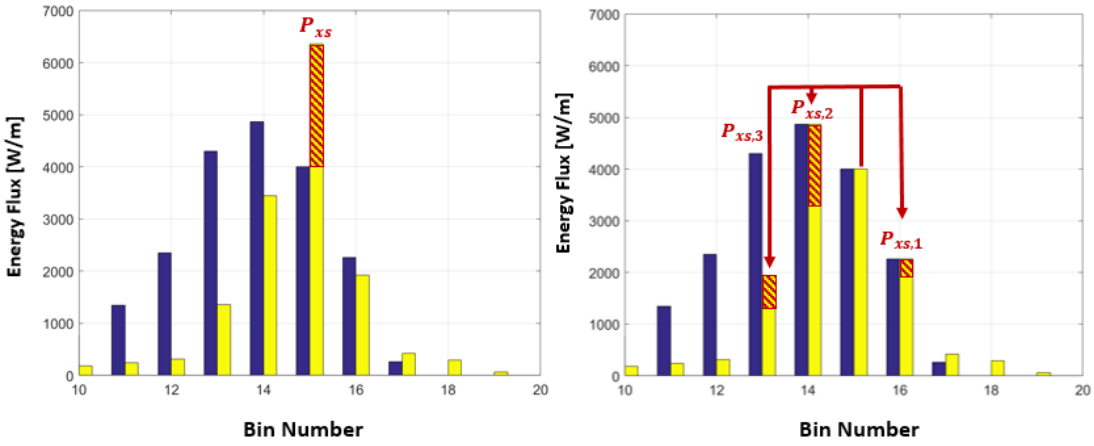

Figure 34: Redistribution of power when the two neighbouring bins are saturated. The blue bins are the wave energy transport in the incident sea. The yellow bins correspond to the relative capture width at the same period.

3.8 Novel Obstacle Case Summary

The representation of a dynamic, wave-generating device within a wave modelling software can take many forms. SNL has proposed using the obstacle command within SWAN to represent a WEC. The work presented in this thesis seeks to add a degree of higher fidelity to this representation and ultimately determine what the limitations to this representation are. The obstacle command in SWAN was originally designed to represent breakwaters as straight line barriers that could be positioned along gridlines within the modeled domain. SNL refers to this command as *obstacle case zero.* A constant percentage of the incident wave energy is extracted across all sea states and frequency bins.

The WEC representations developed by SNL seek to characterize a device based on information available to utilities and regulators from device developers. In practise, device developers are most concerned with power capture performance and thus report captured power metrics. The derivation of a transmission coefficient from these metrics alone assumes any effect the WEC has on the surrounding sea state is represented solely by the power captured by the device – energy losses and radiated energy are unaccounted for. To better represent the device's impact on the surrounding fluid domain, the author has developed WEC representations that account for both the device's captured power as well as the device's intercepted power.

Obstacle case five bilinearly interpolates a transmission coefficient from an intercepted power matrix, uniformly reducing the variance in each frequency bin of the incident spectrum. The intercepted power is used to calculate the device's impact on the surrounding fluid domain while the captured power is used to determine the power produced by the device.

Obstacle case six applies a sea state and frequency dependent transmission coefficient to the incident variance spectrum. This transmission coefficient is calculated from the RCW Matrix. As in *obstacle case five,* the intercepted power is used to calculate the device's impact on the surrounding fluid domain while the captured power is used to determine the power produced by the device. *Obstacle case six* is a higher fidelity representation of a wave energy converter however without further validation it is

difficult to determine which of the two novel obstacle cases is more accurate. Each WEC representation presented in this Chapter is summarized in Table 4.

The conservation of intercepted power between *obstacle cases five* and *six* is analyzed. The power contributions of the P_{INC}, $P_{RAD,}$ and P_{ABS} terms presented in Eqs.(15) through **(29)** are conserved to a great degree between *obstacle cases five* and *six*. On average, the mean root square error of the incident power and the radiated power, presented in Figure 35 and Figure 36 is 0.34% and 1.14% respectively. The radiated power is prone to more error as the force and velocity contributions come from two separate models (a hydrodynamic ProteusDS model and a thermodynamic Simulink model) which were modeled at different time resolutions. In addition, there were more radiation force contributions resulting in a greater summative error.

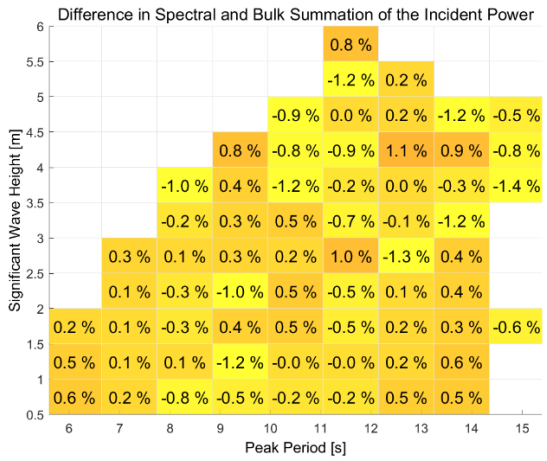

Figure 35: Percentage difference between the bulk incident power and the sum of the spectrally resolved incident power in each sea state

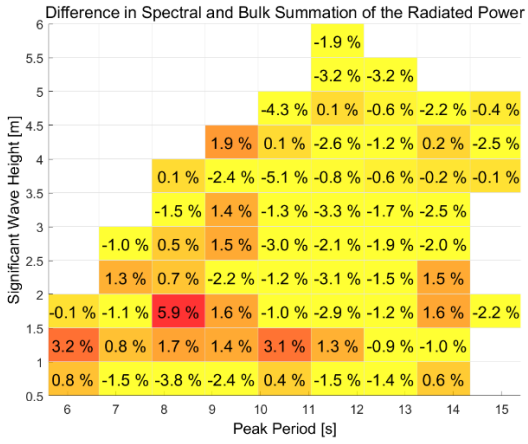

Figure 36: Percentage difference between the bulk radiated power and the sum of the spectrally resolved radiated power in each sea state

The root mean squared error, averaged for each modelled sea state, between the bulk power employed in *obstacle case five* and the summation of the spectrally resolved power terms from *obstacle six* is 0.13% and 2.04% for P_{ABS} and P_{INC}-P_{RAD} respectively. The error between the two is presented for each sea state in Figure 37 and Figure 38. In general, the spectrally resolved representation of power sums to a lower value as a result of minor losses in power due to FFT windowing and potential leakages within bins. The difference in the LHS of the power balance (P_{INC}-P_{RAD}), is generally greater than that of the right because it is composed of more power contributions. Again, the greatest error

can be observed in lower energy sea states with both low significant wave heights and peak periods.

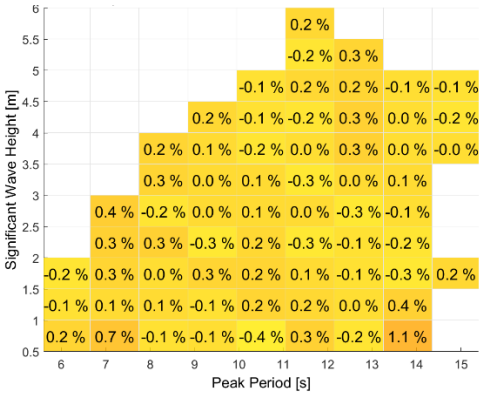

Figure 37: Difference in Spectral and Bulk Summation of the P_{ABS} term of the Power Balance for each sea state modelled in the time domain

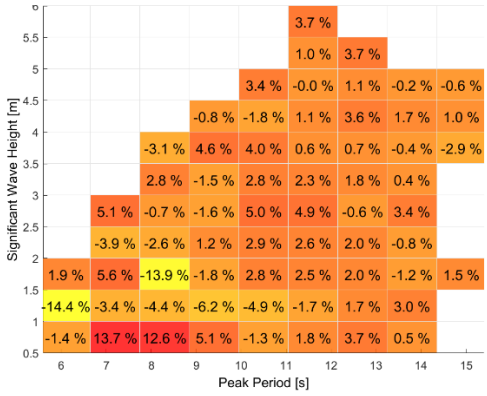

Figure 38: Difference in Spectral and Bulk Summation of the (P_{INC}-P_{RAD}) term of the Power Balance for each sea state modelled in the time domain

A more detailed analysis of the SWAN model's sensitivity to *obstacle cases one*, *five* and *six* is presented in Chapter 4. The reader is reminded the aim of this thesis is twofold. First, the feasibility of representing a WEC in a wave modelling software using SWAN's obstacle representation is investigated. Second, more detailed device representations are proposed and a sensitivity analysis is conducted to quantify the differences observed in far field impact and annual energy production when these new representations are used. Chapter 3 outlines a roadmap in which additional layers of complexity are added to each WEC representation. *Obstacle case five* first introduces the idea of having a device represented not only by its captured power, but also by its intercepted power. WECs operate more efficiently in certain frequency ranges as a result of their PTO tuning. To better characterize a WEC's operation, frequency dependent energy extraction must also be included in a WEC's representation which lead to the development of *obstacle case six*.

Table 4: Obstacle case summary

Obstacle	User Input	Transmission	Dependencies
0	Ratio	Constant	None.
1	Power Matrix	Constant	H_s, T_p
2	RCW Curve	Constant	T
3	Power Matrix	Frequency Dependent	H_s, T_p
4	RCW Curve	Frequency Dependent	T
5.1	Power Matrix Power Absorbed Matrix	Constant	H_s, T_p
5.2	Power Matrix Incident Power Matrix Radiation Matrix	Constant	H_s, T_p
6	Power Matrix Relative Capture Width Matrix	Frequency Dependent	H_s, T_p, T

In total, eight representations have been proposed in Chapter 3. Certain representations will not be analyzed any further due to a lack of input information or challenges in implementation. Of the newly proposed device representations (*obstacle cases five* and *six*), both representations are only investigated as sinks due to practical limitations when investigating the performance of the reference WEC. In *obstacle case five* assuming an equal distribution of radiation in front of and in the lee of the reference WEC, the WEC removes more power than is present in the incident sea for the reference device. *Obstacle case six* could also not be employed as a source and a sink because it would suffer from cases where at particular frequencies the transmission coefficient would exceed one. This problem stems from the device's representation and the creative choice of using the device's width to normalize the power produced by the device, which will also be discussed in Section 5.1.1. This issue is further discussed in Chapter 5. By representing the device solely as a sink, the power radiated by the device is present only in the lee thus reducing the net power absorbed by the device.

Obstacle case 6 is investigated also as a sink allowing the user to compare a constant transmission representation (*obstacle case 5*) to a frequency dependent one. The WEC representations investigated in Chapter 4 have been carefully chosen for their capacity to demonstrate the defining characteristics of each representation.

Chapter 4

Results

Two novel representations of a WEC within a spectral action density model were proposed in Sections 3.6 and 3.7. Both representations use time series data from high fidelity time domain simulations to more accurately depict the device's hydrodynamic behaviour at sea. The author has chosen to analyze the sensitivity of the captured power by a device and the far field impact of a device when characterized with the new obstacle cases. It is of the highest importance to determine whether SNL-SWAN is at all sensitive to the additional layers of fidelity. *Obstacle cases five* and *six* require more preprocessing than cases zero through four adding to the computational expense of characterizing a device. This chapter establishes the impact of representing a device with additional pre-processed data.

In this chapter, the power production and far field impact of an array is compared between obstacle cases one, five and two instances of obstacle case six. Results of the first simulation set are presented in Section 4.1.2 in which a single device is observed in a flat bottom domain followed by an analysis of five WECs in series. Section 4.2.3 describes the results collected from a field study at Amphitrite Bank in which the new

WEC representations are applied to determine the array's far field impact at a real location and the impact of each representation on determining an array's annual energy production.

4.1 Flat Bathymetry Domain Simulations

Rather than conducting a validation of the newly developed source code, a sensitivity analysis is conducted. The previously implemented *obstacle case one* is compared to the novel *obstacle cases five* and *six*. *Obstacle cases two*, *three* and *four* were discounted from further analysis as the computational expense for generating the input files surpassed any additional fidelity that could be gained from these representations, as discussed in Section 3.8. An initial sensitivity analysis is conducted within a flat bottom domain with an incident wave condition corresponding to the most commonly occurring sea state at Amphitrite Bank (Hs=1.75 m, Tp =11.1 s), as described in further detail in Section 4.1.1.

4.1.1 Flat Bathymetry Domain Description

In the first case studies, a flat bottom domain was employed in order to eliminate bias that may result from a changing topography. By stripping away layers of complexity such as: varying bathymetry and non-stationary boundary conditions, and neglecting non-linear forcings, one can more clearly discern the differences imposed on the surrounding wave field by each WEC representation. Any changes in the surrounding wave field or in the power produced by the device can confidently be attributed to the WEC representation opposed to other external factors. Within the flat bathymetry tests, two device configurations were run in SNL-SWAN to demonstrate the effectiveness of obstacle cases five and six. The first configuration examines the impact a single device has on the surrounding wave climate. The second configuration is comprised of five devices in series. This configuration is analyzed to both quantify the devices' environmental footprint and to investigate the impact a device's shadow has on a subsequent device's power production.

Both configurations were run in a Cartesian domain with a grid resolution of twenty five meters in the x and y directions and a uniform 50 meter depth. The most commonly occurring sea state at Amphitrite Bank, as presented in Section 1.6 is investigated for this case study. An idealized Pierson Moskowitz spectrum characterized with an H_s, T_p and a $\cos^2$ directional spreading was applied across the model domain in each of the test cases, representing spectral shapes similar to the ones observed off the West Coast of Vancouver Island [49]. Source terms typically used to represent non-linear phenomena in SWAN such as wind growth, triad and quadruplet wave interactions were disabled for this simulation to better demonstrate the impact the device has on the surrounding sea.

Configuration 1

In the first configuration, a device was represented with a line extending from (1215 m, 1215 m) to (1215 m, 1242 m), as depicted in Figure 39. This device was represented using obstacle cases one, five, and six. Obstacle cases five and six were implemented both as sinks as well as sources and sinks in a 2500 metre by 2500 metre computational domain with a spatial resolution of 25 metres and a directional resolution of five degrees.

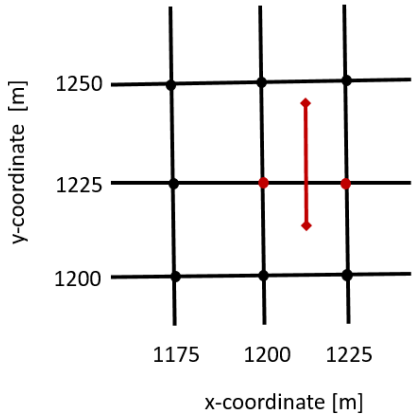

Figure 39: Device is represented as a line between two points in the computational domain (1215 m, 1215 m) and (1215 m, 1242 m) in SNL-SWAN.

Configuration 2

The second configuration consisted of five devices placed one behind the other. A 270 metre separation distance was chosen between each of the five devices. This distance would provide maintenance vessels with sufficient space for operation and sufficient distance for each device's watch circle [108]. Secondly, Stratigaki has recommended

employing a separating distance of ten times the device's width to reduce destructive device interaction [62]. Similarly to the first configuration, the computational domain extended 2500 metres in both the x and y direction with a spatial resolution of 25 metres and a directional resolution of five degrees. An inset of the computational domain and the five devices are presented in Figure 40 and node points defining the 5 WEC devices are given in Table 5.

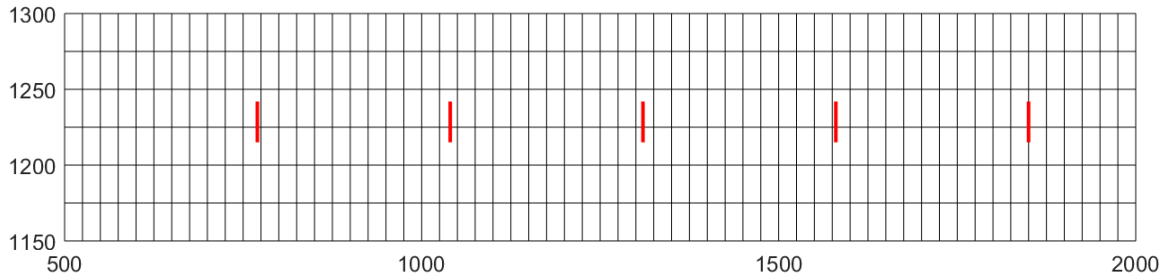

Figure 40: Device representation within an inset of the flat bathymetry computational domain.

Table 5: Coordinates of each of the devices employed in Configuration 2 of the flat bathymetry case study

Device number	Coordinate 1	Coordinate 2
1	[770 m, 1215 m]	[770 m, 1242 m]
2	[1040 m, 1215 m]	[1040 m, 1242 m]
3	[1310 m, 1215 m]	[1310 m, 1242 m]
4	[1580 m, 1215 m]	[1580 m, 1242 m]
5	[1850 m, 1215 m]	[1850 m, 1242 m]

The reader is warned that the H_s fields in Figure 41 and Figure 44 may appear pixelated, however more finely resolved grids spatial grids may result in an artificial banding pattern in the H_s in the lee of a device. This banding is commonly referred to as the 'garden sprinkler' effect which emerges when the ratio of the directional and spatial resolution is too low. Booji and Holthujisen suggest the width of the spectral bands in frequency and direction should fulfill the following condition ($\Delta\theta < \frac{1}{N}$) where N is the distance across the computational domain expressed in number of mesh elements [84]. For the test cases used, this would imply a directional resolution of 0.01 degrees.

Unfortunately this criterion is impractical for the discretization of highly resolved grids, leading to immense computational times and memory allocation issues. The developers of SWAN have implemented correction terms to the energy balance equation in order to reduce these effects, however caution must be exercised by the modeller to ensure the directional bins are adequately resolved for each simulation. Previous sensitivity analyses suggest that with higher directional resolutions, these perturbations will be removed. The author chose to employ a directional resolution of five degrees to strike a balance between accuracy, the reduction of numerical defects such as the garden sprinkler effect and computational expense

4.1.2 Flat Bathymetry Domain Results

This section establishes the far field impact of a WEC and multiple WECs in series. The change in the surrounding wave field and the incident wave spectrum at different distances in the lee of the device are investigated. How these effects leads to changes in power production downstream of the WEC are also examined.

Impact on the Surrounding Wave Field

Each of the *obstacle case one, five* and *six* representations impacted the surrounding wave field to some extent. A two-dimensional plan view of the variation in H_s in the field surrounding the single WEC is presented in Figure 41. Since the energy transport in the wave field is proportional to H_s^2, the significant wave height measure is a good metric for gauging the magnitude of the WEC's far field impacts. In Figure 41, *obstacle cases five* and *six* attenuate H_s more than *obstacle case one* indicating that characterizing the device interaction with the surrounding wave field with intercepted power opposed to captured power has an input on the nearfield.

The attenuation to 90% of the incident significant wave height is analyzed in each of the obstacle cases. In *obstacle case one,* an H_s of 1.6 metres is observed five metres behind the device. In *obstacle case five,* the 1.6 metre H_s contour is observed 90 metres while in *obstacle case six*, the H_s = 1.6 metre contour extends 70 metres behind the device.

With respect to H_s recovery, The H_s recovers to 1.72 metres 100 metres behind the device in *obstacle case one,* 330 metres behind the device in *obstacle case five* and 260

metres behind the device in *obstacle case six*. Of the two representations accounting for the device's intercepted power, *obstacle case six* has less of an impact on the significant wave height in the lee of the WEC device. *Obstacle case six* removes power from selected frequency bins in the wave spectrum. The incident power and radiated power are both represented as sinks. As such, the radiated power compensates for the power absorbed by the device since both quantities are only represented in a single direction due to directional limitations of this particular representation, and since only certain frequency bins are affected.

Even though *obstacle case five* and *six* remove the same amount of power from the system, there are differences in the H_s reduction in the lee of the device when these two representations are employed. The difference is attributed mostly to the different methods with which the power absorbed is calculated for these two representations. The transmission coefficient for *obstacle case six* is interpolated from an RCW matrix generated with the spectrum used in ProteusDS. The total energy flux was used as incident power opposed to the orthogonal projections of the directional power used in *obstacle case five*. Secondly, the spectrum within ProteusDS had 20 frequency bins and seven directional bins. When SNL-SWAN calculates the transmission coefficient it must linearly interpolate from a set of half the bins Depending on how peaked the RCW curve is, this interpolation can cause underpredictions in power as well.

The H_s contours in each of the obstacle cases are roughly circular, increasing in area as greater decreases in H_s are observed directly behind the device. The circular pattern can be attributed to the fact that the transmission coefficients are insensitive to direction. These circular patterns are likely to change if directionally dependent transmission coefficients are implemented in future WEC representations in SNL-SWAN.

Additionally, the transmission coefficient in *obstacle case five* was determined from the perpendicular projection of the incident spectrum onto the device's inlet. If the waves were to come from an oblique incidence angle, the magnitude of energy perpendicular to the device would decrease, reducing the denominator in Eq. (14), increasing the transmission coefficient.

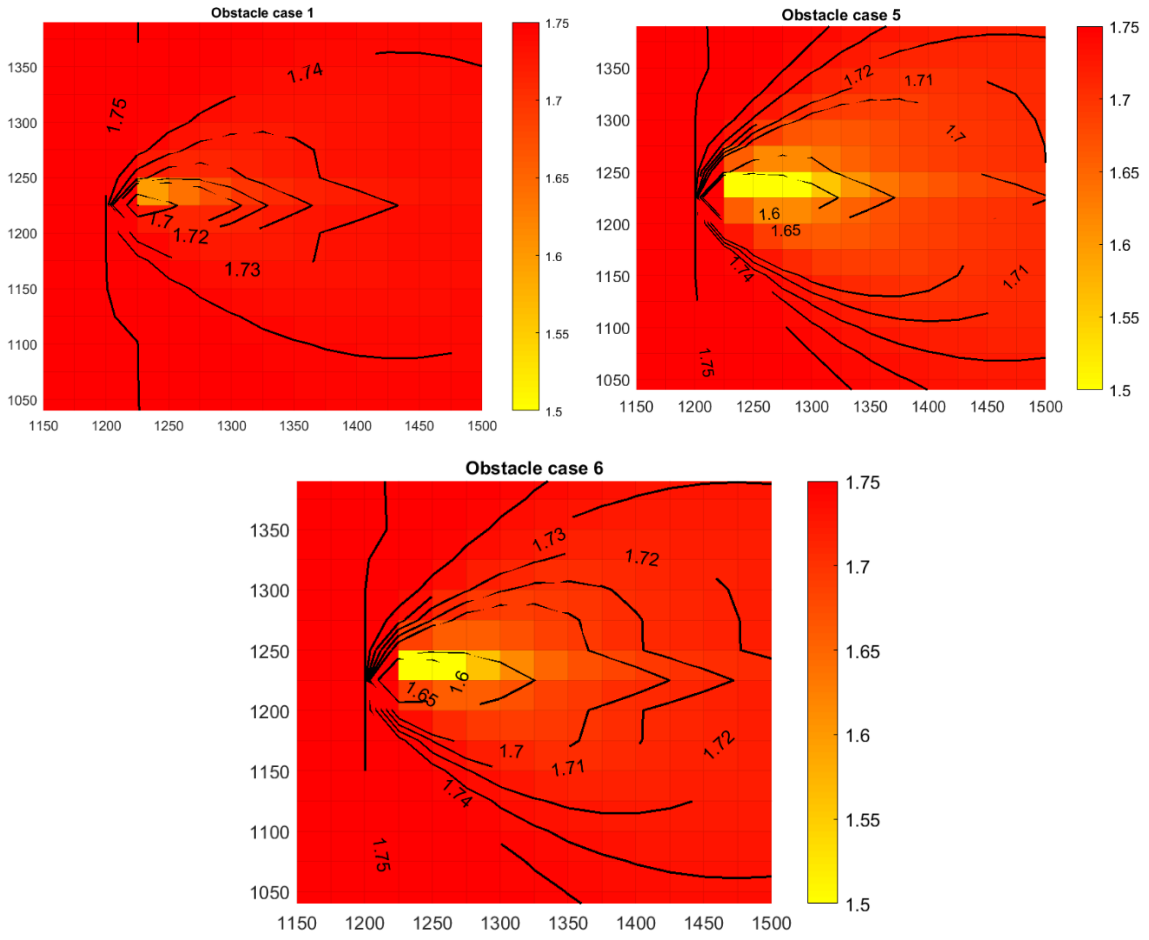

Figure 41: Significant wave height comparison demonstrating a device's impact on the surrounding wave field when represented with different obstacle cases in the most commonly occuring sea state off of Amphitrite Bank (H_s=1.75 m, T_p = 11.1 s)

The difference between these representations becomes even more apparent when the wave spectra in the lee of the device are studied. Figure 42 presents the omni-directional variance spectra interpolated at five metres (top left), 25 metres (top right), 100 metres (bottom left) and 200 metres (bottom right) behind the device. This figure demonstrates both how the variance spectrum recovers as it moves further away from the device as well as how the device removes energy from the variance spectrum depending on its representation. The wave spectrum incident to the device is presented in black for reference.

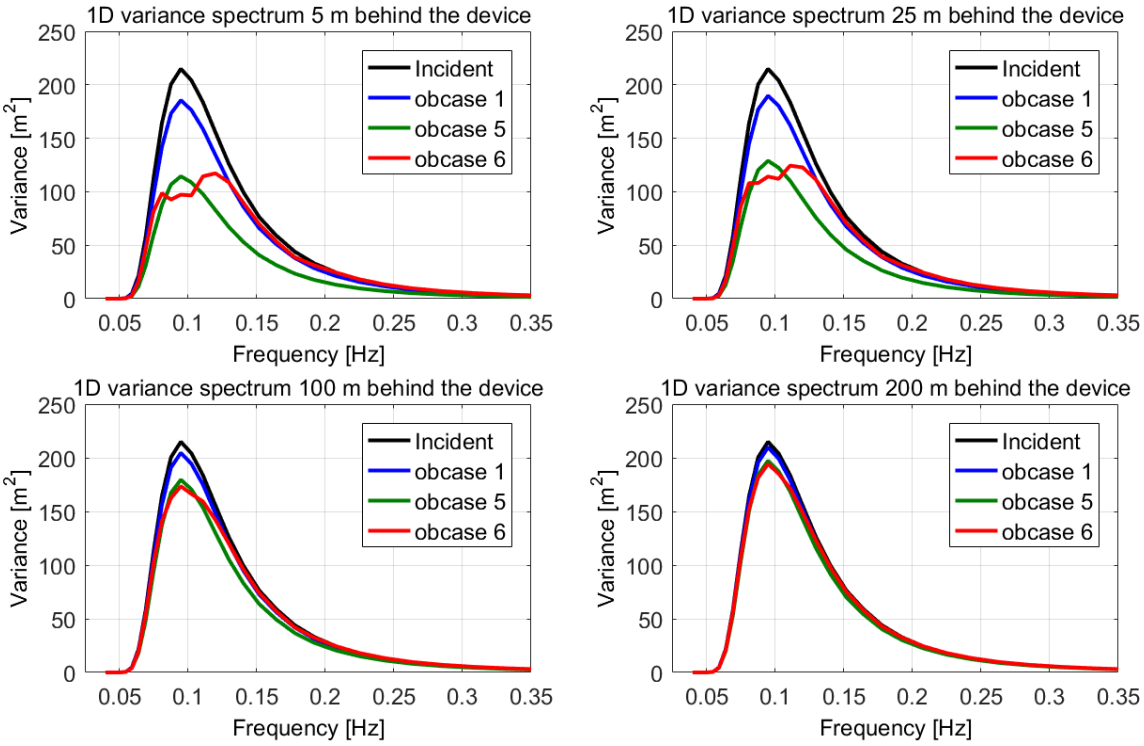

Figure 42: Comparison of non-directional variance density spectra at various distances behind the WEC when the WEC is represented with obstacle cases one, five and six.

The greatest decrease in variance can be observed directly in the lee of the device, as can be seen in the top left corner of Figure 42. The variance spectra modified by *obstacle cases one* and *five* are scaled forms of the incident variance spectrum. The uniform decrease in the spectrum is expected given a frequency independent transmission coefficient is applied in both cases. The spectrum corresponding to *obstacle case six* has been non-uniformly decreased as a function of frequency as can be seen in the relative capture width curve presented for this sea state in Figure 31. *Obstacle case six* removes the most power at the spectrum's peak (0.09 Hz)as well as to the right of the peak (0.11 Hz), where the device operates most efficiently [20].

At a distance of 25 metres behind the device (top right), the variance density spectrum is seen to recover quickly. One may also observe that the variance density spectra affected by the frequency dependent representations of the device have shifted variance back into the peak frequencies resulting in a spectrum that more closely resembles the incident Pierson Moskowitz spectrum. The device representations that removed less

energy from the incident wave spectrum recover at a slower rate than those that removed more. As one moves further from the device, at 100 metres (bottom left), all spectra have assumed the same shape with differences in amplitude depending on the representation. Finally, at 200 metres away from the device (bottom right), the spectra have all nearly recovered to the same levels of variance, across all frequencies, as the inlet spectrum.

An additional analysis was conducted in which the non-directional variance density spectrum was analyzed for each WEC representation at different distances from the device as seen in Figure 43.

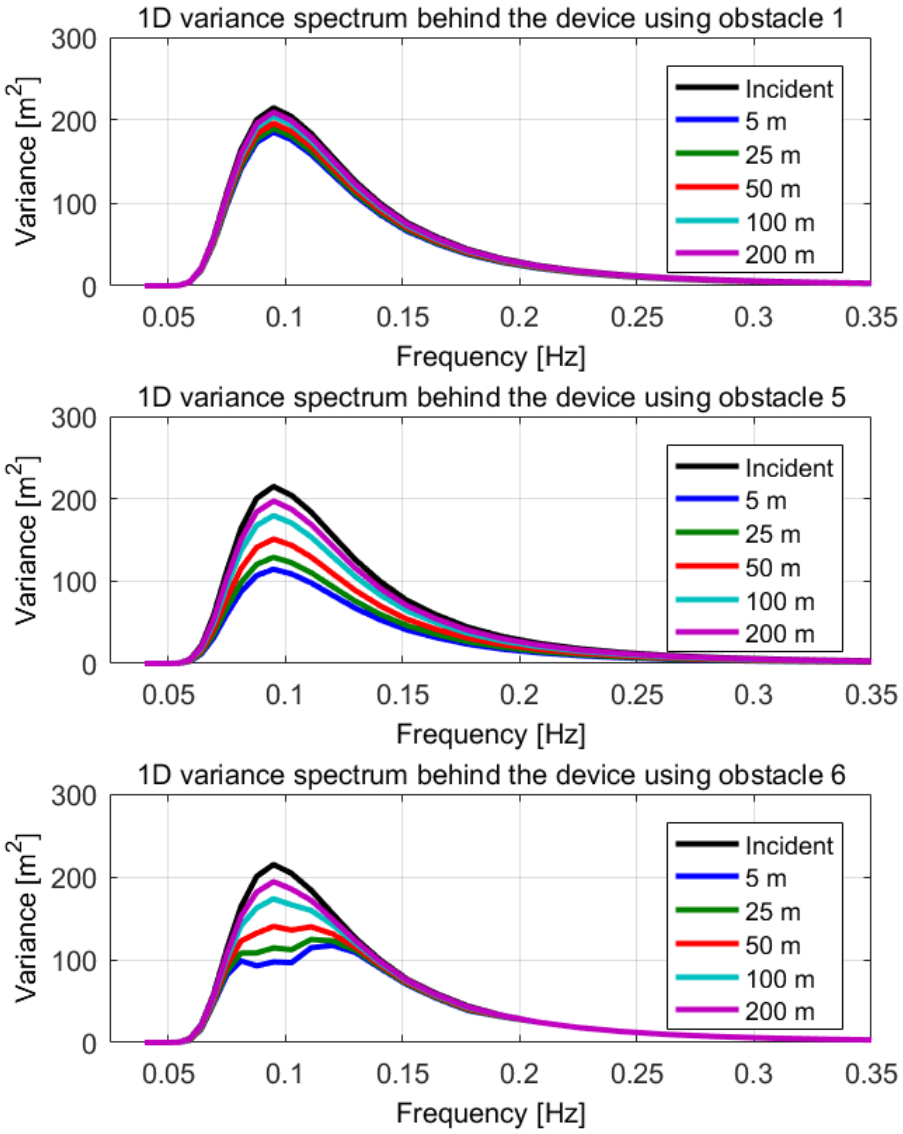

Figure 43: Evolution of variance density spectrum with increasing distance away from the WEC when the WEC is represented with different obstacle cases.

This view is intended to give a clear visualization of the recovery of the wave spectrum in the lee of the converter. In all device representations, the variance spectrum recovers as the variance spectrum propagates further from the device. This growth in variance can be attributed to energy transport diffracting around the obstacle and moving into areas of lower energy in the lee of the device. The frequency dependent energy extraction in *obstacle case six* is most prominently observed five metres behind the device. The spectrum assumes a shape similar to that of the incident spectrum 50 metres behind the device. As previously mentioned in the discussion of Figure 42, *obstacle case six* removes the most energy at the spectrum's peak as this is the frequency at which the device operates most efficiently.

Figure 44 presents a surface plot depicting the modification of H_s when five devices are placed in series at a spacing of ten device widths.

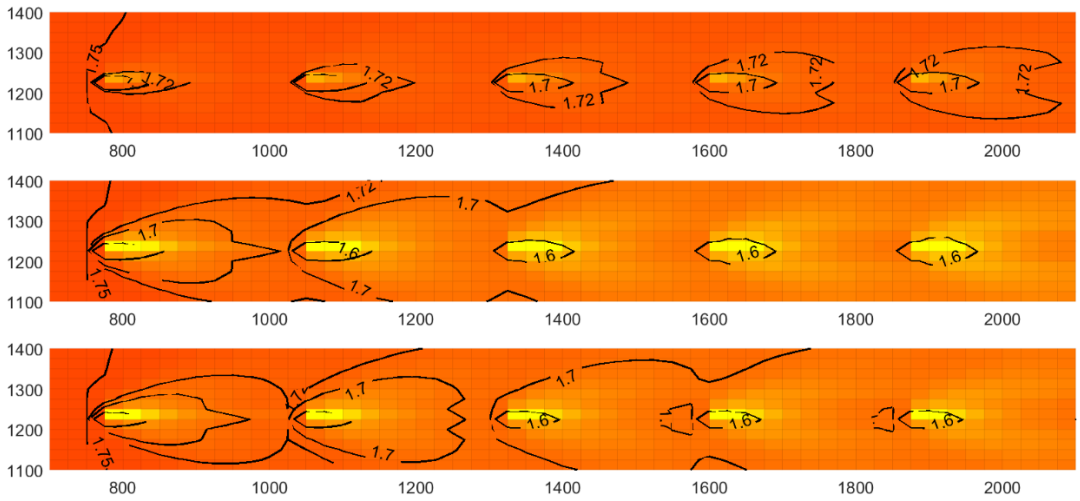

Figure 44: Hs contours surrounding a line of five devices spaced 10 device widths away from one another

The top plot of Figure 44 corresponding to the wave field around a device represented with *obstacle case one*. The middle and bottom plots show analogous results from when *obstacle cases five* and *six* are run. The first device maintains a narrow elliptical significant wave height contour, which grows in width after each subsequent device. In addition, one may observe a greater decreases in H_s closer to the device's node points opposed to directly behind the device. The decrease in significant wave height near the obstacle's node points can be attributed to diffraction around the device. As energy

diffracts in from both sides of the device it concentrates directly in the lee of the device as a result of the incident spectrum's directional spread. A directional spread of two was run as this corresponds to the directional spread employed in the time domain simulations. The same pattern is observed in each obstacle case, with differences in the magnitude and spatial extent of the H_s attenuation.

The recovery of H_s directly in the lee of five devices is presented in Figure 45. All device representations result in a similar pattern in H_s profile. *Obstacle case five* consistently reduces the significant wave height more than *obstacle case six*. At first the difference is merely 0.02 metres between the two, and by the fifth device the difference in significant wave height reduction increases to 0.04 metres. The incident H_s at each device is presented in Table 6. Small differences in H_s are observed at the last three devices. As the incident H_s decreases, a greater transmission coefficient is employed for this particular sea state, thus reducing the power absorbed at each device.

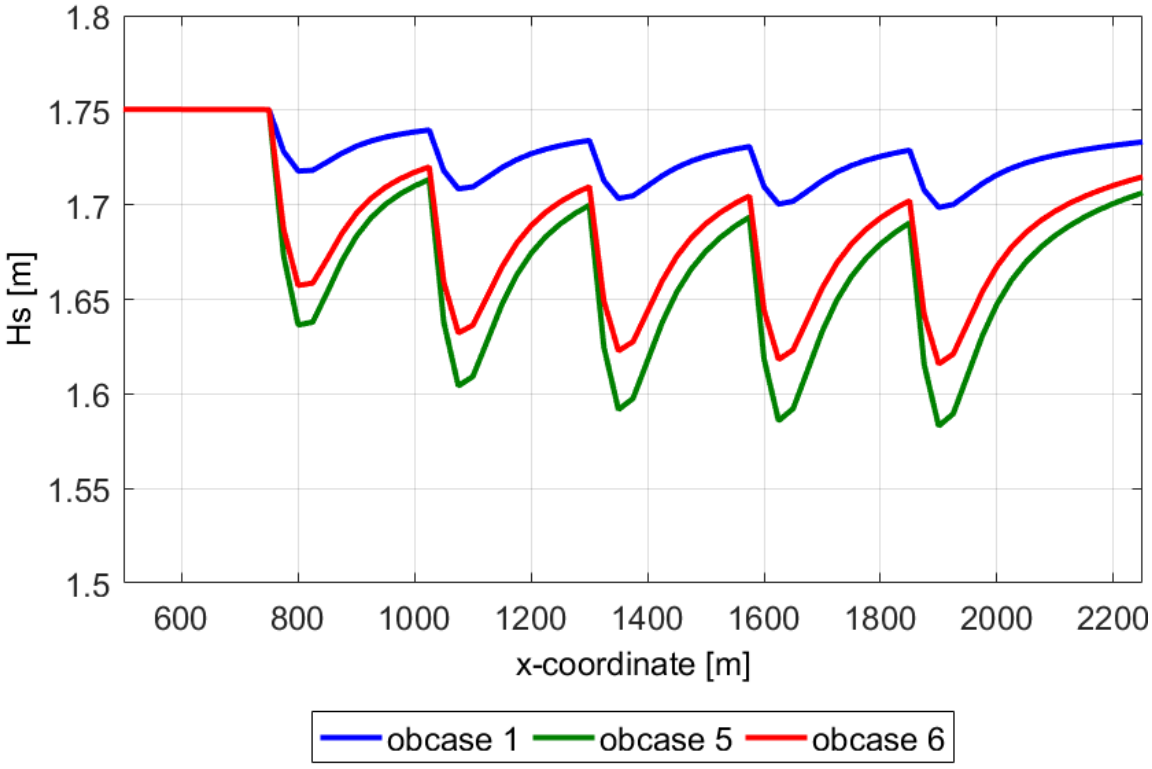

Figure 45: Comparison of the profile view of the H_s and its recovery in the lee of five devices when the devices are represented with different obstacle cases

Table 6: H_s incident to each device, when devices are represented with obstacle cases one, five and six.

Device number	Obstacle Case One	Obstacle Case Five	Obstacle Case Six
1	1.750	1.750	1.750
2	1.739	1.713	1.720
3	1.734	1.700	1.710
4	1.731	1.694	1.705
5	1.729	1.690	1.702

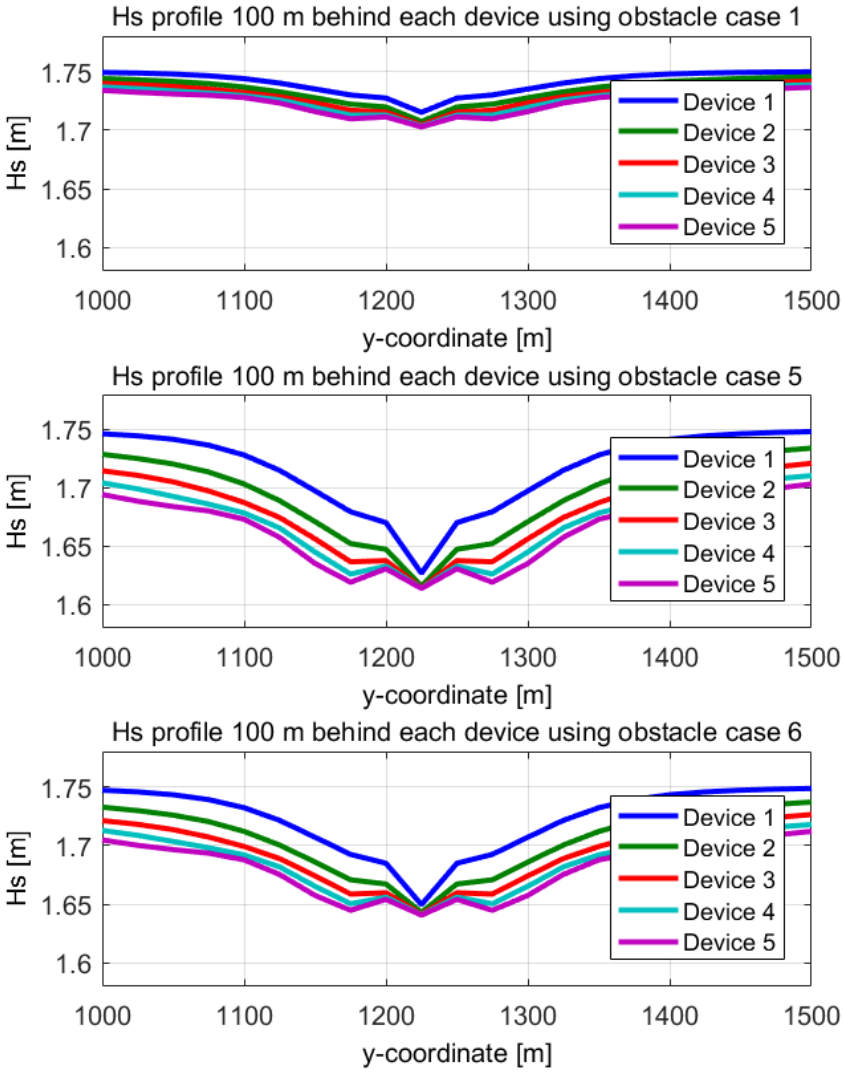

Figure 46: Cross sections of the H_s profile 100 metres behind each device when using different obstacle case representations.

As presented in Table 6, the wave height incident to the last device is decreased by 1.2% when *obstacle case one* is employed, 3.4% when *obstacle case five* is employed and 2.7% *obstacle case six* is employed

Finally, a cross-sectional view of the H_s 100 metres behind each of the five devices is presented in Figure 44. In each of the section views, there is a sharp jump between 1200 metres and 1225 metres, as well as between 1225 and 1250 metres. This jump is largely a result of interpolation and would not be present if a higher spatial resolution was employed. Due to the garden sprinkler effect discussed in Section 4.1.1, a higher spatial resolution would also create artificial oscillations in H_s across the H_s profile. *Obstacle cases five* and *six* recover at similar rates behind each device along the cross sections. The greatest difference between the first device's significant wave height profile and the last device's significant wave height profile is seen when employing *obstacle case five*.

Impact on power production

The representation used for a WEC also impacts the power production of each device. Each device decreases the H_s in the device's lee, ultimately changing the incident conditions of the subsequent device until a steady state is reached in which the conditions no longer change for each device thereafter.

Given each representation modifies the surrounding wave field to a different degree, the power captured by a device from the incident wave field will also change with each representation. The power produced by each of the five devices in the second configuration is reported in Table 7 followed by the percentage decrease in captured power presented in Table 8. The percentage decrease is calculated by comparing each individual device's captured power to that of the first device in *obstacle case one, five* and *six*. The greatest decrease is observed in *obstacle case five*, as in this representation the device absorbs the most power. At each subsequent device however, the power captured stays quite similar ranging between five and six percent of the first device's power capture. In *obstacle case one,* the reduction in power capture for each subsequent device ranges between 1.5 and 2.5% of the first device's power capture and finally in *obstacle case six,* the decrease in captured power ranges between 3.5 and 4.5% indicating relatively small losses in power when devices are spaced ten device widths apart.

Table 7: Captured power [kW] produced by five devices placed ten device widths behind the previous for each obstacle case

	Captured Power [kW] for each device in series				
Obstacle case	1	2	3	4	5
1	88.50	87.13	86.69	86.52	86.45
5	88.50	83.79	83.39	83.35	83.34
6	88.50	85.23	84.91	84.82	84.79

Table 8: Percentage decrease in captured power produced by five devices placed ten device widths behind the previous for each obstacle case

	Percentage decrease [%] in captured power				
Obstacle case	1	2	3	4	5
1	0	1.54	2.05	2.24	2.32
5	0	5.32	5.77	5.82	5.83
6	0	3.69	4.06	4.16	4.19

Even though this test case was carried out for a single sea state, previous analyses have indicated applying the *obstacle case five* representation will result in an average 5.7% decrease between power produced by the first and second device when averaged over each sea state that occurred at the field case location in 2006 [109]. The shadowed device has been observed to produce as much as 9.8% less power than the first device in series in higher energy seas [109].

The results presented in this section are specific to the reference device and the device spacing chosen and as such, caution should be exercised in generalizing these results.

4.2 Field study: Amphitrite Bank

In this section, a case study is presented in which an array of fifty four devices is modelled six kilometres off the coast of Amphitrite Bank to meet the load requirements previously outlined by the local electrical utility [110]. Amphitrite Bank has been identified by the local power authority, BC Hydro, as a promising location for a WEC array due to its proximity to major grid interconnections at the community of Ucluelet, suitable bathymetry and a strong wave energy resource [110], [111]. The site was also identified as a promising WEC farm location in previous studies of the gross wave resource off the West Coast of Vancouver Island [55], [112].

4.2.1 Field Simulation Description

Three nested SWAN simulations were used to create the 54 unit WEC array model at Amphitrite Bank. Nested simulations use a larger spatial grid to generate boundary conditions at the boundaries of a smaller, higher resolution computational domain. Three domains were employed (two of which being nested grids) to allow for flexibility in generating the final domain in which the WEC array is placed. By employing an intermediate grid, the user can avoid running a SWAN simulation of a large, computationally expensive domain if changes are made to the orientation of the smallest grid. The structure of the nested runs and the inputs are displayed in Figure 47 followed by a more detailed description of each of the computational domains.

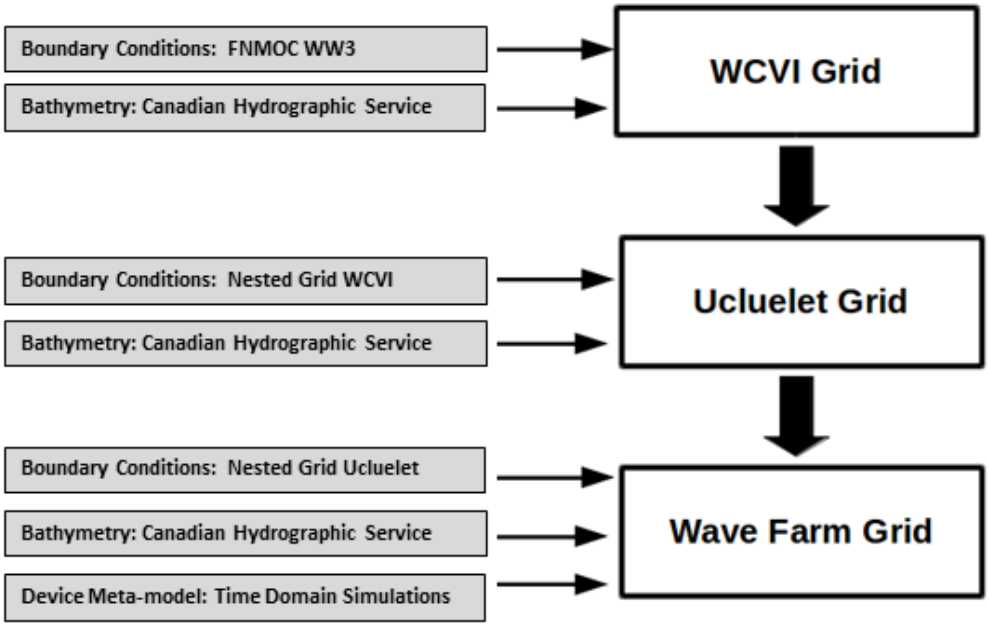

Figure 47: Nesting structure of the field case model for a farm of 50 devices

A pre-existing SWAN grid formerly used to characterize the wave resource off the West Coast of Vancouver Island (WCVI) [42] was used to determine the boundary conditions for subsequent simulations. Within the WCVI grid, the depth ranges from approximately 1000 metres at the continental shelf to zero depth at shore [55]. An unstructured computational grid for the WCVI region was generated using the grid

generation software TQGG[17] Unstructured grids allow for greater computational efficiency and improved resolution for wave effects in shallower regions. Grid spacing was specified proportional to water depth with the most highly resolved elements 50 metres in length. The bathymetry was interpolated onto the computational grid from 500m and 100m gridded bathymetry sets from the Canadian Hydrographic Service [42]. The grid covers over 410,000 square kilometres with over 130,000 computational nodes.

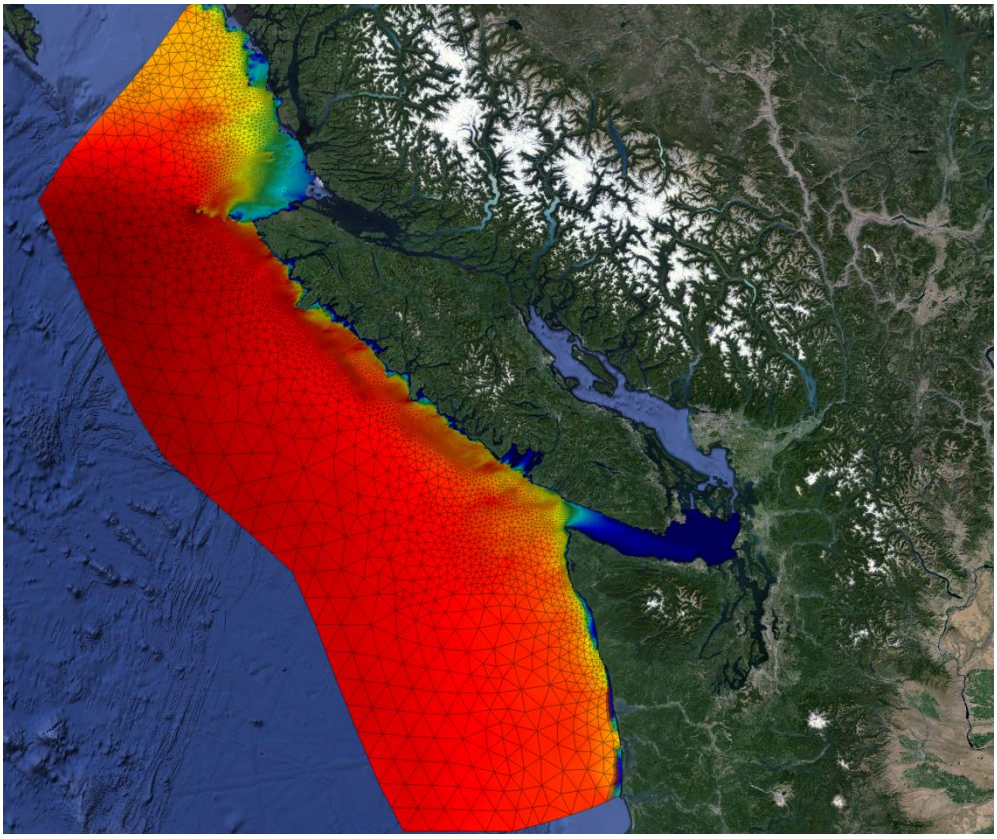

Figure 48: West Coast of Vancouver Island (WCVI) grid from which the boundary conditions of subsequent simulations are extracted. The surface presents the average H_s over the duration of the 2004-2013 Hindcast

Wave boundary conditions from the WCVI grid were obtained from an ocean-scale wind-wave model (WAM) operated by the European Centre for Medium Range Weather (ECMWF). Wind boundary conditions were gathered from the Coupled Ocean/ Atmosphere Mesoscale Prediction System (COAMPS) model developed by the U.S. Navy. The large WCVI grid was run with boundary conditions obtained from FNMOC

[17] https://github.com/rrusk/TQGG

WW3 for all of 2006 at a three hour resolution. Spectral data was output at the boundary nodes for the subsequent grid.

A higher resolution grid, shown in Figure 49, was generated off the coast of Ucluelet using the bathymetry files from the larger WCVI SWAN grid. The Ucluelet grid extends 30 kilometres off shore at the northern boundary and 53 kilometres offshore at the southern boundary of the grid. The Ucluelet grid is 110 kilometres in length with the lowest resolution at the offshore boundary where cell edges are 1.5 kilometres in length and the highest resolution near the coastline where cell edges are 200 metres in length. The Ucluelet grid contains 3571 nodes and 6693 cells.

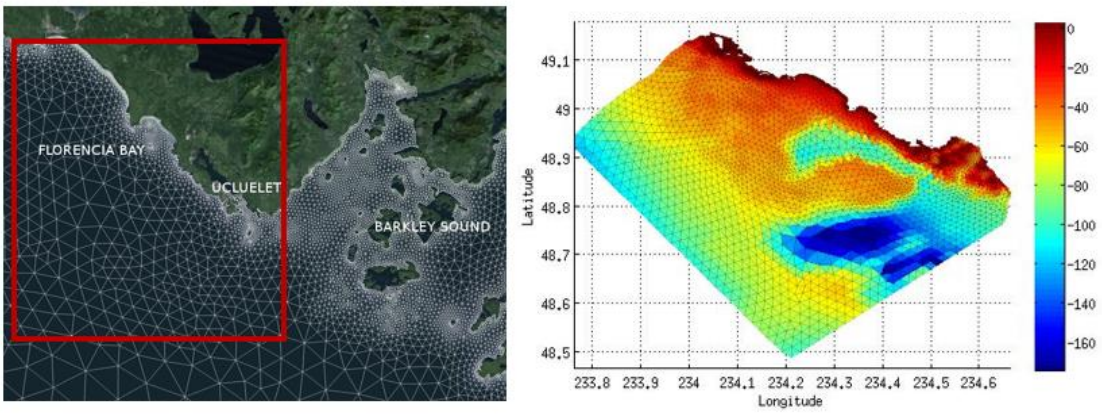

Figure 49: On the left, the unstructured grid used in the WCVI map is superposed onto the physical map of the Amphitrite Bank. On the right, the computational grid as run in SNL-SWAN is presented for the area indicated by the red outline on the left figure. Bathymetry is indicated by the color scale on the right. All depths are in metres.

Finally, a regular, structured Wave Farm grid was generated within the Ucluelet grid with the bottom left corner located at a longitude and latitude of 234.4 and 48.76 degrees respectively corresponding to an area of higher wave energy as seen in Figure 51. The Wave Farm grid has a 25 metre resolution in both the x and y directions and 630,000 nodes. A structured grid was employed to reduce numerical error diffusion that occurs in very fine unstructured grids. The x-axis is aligned with the principle wave direction with the y-axis perpendicular to it. The Wave Farm grid was angled at 80 degrees to be aligned with the mean annual wave direction (260 degrees) averaged over the duration of the hindcast between 2004 and 2013, as seen in Figure 50. The Wave Farm grid extends 20 kilometres along the x dimension of the grid and 28 kilometres in the y direction. It

should be noted that the regular Wave Farm grid is rectangular in Cartesian coordinates and takes on the shape of a skewed polygon when translated into latitude and longitude. The regular grid is the most resolved of the nested grids and is the grid on in which the wave farm constructed using SWAN's obstacle feature.

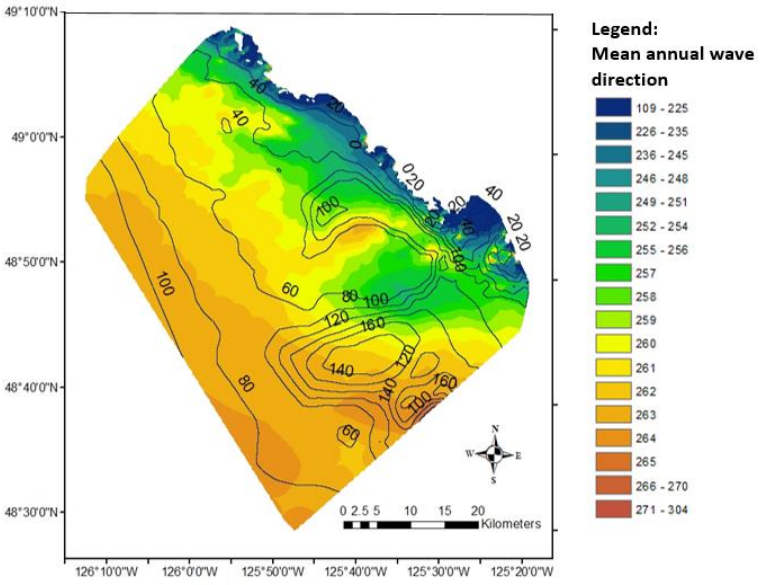

Figure 50: Map depicting the depth contours across the Ucluelet grid and the mean wave direction across the site averaged over 2004-2013

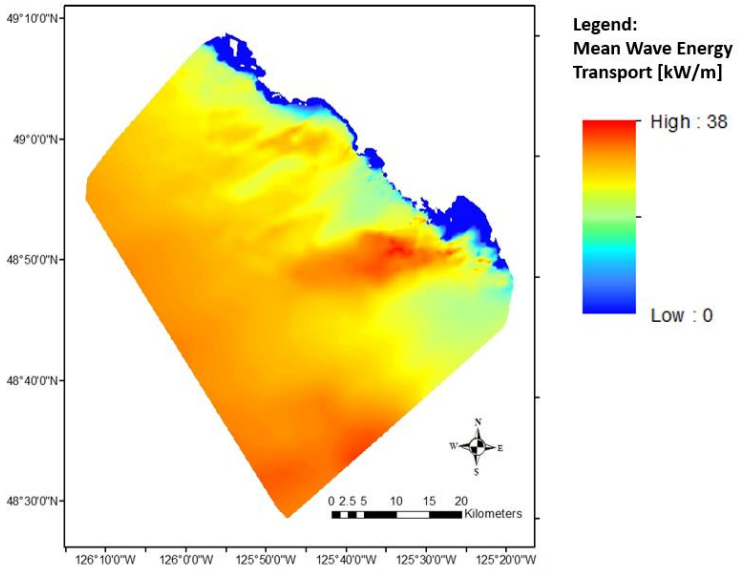

Figure 51: Map depicting the wave energy transport across the Ucluelet grid averaged over the years 2004-2013

4.2.2 Array Format

The array configuration used within this analysis was influenced by array spacing configurations previously suggested by Stratigaki [62] as well as practical electrical transmission considerations reported by MacArtney [113]. Devices were spaced at ten device widths in smaller subarrays of nine devices. Stratigaki recommends the installation of WECs in smaller arrays with at least a ten device diameter spacing between devices to limit far field impacts and reduce intra-array interactions between devices. Stratigaki reported a constructive effect of intra-array interactions for 3 x 3 arrays spaced ten device widths apart when experimentally testing arrays in long crested irregular waves [62]. The constructive interactions between these devices were decreased when 5 x 5 arrays were tested. It should be noted that even with constructive interaction between WECs, the devices on average performed less efficiently in an array than when individually deployed. Smaller subarrays of devices are also compatible with the recommended electrical infrastructure configuration previously suggested by the MacArtney Group [113]. The MacArtney study was focussed on the conceptual design of the subsea electrical infrastructure required for a WEC array installation on Amphitrite Bank. Components of the electrical system were drawn from MacArtney's established products used in offshore wind energy applications. Modular hubs are used to connect and combine inputs from multiple dynamic cables connected to individual WECs and export the power.

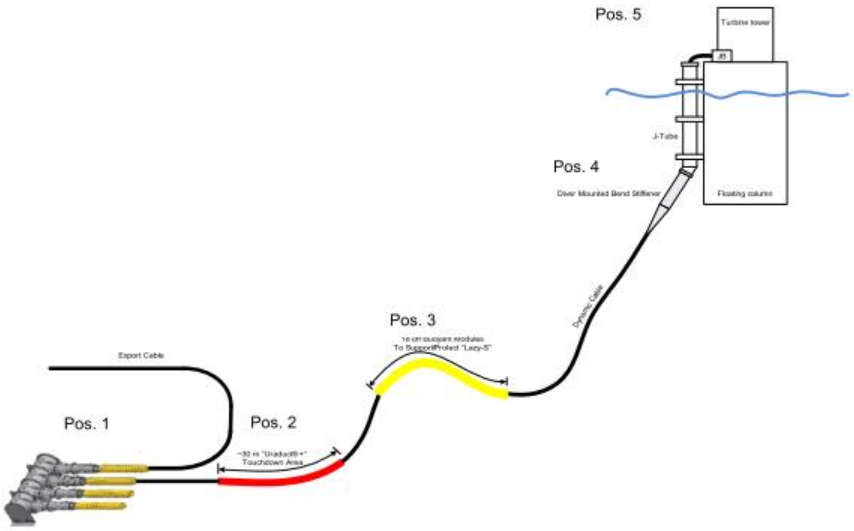

Figure 52: Diagram presenting one device connected to a modular hub [113]

In practice, the number of connections to the hub is limited by the electrical rating of the export cable, which necessitates the need of smaller arrays. MacArtney's study concluded with a 54 device layout within which three devices are connected to each modular hub in smaller arrays of nine devices [113].

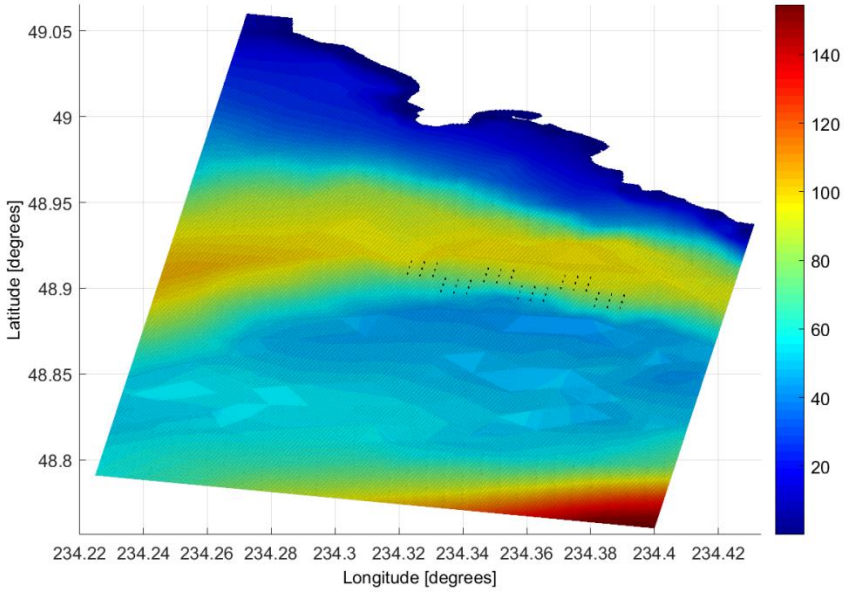

Figure 53: Position of 54 WEC devices presented within in the computational domain superposed on the domain's depth

4.2.3 Field Case Results

The computational domain presented in Figure 53 was modelled with boundary wave conditions in 2006 with a three hour time step. The boundary conditions were determined based on the nesting procedure outlined in Figure 47. The WCVI grid was run for 2006. This model run saved boundary conditions at nodepoints corresponding to the Ucluelet grid's boundary nodes for the duration of the year. The Ucluelet grid was then evaluated with the previous simulation's outputs and the outlined procedure was repeated for the Regular Wave Farm grid boundary conditions.

In order to compare the performance of *obstacle case one*, *five* and *six* with respect to annual energy production and far field impact, four chief model outputs were recorded from the simulations. First, the power captured by each WEC was recorded for each time step in the simulation. Second, the H_s, $T_{p,}$ peak direction and energy transport, from

herein collectively referred to as bulk parameters, were recorded for each node surrounding the WEC array, as can be observed in Figure 57 through Figure 62. The bulk parameters at these field points are used to visualize the interaction between devices within the farm, ultimately allowing one to understand why certain changes in power production may occur between the devices. The bulk parameters were interpolated at cross sections through the Wave Farm grid at 100, 200, 500, 1000 metres behind the array and also at a location close to the shoreline in order to determine the far field impact the WEC array has on the very near shore region. These cross sections are presented in Figure 54.

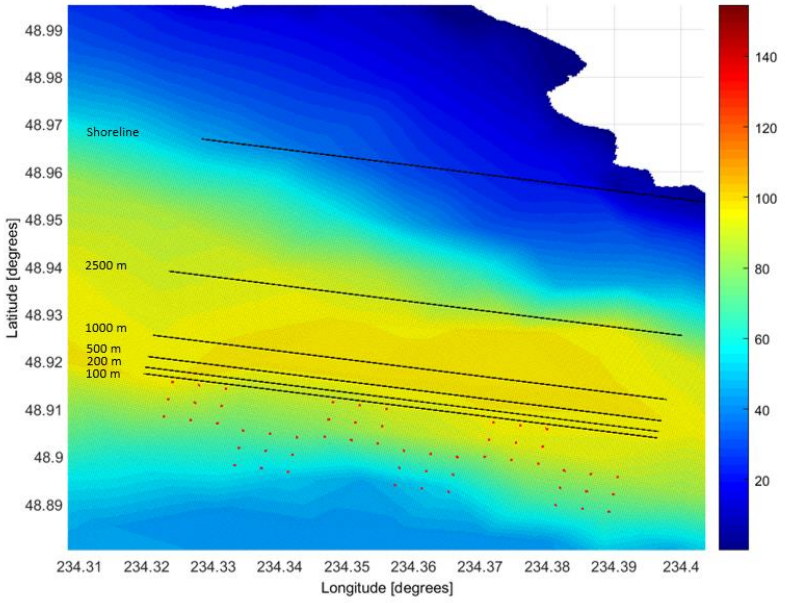

Figure 54: Location of the far field impact lines, as located behind the array of 54 WECs superposed on a depth plot for a section of the computational domain.

The simulations conducted for this work required 3774 hours of CPU time and were run in both series and parallel on five machines each with 16 cores. Simulations run with obstacle case five required more CPU time than obstacle cases one and six. The author presumes this is due to the large decreases in H_s incurred with representing a device with *obstacle case five*. As a result, SWAN needs to iterate more for each time step in order to find a solution that meets the user's convergence criteria set in the input file.

The remainder of this section is split into two primary parts. First, the impact the WEC array has on the surrounding wave field – both with respect to far field and intra-array

impacts is investigated. Secondly, how power production is impacted by the device representation is analyzed

Impact on the Surrounding Wave Field

The WEC array's impact on H_s was analyzed for *obstacle cases one*, *five* and *six* both spatially, by analyzing the cross sections behind the device presented in Figure 53, as well as temporally. First, the percentage decrease in H_s averaged over 2006 is analyzed at cross sections 100 metres, 1000 metres and at the shoreline in Figure 55.

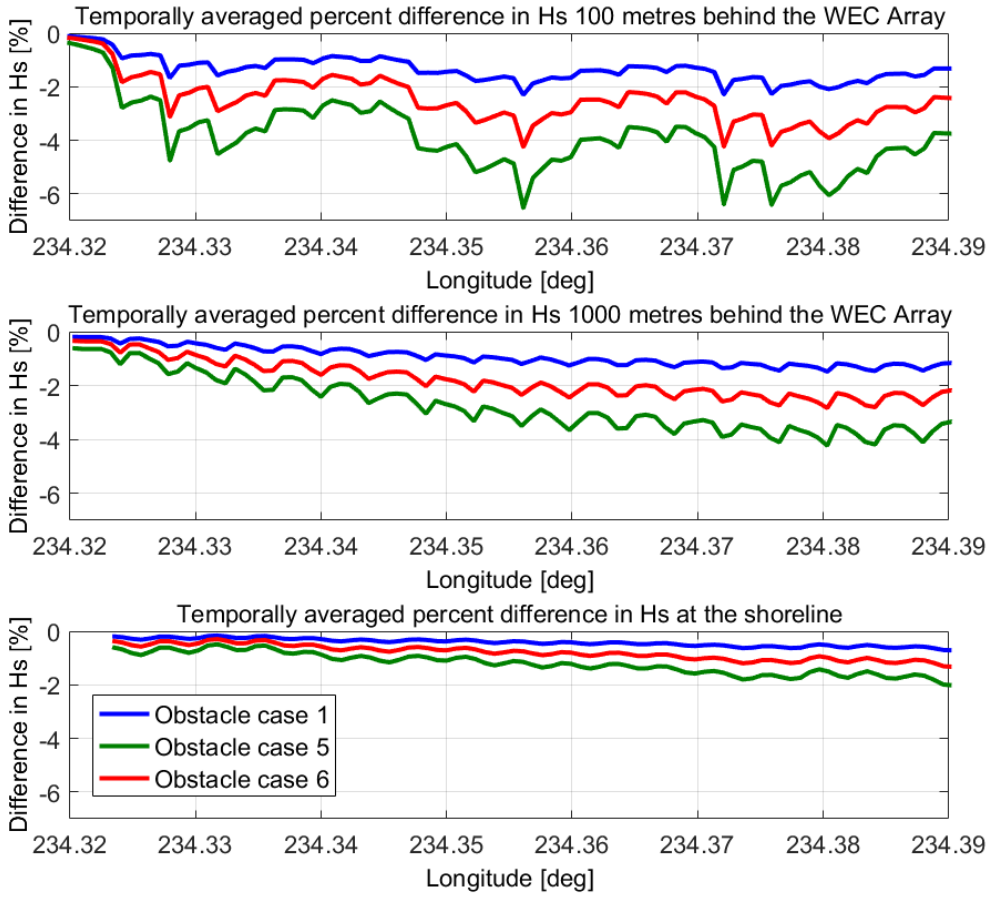

Figure 55: Decrease in Hs averaged over 2006 as observed at cross sections behind the WEC Array presented in Figure 54

The greatest decrease in H_s is observed 100 metres behind the device for each obstacle case. Patterns similar to those presented in the flat bottom simulations are observed in that *obstacle case five* has the greatest impact on the surrounding wave field, followed by *obstacle case six*. A more detailed discussion on why *obstacle case five* removes more

power than *six* was previously presented in Section 4.1.2. The mean percentage decreases in H_s behind the array at the cross sections presented in Figure 54 is presented in Table 9.

As a result of the mean wave energy transport approaching the farm from the west over most of the year, the greatest decrease in H_s is observed behind the devices near the eastern extent of the array. The computational grid was angled according to the mean wave direction over the duration of the 2004-2013 hindcast however in 2006, the waves approached Amphitrite Bank more from the west. The author anticipates if the grid were angled to the dominant wave direction, there would be a horizontal, averaged wake behind the array. In the top plot of Figure 55, the reader may also observe a greater decrease in H_s at longitudes 234.328 and 234. 356. These coordinates correspond to where two adjacent 3 x 3 arrays meet. The impact of the two neighbouring arrays is no longer observed 1000 metres behind the device, however the eastern extent of the array remains more affected by the presence of the array. Finally, near the shoreline, regardless of the obstacle case employed, less than a two percent decrease in H_s is observed.

Table 9: Temporally and spatially averaged difference in H_s observed at the specified distances for each device representation.

	Distance from Array [metres]				
Obstacle case	100	200	500	1000	Shoreline
1	-1.34	-1.27	-0.95	-0.63	-0.44
5	-3.86	-3.66	-2.79	-1.87	-1.27
6	-2.46	-2.34	-1.83	-1.26	-0.84

In addition to the average difference in H_s observed over the course of a representative year, it is important to consider the condition which would decrease the H_s most. Significant wave height cross sections corresponding to December 6, 2006 at 18:00 are presented in Figure 56. This time step corresponds to when *obstacle case five* removed the most energy from the WEC array in 2006. At this time step, the mean energy transport direction is coming from the east creating a more prominent decrease near the eastern extent of the WEC array. The greatest decrease across the 100 metre cross section approaches a 15% decrease in H_s when *obstacle case five* is employed. Even when the far field impact is deemed the worst, the reduction in H_s at the shoreline is observed to be less than 5% regardless of the representation used for the WEC array. The cross sections

at which the significant wave height was recorded are presented in Figure 54. A more detailed list of H_s decreases for each of the obstacle cases is presented in Table 12.

Table 10: Spatially averaged difference in H_s observed on December 6, 2006 at the specified distances for each device representation.

	Distance from Array [metres]				
Obstacle case	100	200	500	1000	Shoreline
1	-2.26	-2.17	-1.72	-1.10	-0.57
5	-7.57	-7.23	-5.67	-3.54	-1.80
6	-4.38	-4.15	-3.09	-1.71	-0.72

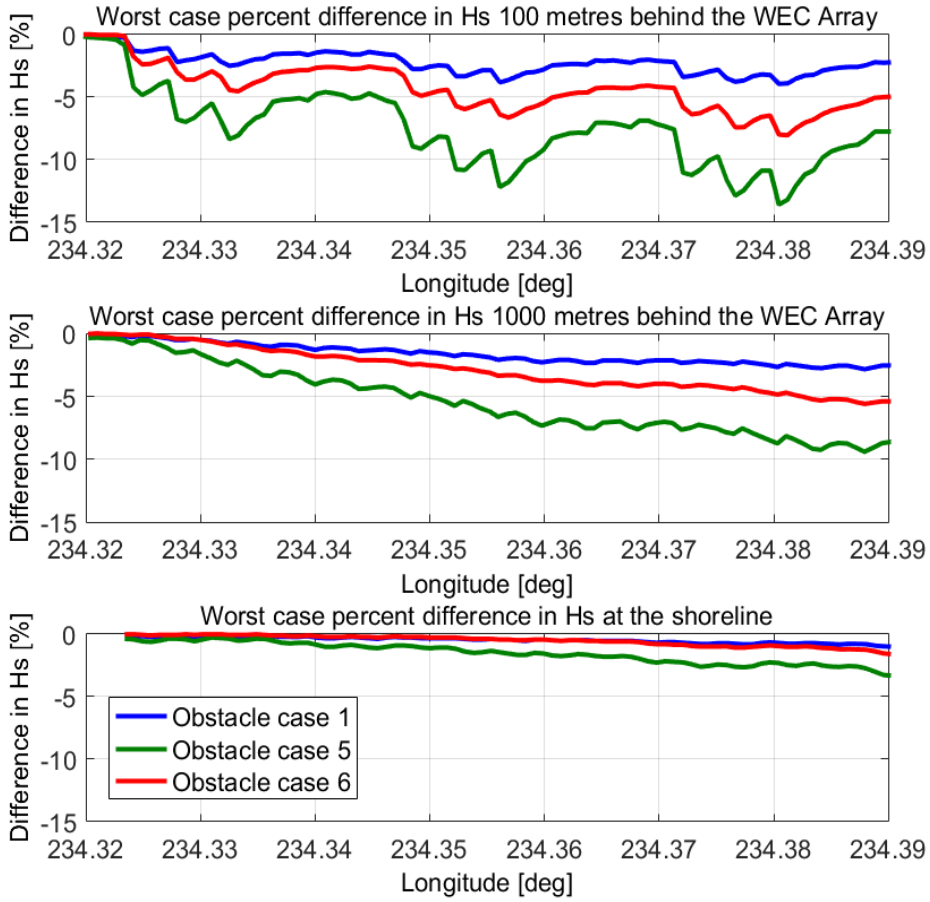

Figure 56: Decrease in Hs observed at the cross section behind the WEC Array, as presented in Figure 54 on December 6, 2006 at 18:00 hrs

In addition to the impact the farm has on H_s, bulk parameters are analyzed within the vicinity of the WEC array. Figure 57 through Figure 59 present the H_s, direction of the energy transport, peak direction and the T_p in the wave field surrounding the farm in the

most commonly occurring sea state in 2006. Figure 60 through Figure 62 present the same bulk parameters for a higher energy sea, demonstrating how the device behaviour is impacted by the WEC representation in more extreme conditions defined in Table 11.

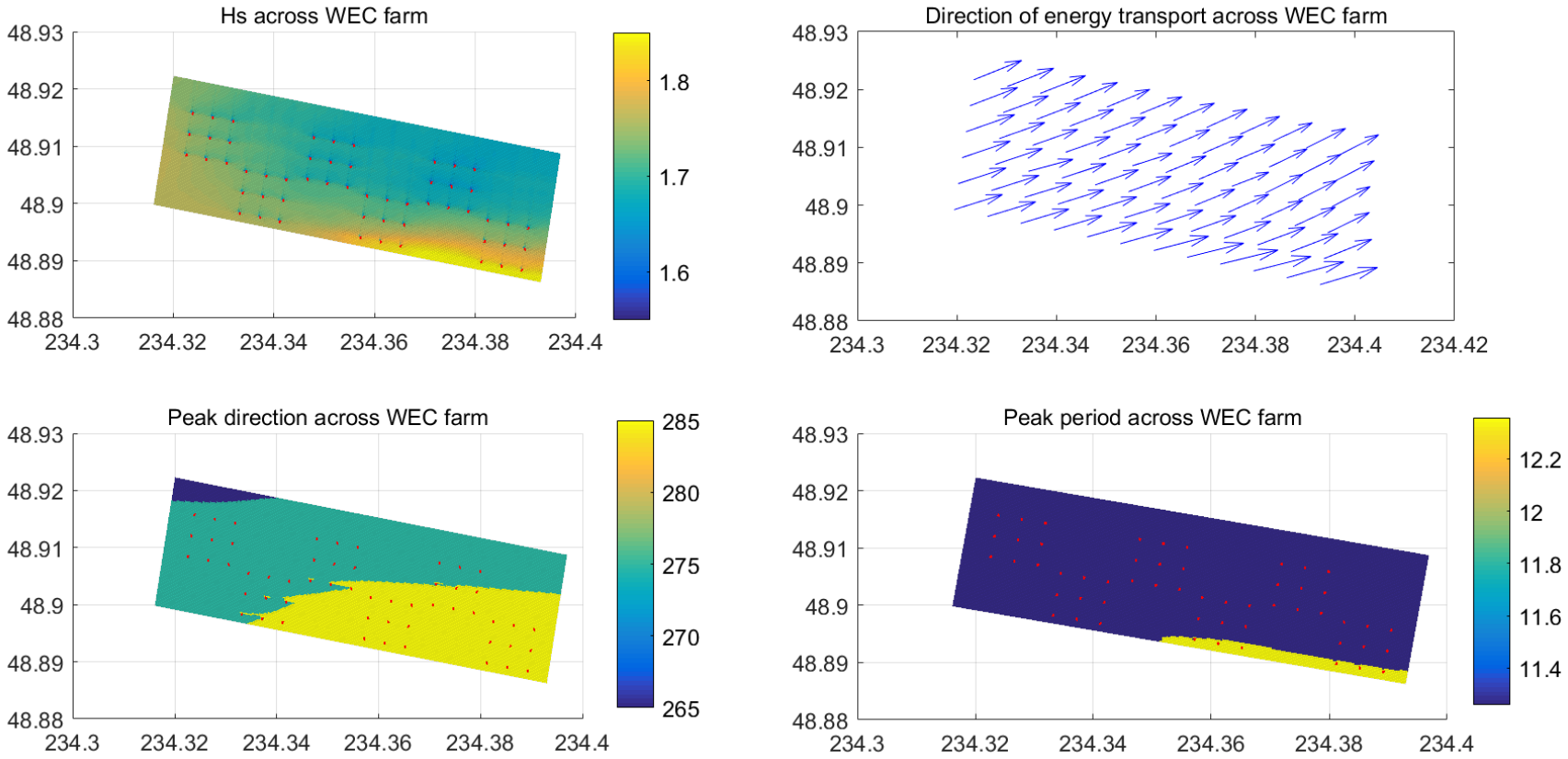

Figure 57: Bulk Parameters plotted across the WEC farm for the most commonly occurring sea state when devices represented with obstacle case one

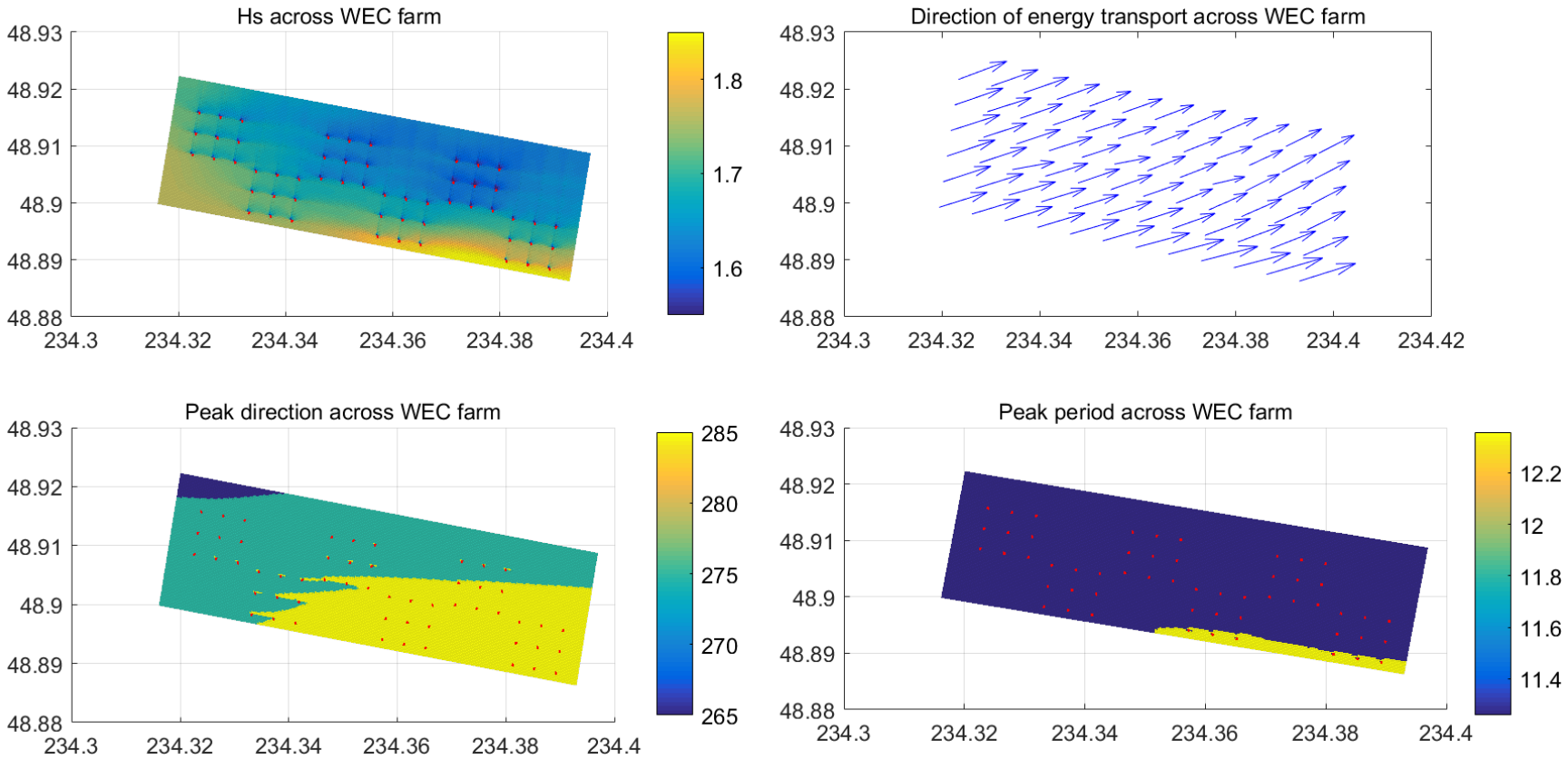

Figure 58: Bulk Parameters plotted across the WEC farm for the most commonly occurring sea state when devices represented with obstacle case five

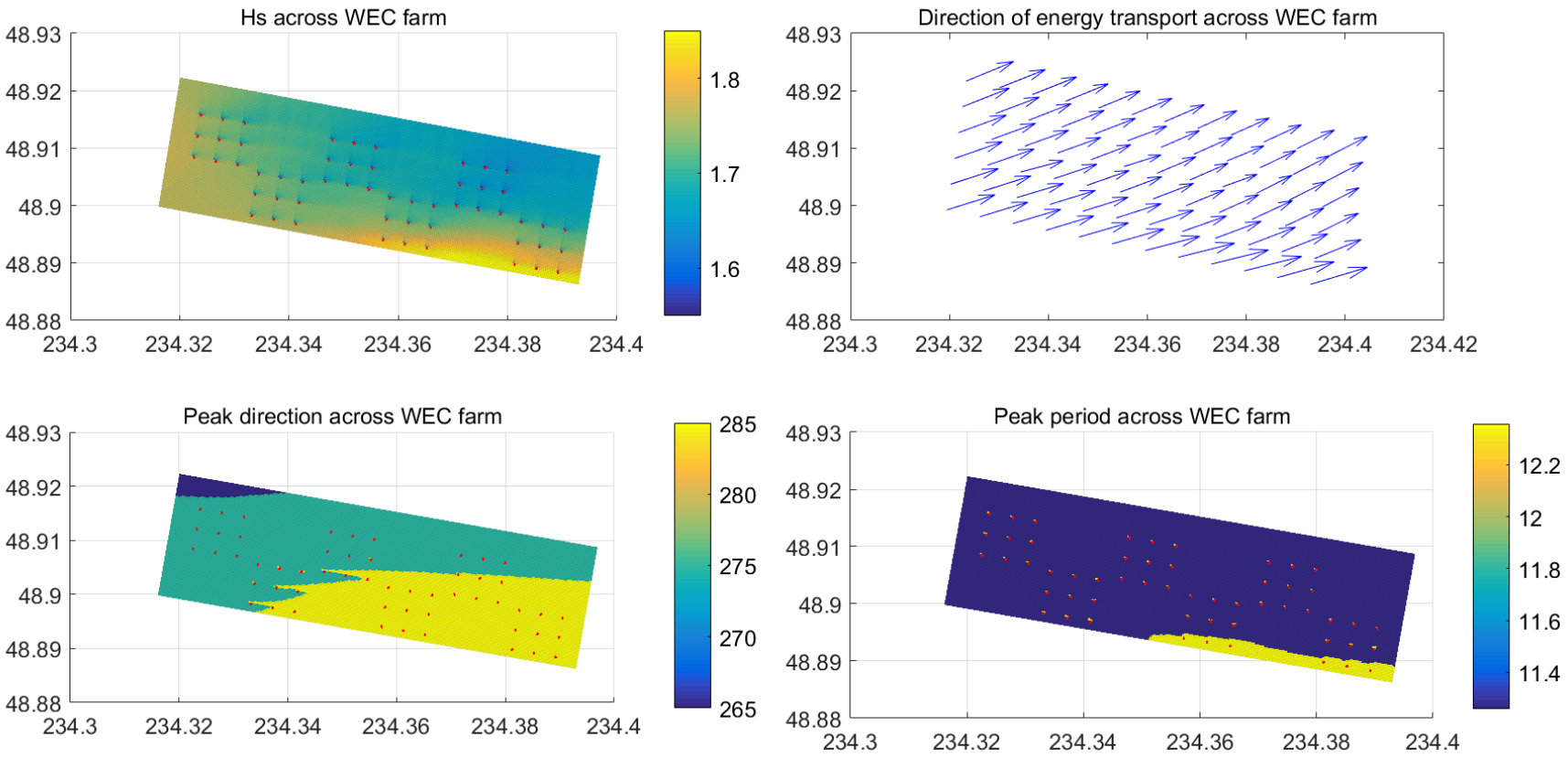

Figure 59: Bulk Parameters plotted across the WEC farm for the most commonly occurring sea state when devices represented with obstacle case six

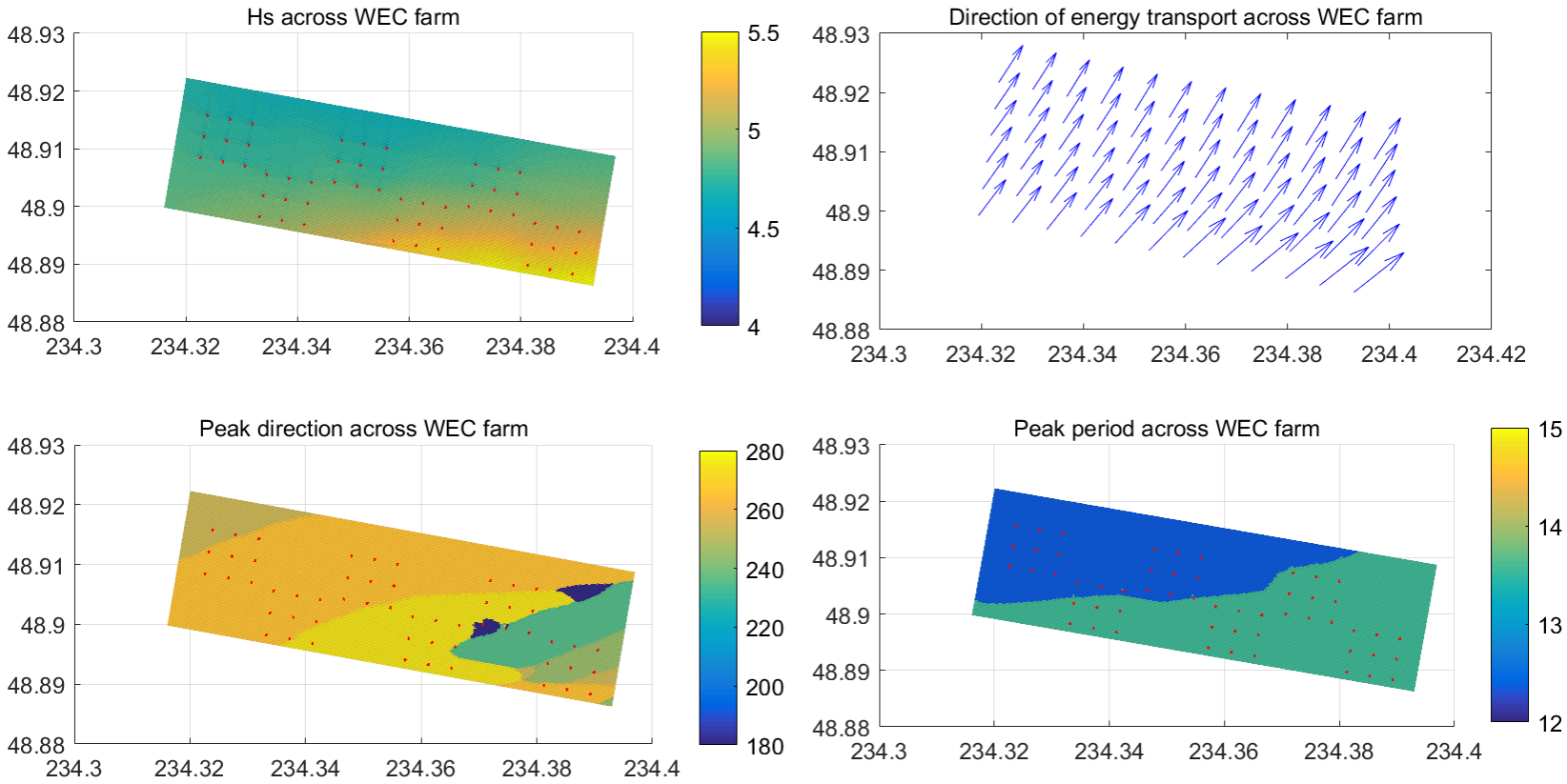

Figure 60: Bulk Parameters plotted across the WEC farm for a high energy sea (Hs = 4.75 m, Tp = 13.5 s) when devices represented with obstacle case one

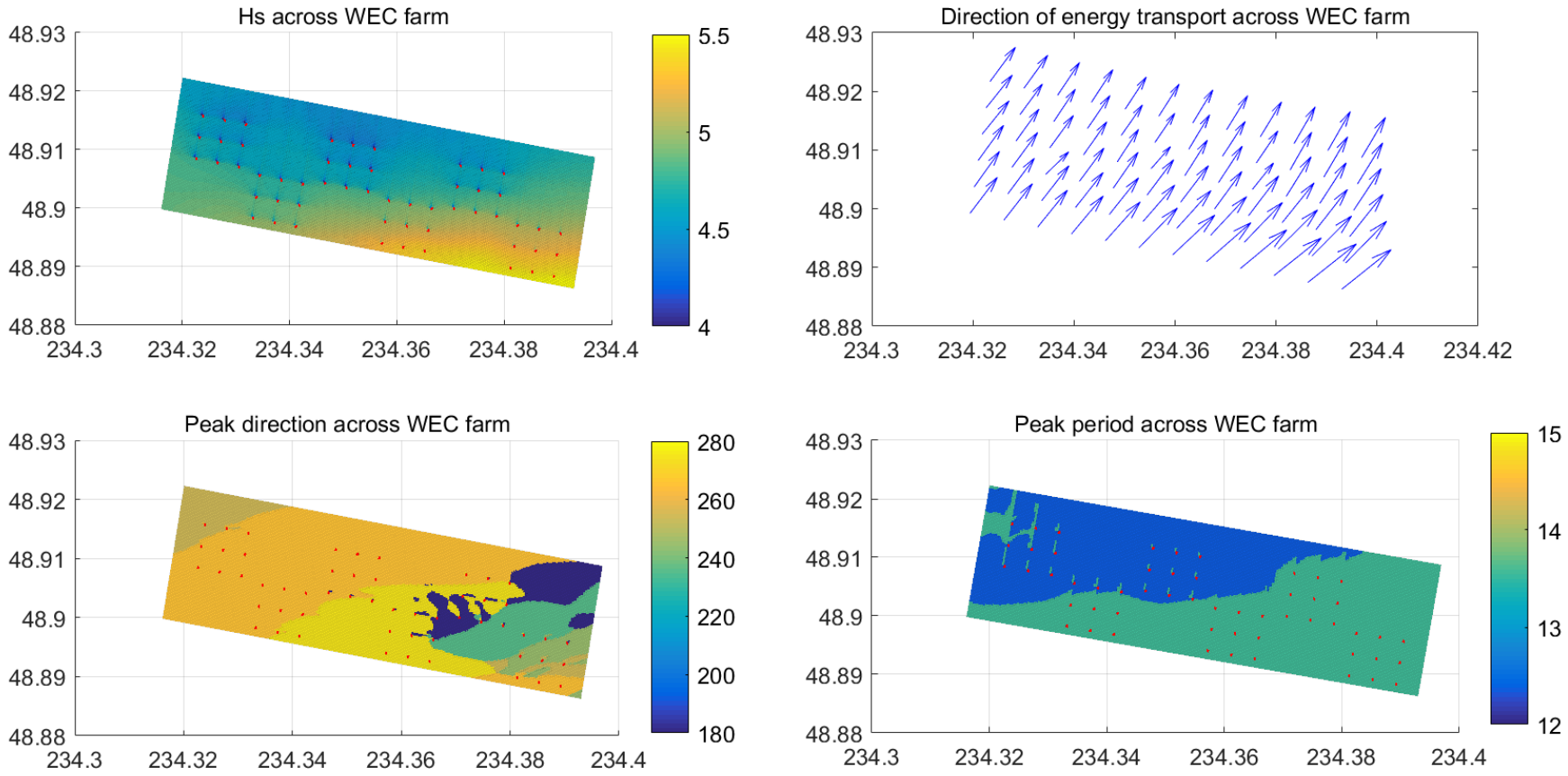

Figure 61: Bulk Parameters plotted across the WEC farm for a high energy sea (Hs = 4.75 m, Tp = 10.5 s) when devices represented with obstacle case five

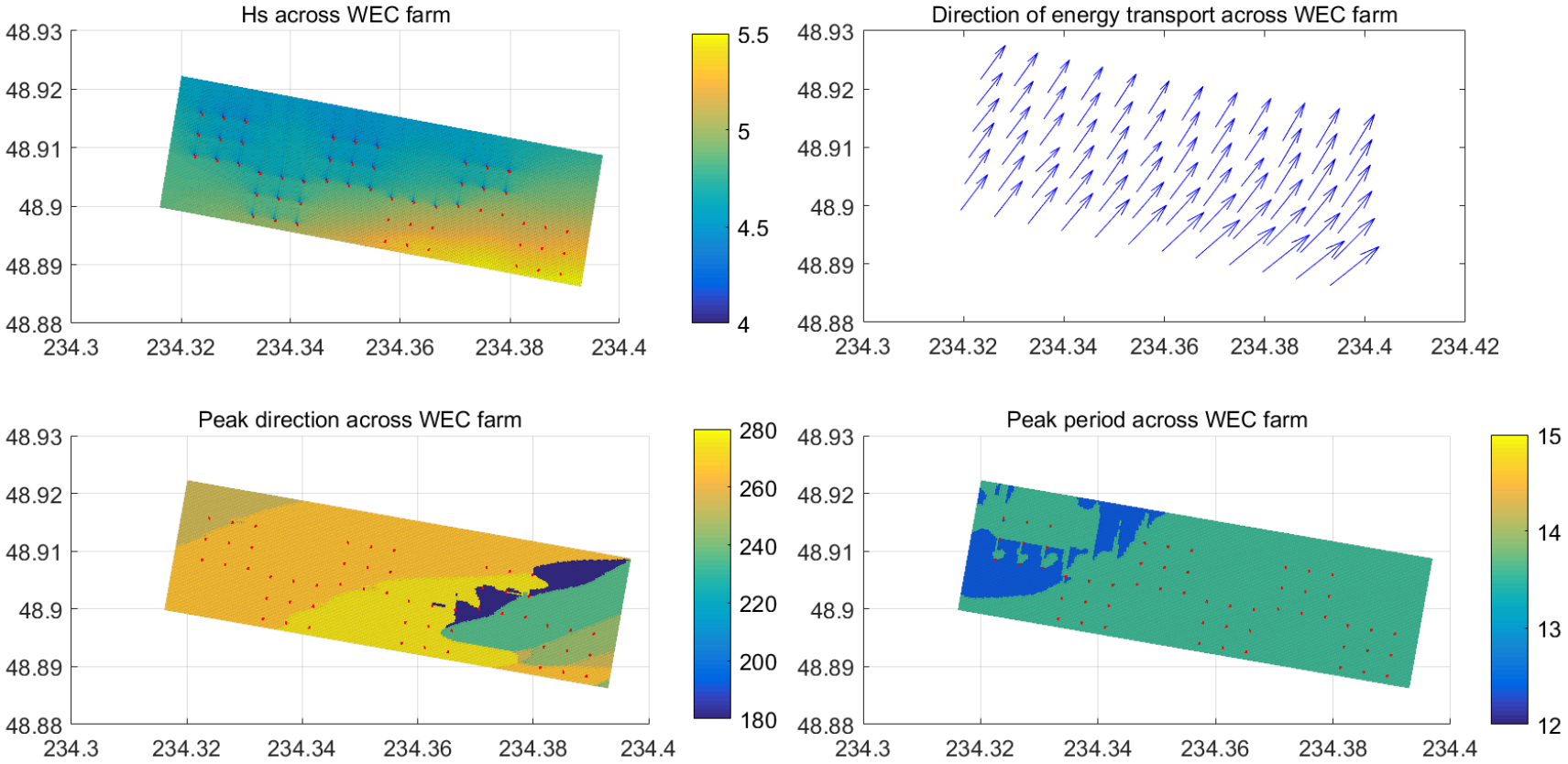

Figure 62: Bulk Parameters plotted across the WEC farm for a high energy sea (Hs = 4.75 m, Tp = 10.5 s) when devices represented with obstacle case six

Table 11: Description of wave conditions under which obstacle cases one, five and six were analyzed for the field case

Description	H_s [m]	T_p [s]
Commonly occurring	1.75	11.1
High Energy	4.75	13.5

In the most commonly occurring sea state, the greatest difference between the three device representations is observed in the H_s. field. The H_s is most prominently decreased in the lee of the fifth 3 x 3 array from the left. Because the energy transport is approaching the WEC array from the east (as seen in the top right plot of Figure 60 through Figure 62), the energy spectrum incident to the WEC array has already been perturbed by the second and fourth 3 x3 array. The change in H_s in the lee of the device at 100, 250 and 1000 metres is presented in Figure 63 below. The reader may also note that when the energy transport is directed perpendicular to the array the decrease in H_s is more uniform across the width of the array.

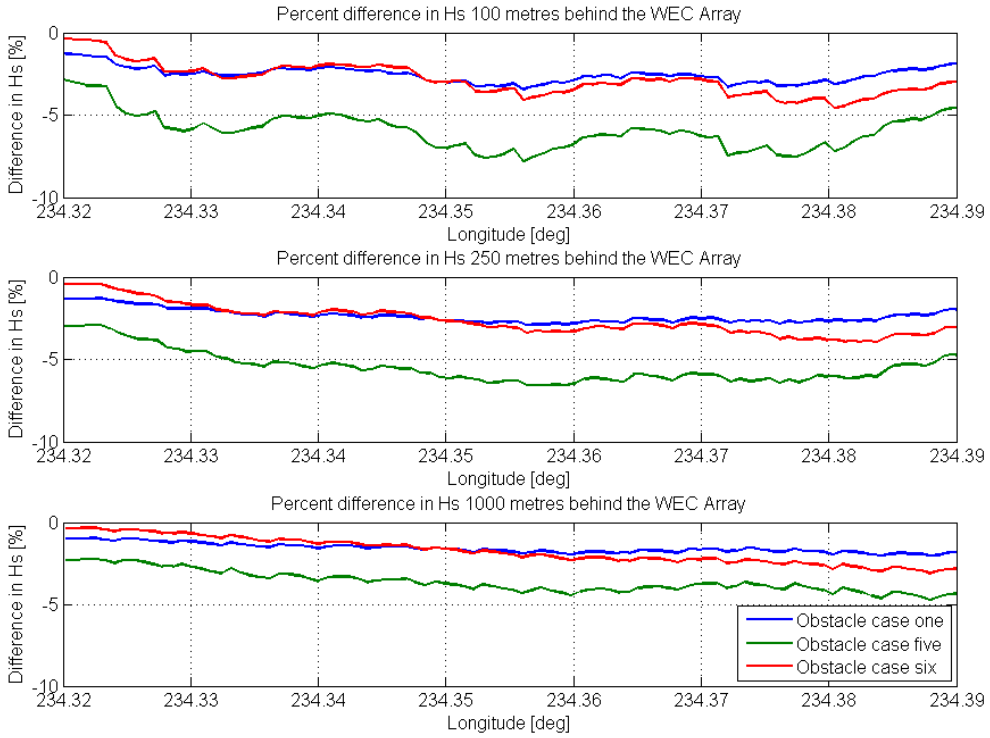

Figure 63: H_s interpolated at 100, 250 and 100 metres in the most commonly occurring sea state in 2006

The peak direction of the waves propagating across the WEC farm are influenced by the WEC representation to a lesser degree. In Figure 57, the peak direction surrounding the fourth, sixth and part of the fifth array is 285 degrees. At a closer glance, directly in the lee of certain devices in the second and third array, there are also pockets of 285 degree peak direction. When *obstacle case five* is employed, additional pockets of 285 degree peak directions manifest themselves around devices in the corner of the second array from the left. This effect is very small because this is not a very high energy sea.

The peak period is relatively unaffected by the device representation in an $H_s = 1.75$ metre and $T_p = 11.1$ second sea. If one looks closely at the peak period plot in Figure 59, the peak period jumps to 12.4 seconds directly in the lee of each of the devices characterized with *obstacle case six*. It appears that in this particular sea state, most of the energy was extracted from the peak of the incident energy spectrum. As a result, a new peak was created. Because of the directional spread of the incoming waves, and as these waves diffract around the device, the spectrum assumed its original shape as it travels further from the device. This phenomenon was also seen in Figure 42 when the spectrum behind a single device was observed. The author believe that a more continuous variation in the mean period would be seen across the computational domain however, the peak period was analyzed as it is used to determine the power absorbed by the device from the power matrix.

More prominent changes in the wave field can be observed when the three obstacle cases are observed in a higher energy sea state, such as the one presented in Figure 60 through Figure 62. Similarly to the lower energy sea, the greatest decrease in H_s can be observed in Figure 61 corresponding to *obstacle case five*. The first, third and fifth array undergo the greatest decrease in H_s, as their wave field is partially shadowed by the first, third and fifth arrays. This effect is presented more clearly in Figure 64 where there are greater dips in the H_s directly in the lee of the first, third and fifth arrays for each of the obstacle case. At 250 metres behind the device, the array configuration's impact on the H_s profile is still observed while at 1000 metres, the decrease in H_s is uniform along the length of the array.

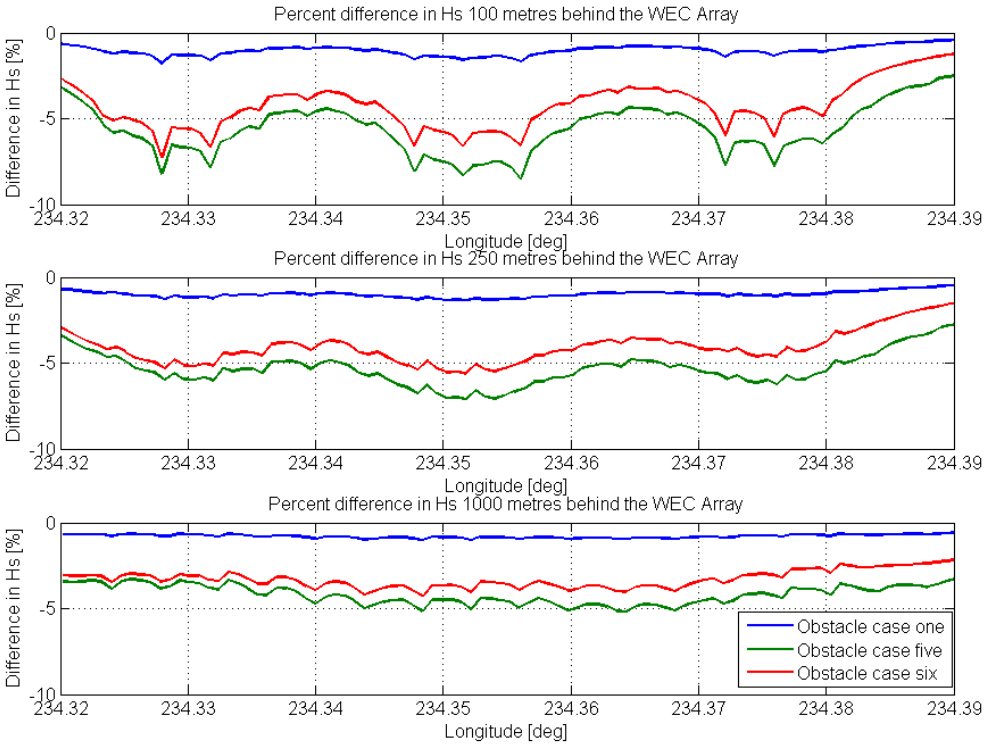

Figure 64: H_s interpolated at 100, 250 and 100 metres in a high energy sea

The direction of the energy transport remains unaffected between the three obstacle cases. The peak direction plot however demonstrates how each obstacle case impacts the peak direction within the array. In obstacle case one, a small pocket of waves is observed where the peak direction is 155 degrees, opposed to the incoming waves which range between 255 and 275 degrees. The peak direction is most drastically changed in *obstacle case five*. It is believed that the devices are extracting so much power from the incident component of the energy transport projection that the peak direction of the energy spectrum begins to change. This hypothesis is supported by the fact that the peak direction is reduced to a value that's roughly perpendicular to 255 degrees.

The peak period is also impacted by the device representation. In Figure 60, the peak period changes across the WEC farm as a result of a storm approaching the farm. An increase in H_s can also be observed along the same front in the top left plot of Figure 60. In Figure 61 and Figure 62, this change in peak period is observed further across the farm, most prominently directly in the lee of the devices on the western extent of the farm.

Field Case Annual Energy Production

The different representations used to model the WEC array on Amphitrite Bank impacted the assessment of power production. Over the course of a year, the different representations employed to characterise a WEC array installed off of Amphitrite Bank resulted in a mean percentage decrease in power of 3.8% when *obstacle case one* was compared with *obstacle case five*, and a mean percentage decrease of 2.7% when *obstacle case six* and *obstacle case one* were compared, as stated in Table 12, indicating that including hydrodynamic losses does influence the power produced by a WEC array, even at a ten device width spacing where the incident energy spectrum has almost fully recovered, as was seen in Figure 42.

Table 12: Annual Energy Production for a Farm of 54 devices deployed off of Amphitrite Bank in 2006 when represented with three different representations in SNL-SWAN

Obstacle case	Annual Energy Production (GWh)	Percentage Difference
1	47.4	0
5	46.0	-2.9
6	46.3	-2.3

On aggregate, including the intercepted power in the device representation reduces the mean farm power production by less than five percent. However, the performance of an individual device in an array is more drastically affected. To gain a better appreciation for how a device's power production can change temporally, the difference in power production for a device is presented in Figure 55. One may observe that on average *obstacle cases five* and *six* remove more power from the incident sea than *obstacle case one* however there are instances when the intercepted power representations will suddenly produce much more, or much less power (as depicted by the spikes in power production) because of a local shift in T_p. The line is discontinuous in the bottom plot of Figure 65 where no power is being produced by any of the devices.

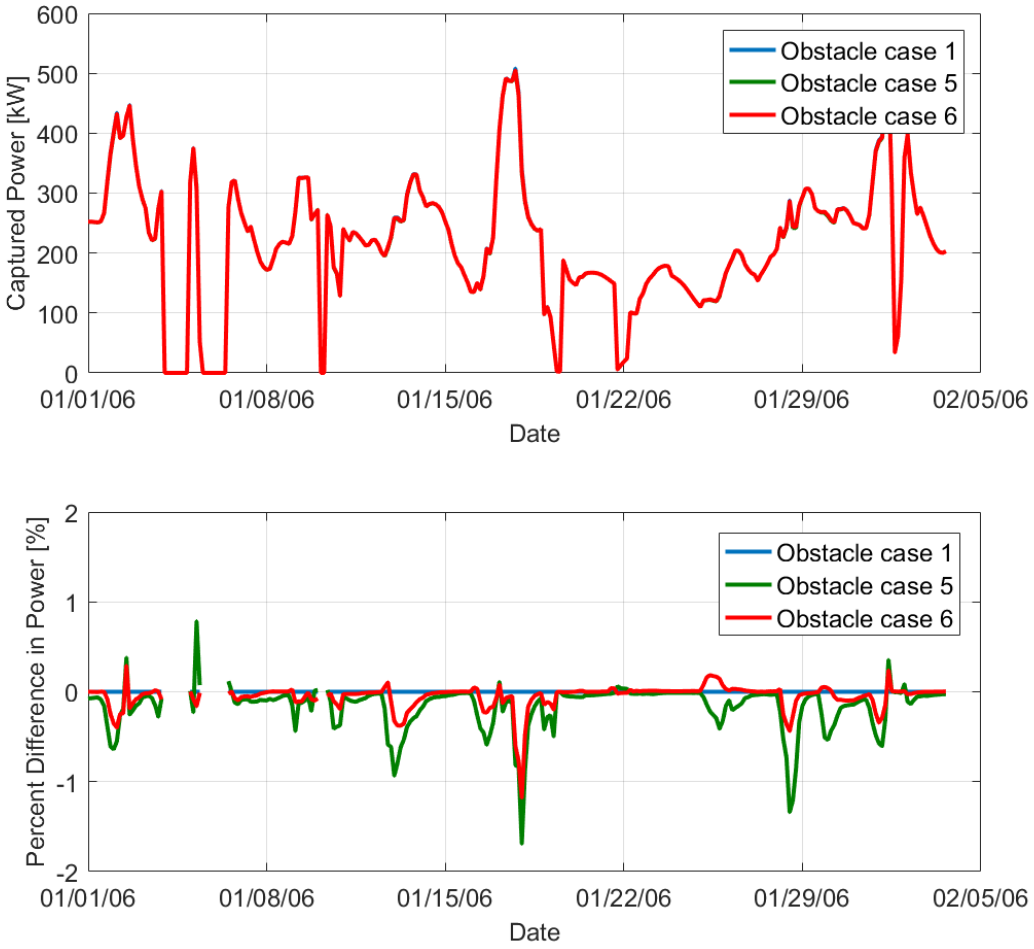

Figure 65: Time Series of the captured power by a device in the first row of the first array in January 2006 (top). The difference in power produced by a device using when comparing between different obstacle cases and the baseline (obstacle case one)

Figure 66 presents the percentage difference in annual energy production (AEP) for each device in the array to the reference representation (*obstacle case one*). The greatest decrease in power production when employing *obstacle case five* is observed in the eastern most device in the fifth array from the left. An 8.1% decrease in captured power is observed largely due to the fact that this device is the most shadowed over the course of the year. The same trend is observed when *obstacle case six* is analyzed.

Even though *obstacle case five* and *six* should theoretically remove the same amount of power from the incident wave spectrum, the RCW matrix generated for *obstacle case six* assumed a Pierson Moskowitz spectrum when normalizing the power absorbed by the

device. If the spectrum incident to the farm has a different shape, the transmission coefficients derived may be applied to bins containing different magnitudes of energy density than assumed in the preprocessing step. Because *obstacle case five* reduces the incoming spectrum by a constant transmission coefficient, this representation is less sensitive to spectral shape and appears to remove more energy from the incident sea.

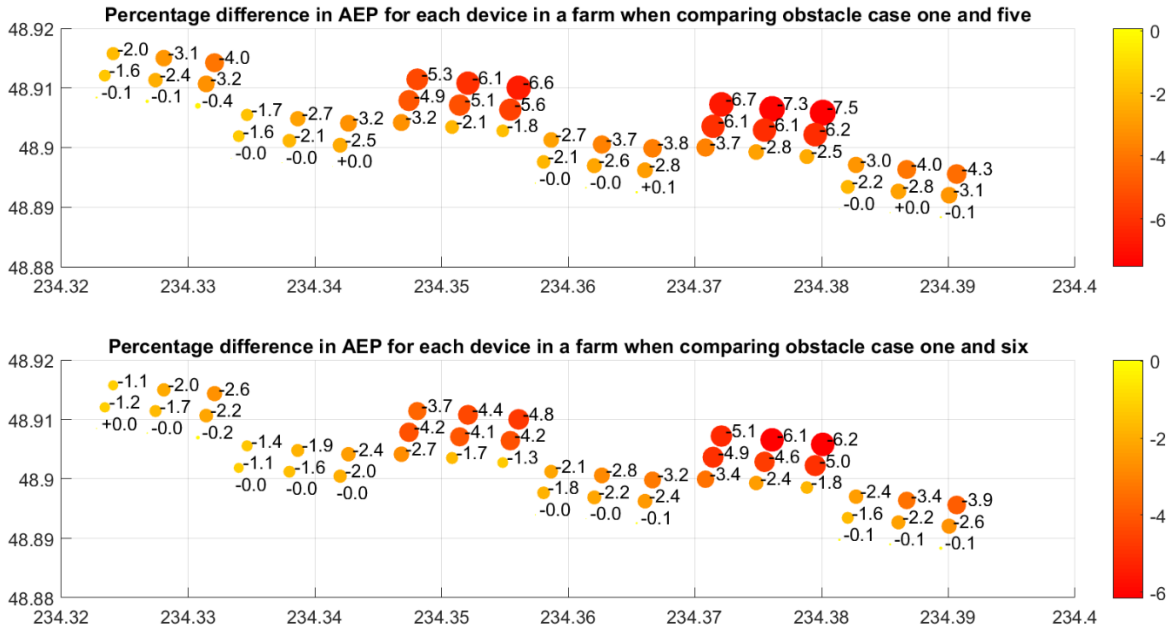

Figure 66: Percentage difference in annual energy production between obstacle cases one and five (top) and one and six (bottom)

It is also interesting to note that there is a decrease in captured power in the first row of devices in the array for both *obstacle cases five* and *six* as seen in Figure 66. The author believes this phenomenon is caused by wave directions coming from 180 degrees during some instances over the course of the year. Devices closer to the western extent of the array are shadowed by those located further east and by extension produce less power over the course of the year.

Comparing the annual energy production of the array when represented with different obstacle cases is subject to significant smoothing over the different incident wave directions and amplitudes experienced by the WEC array. Figure 67 compares the power produced by each device in *obstacle case five* and *six* in the most commonly occurring

sea previously presented in Figure 57 through Figure 59. Because the energy transport was coming from the east, the greatest reduction in power is observed in the western most devices. In a real field case, another potential source of error comes to light. *Obstacle case six* has transmission coefficients assigned to particular bins assuming that the incident spectrum was a Pierson-Moskowitz spectrum with a cosine squared directional spread. In this field case, there may be real spectra that may not resemble the reference spectrum, causing the same transmission coefficient to be applied to a different amplitude of incident power.

Figure 67: Percentage difference in power produced between obstacle cases one and five (top) and one and six (bottom) for the most commonly occurring sea

The difference in power production is also compared between *obstacle cases five* and *six* for a higher energy sea in Figure 68. This case is particularly interesting because the devices on the eastern flank of the WEC array produce more power in *obstacle case five* than in *one*. In *obstacle case five*, the reduction in H_s by the first row of device in the fourth, fifth and sixth 3 x 3 arrays decrease the H_s to such an extent that a higher power production value is being interpolated for the devices in the lee. A similar phenomenon is

observed when one compares *obstacle case six* and *obstacle case one*. On the western flank, once again, another bin is being referenced in the captured power matrix. One may observe in Figure 62 that the peak period is 13.56 s for almost the entire array while this is only the incoming condition on the right in Figure 60. The difference in peak period, combined with the decrease in H_s in the lee of the first row of devices change the incident condition to the shadowed devices.

The results presented are subject to a spacing that was set to ten times the device width and an array layout that was trying to minimize interference which is subject to change if another configuration is employed by the user. The results lend hope that a second row of 54 devices could be built behind the current one and still perform quite well. The performance of this second row will depend on how the devices are represented and as such we may see accumulating differences in the estimates made using obstacle cases one, five and six in that case

Figure 68: Percentage difference in power produced between obstacle cases one and five (top) and one and six (bottom) for the higher energy sea

Chapter 5

Unresolved issues

Over the time the author has spent working to improve the representation of a WEC device in SNL-SWAN, certain limitations imposed by the structure of the existing SNL-SWAN source code have been revealed. Some of these limitations are inherent to the device's representation as an 'obstacle' in SWAN, some stem from the finite set of time domain simulations used to populate the representation and some arise from practical limits made to keep the computational expense of the proposed methodology low.

This chapter is divided into three parts. Section 5.1.1 describes physical limitations imposed by the way the obstacle is applied within the finite difference solution of a spectral action density balance. Section 5.2 lists assumptions and approximations made within the time domain model which can lead to an inaccurate representation of the device. Finally, Section 5.3 identifies systematic error that occurs in the post processing of the time domain data and finally Section 6 presents the need to validate the work presented.

5.1 Device Representation in SWAN

Representing a device as an obstacle was a convenient and natural first step when trying to include a WEC in a coastal model however, as with any simplification, limitations exist to this approach. This section outlines issues associated with the geometric representation of a device within SWAN and the representation of the radiation within the model.

5.1.1 Geometric Representation

In SWAN, the location of an obstacle is defined by a sequence of node points used to represent line segments. These lines cross a grid linkage between two nodes and interrupt the transmission of energy density across that grid linkage.

Representing a dynamic device with a line may appear over-simplistic until one considers the spatial and temporal scales across which SWAN operates. Inherent issues with the representation exist, where a line cannot effectively extract power from a directional sea. To complicate matters further, it is difficult to find a universal representation for a device given the ever growing number of device architectures. En masse, devices rarely resemble lines making this geometric simplification not only visually inaccurate, but also a source of trouble when calculating a transmission coefficient. The reference WEC in this work has a well-defined inlet and outlet but devices which extract power from omnidirectional seas, such as the point absorber presented in Figure 1 are more difficult to represent.

Additionally, the WEC device's physical width is used to calculate the width of the incoming wave front as presented in Eq. (14). Following existing SNL-SWAN convention, the entries in an input power matrix are normalized by a capture width. Using a device's physical width in the calculation of RCW is a creative choice and one that has been widely used in the WEC industry based on the perception that a WEC only interacts with the incident wave front that it physically touches. However, this notion is is problematic as described by Falnes and Hals:

> "Quite often, results have, traditionally, been expressed by quantities as 'absorption width' and 'capture width', which have dimension length (SI unit

> metre), or by dimensionless quantities, such as ‘capture width ratio’ and ‘(hydrodynamic) efficiency’… These technical terms focus on one horizontal dimension (in the direction of the incident wavefront). However, a WEC has two horizontal dimensions, in addition to a vertical one. [114]”

Devices interact with the oscillations of the surroundings waves over these other dimensions as well. In fact, when the diffracted wave field is considered, the device is known to perturb the surrounding wave field over a broader domain than its own physical dimensions. Previous literature has indicated certain device architectures can absorb more wave power than is available directly incident to the width of the device. Early experimentation with point absorbers demonstrated devices absorbing more energy than was directly incident to the device [115].

To summarize the issue, the power incident to the device’s primary interface is underestimated as a result of the width chosen with which to normalize the device’s power production. As such, when the energy density is gathered at a node point (or lumped) it is gathered from a surrounding region that is no larger than the width of the grid spacing it intersects. When the obstacle then removes energy during the transport from one node to the next, the power in the incident sea is integrated over the width of the physical device. The proposed correction is that the width needs to represent the effective width of the device, or the device needs to be represented using another dimension, as will be discussed in Chapter 6.

The theoretical issues presented extend into the work presented in this thesis as well. The device’s representation has an influence on how the waver power transport across the directional domain is modified. SWAN isolates the inlet wave spectrum to the power crossing the line based on projections of the energy transport. When the device is simulated in the time domain, even though the incident wave spectrum is propagated towards the device from a principal wave direction. The incident wave forcing is integrated across the device’s three-dimensional mesh allowing the device to be excited not only across the face directly incident to the wave, but also along its other edges, which is partially responsible for the difference in power absorption when the device is represented with *obstacle case five* versus *obstacle case six*.

5.1.2 Representation of Radiation

Radiation can theoretically be distributed across either side of the line representing the device in SWAN given more power is not taken out of the system than is incident. If energy is to be conserved within the computational domain, the following condition must be true:

$$E_r + E_t + E_a = E_{inc} \quad \textbf{(35)}$$

where E_r is the energy radiated by the device, E_t is the energy transmitted past the device, E_a is the energy absorbed by the device and E_{inc} is the energy incident to the device. From the power balance presented in Section 3.5, one can determine the time averaged power absorbed, radiated and incident to the device. When the device is represented as both a source and sink the representation of energy transmitted (leaving through the lee of the device) and energy reflected (leaving through the front of the device), are linked through Eq. (30). In addition to the overarching energy conservation condition, the user must also comply to Eq. (32) to ensure that within the finite difference scheme used in SWAN, more energy is also not taken out of the system. With the present uncertainty in device capture width this condition could not be implemented without violating Eq. (32) however modelling another device, or increasing the device's width in SWAN can make this representation a feasible alternative.

The inconsistency in representing a device as a line in SWAN is already apparent when considering the incident loading alone. The magnitude of this problem is amplified when considering the radiated wave. A moving device will radiate waves in all directions. The only directional data provided by the time domain simulator is the magnitude of forces exerted in each DOF which does not provide sufficient information to discern the direction in which the radiated power is being transferred and the user has no knowledge of what the radiation pattern would look like. Even with this information available, within SWAN, the user can only propagate energy directly in front of or behind the device as there are only two sides of a line.

The right hand plot in Figure 69 demonstrates how both the incident and radiated power exceed the power within the incident wave spectrum at frequencies near the spectral peak. For the simulations pertaining to the reference WEC, the power absorbed

by the device was calculated by taking the difference of the incident and radiated power, as presented by the blue line in the plot on the left. Even though the author has created a method with which the device can be characterized as both a source and a sink, this technique is rendered moot by the fact that power must be radiated to the lee in order to prevent the energy extraction in spectral bins to avoid saturating. Once saturated, the energy extracted must be redistributed following the method of Section 3.7.1.3 which adds another layer of creative modeling.

Theoretically, if a capture width greater than that of the device's physical width was selected, the incident wave spectrum would be scaled up allowing for more power to be intercepted. To the author's knowledge, there has been no method established to date which can be used to determine the width of the wave front from which the device intercepts power.

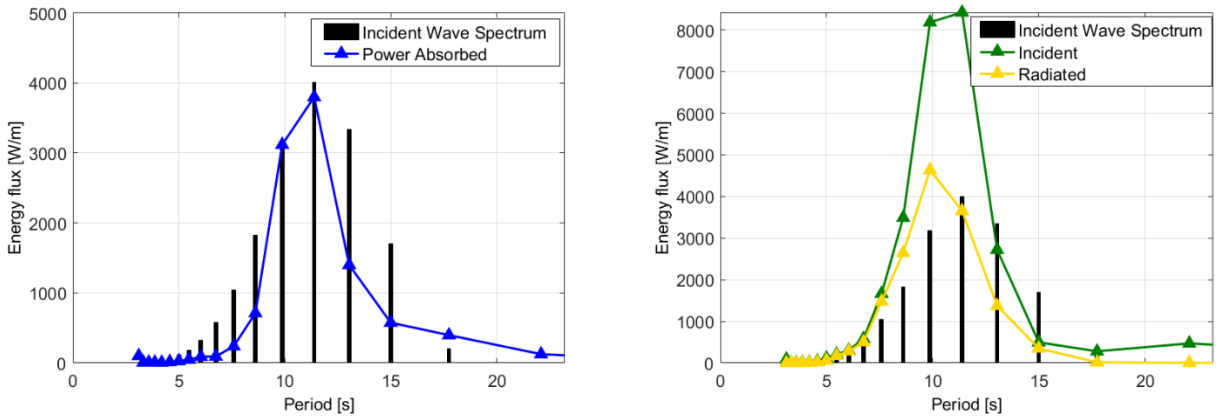

Figure 69: The incident wave spectrum and the power absorbed by the Reference WEC in an Hs = 1.75 m and Tp = 11.6 s sea state. On the left, the power absorbed by the device is superposed on the incident wave spectrum. On the right, the incident power and the radiated power are superposed on the incident wave spectrum.

The user is warned that even in the case where energy is conserved and the coefficients input by the user comply with Eq. (32), limitations still exist in the representation of radiation. Radiation is being represented as a source term which is added back into the computation domain after the initial finite differencing. Representing a device as a source and a sink allows for potential constructive interaction to occur between devices however the present representation of radiation needs further refinement in future work.

First of all, power is only being radiated in two directions largely due to the geometric constraints of representing a device with a line. Simulations conducted in BEM models

such as WAMIT indicate devices radiate waves in many directions [89] with exact radiation patterns depending on the device geometry.

Even though power can only be radiated forward and backward, because the far field transmission coefficient K_r is applied uniformly across each directional bin, a circular radiation can be observed for the OWC device within SNL-SWAN.

Secondly, the SNL-SWAN source code modifications implemented by the author only allow for a device's radiation pattern to be tuned with a single parameter, γ_{rad}. Radiation patterns can be determined from WAMIT by finding the radiated potential at various field points for each DOF and each frequency. It is difficult to represent this information in a concise manner. Secondly, because WAMIT is run with regular waves, an impulse response function would be required to recreate the time series of radiated waves for each device with SNL-SWAN negating any benefit in having a fast, phase-averaged model. Potential alternative representations are presented in Chapter 6.

Thirdly, radiation is essentially implemented as a reflection coefficient where a user-specified percentage of the incident wave is reflected back towards the incident wave. This approach is consistent with the way energy transmission is represented in SWAN, however not necessarily consistent with the wave radiated power is transferred physically. As a result, the shape of the radiated wave field will be a scaled representation of the incident wave field.

Finally, the inclusion of a radiated wave field will skew the selection of transmission coefficients as the model iterates upon a solution. SWAN employs a Gauss-Seidel scheme [84] to propagate energy density across the computation domain. After energy density is propagated from the boundaries, source and sink terms are applied to the model's computations. SWAN iterates until it can converge on a solution that falls within the tolerance set by the user in the control file. The transmission coefficient is dependent on the H_s and T_p of the energy density spectrum at the node before the obstacle. As power is radiated from the obstacle, the bulk parameters at the device's incident node will increase, as seen in Figure 70. Higher values of power will be referenced within the device's power matrices leading to greater captured power being reported. Even though it is physically possible that a device can work off its own radiated wave, there is no way to

validate whether or not the values generated will be representative of a device's performance at sea.

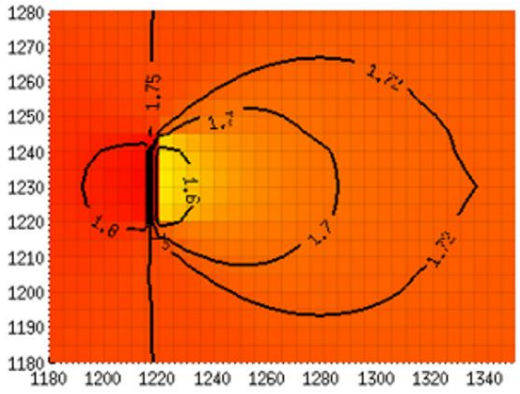

Figure 70: Radiation represented within SWAN

The time domain simulation results do in fact capture instances where a radiated wave completes work back on the device. These instances contribute to the calculation of net energy taken or delivered to the surrounding waves.

In the context of SWAN, the problem lies in that the radiated waves are changing the description of the incident wave condition. As a result, SWAN is employing a look up procedure to a condition the device did not encounter within the time domain simulator.

Once again, the reader is reminded ProteusDS was developed to analyze a submerged device's dynamics, not the device's impact on the surrounding wave field. In order to minimize the computational cost of the model, radiated waves are not actuated by the device's motions. As a result, a device will not be able to generate power from its own radiated wave potentially underpredicting both the power generated by the device and any additional forces that may arise. The lack of a radiated wave will further hinder the representation of drag power. Since a radiated was is not being generated within the time domain simulator, the water velocity around the device does not capture the radiated wave.

5.2 Approximations in the time domain model

The accuracy of the results from SNL-SWAN are limited by the accuracy of its input parameters. The energy balance method proposed in Section 3.4 relies heavily on the precise calculation of the velocity and forces drawn from the time domain model. It should be noted however, that the time domain model was created with the intent of modelling a device's hydrodynamic response to incident wave conditions, not the device's effect on the fluid domain. As such, certain parameters required for the energy balance are either not explicitly calculated or not recorded in ProteusDS. In either case, valuable information is missing.

First, inaccuracies lie within the representation of the device's power associated with drag. The drag force is calculated by ProteusDS using a Morrison based approach similar to the one presented in Equation 11. This calculation employs the device's relative velocity at each mesh panel, transforms and sums these forces so they can be represented at the device's center of mass. Similarly, the simulator outputs the device's velocity at the center of mass. A challenge arises in calculating the power transfer associated with drag because the velocity of the water at each panel location is required to calculate the power transfer occurring through each panel interaction – this data is not available. To alleviate this issue, an available representative value of the water velocity, that at the WEC device's center of gravity, is used to calculate the energy transferred from or to the fluid domain. Secondly, the device dynamics in ProteusDS are calculated based solely on the incident wave spectrum, as previously discussed in Section 5.1.2. The model calculates the radiated force exerted by the device on the surrounding fluid according to motions induced by it radiating waves. The simulator however, does not actually propagate waves back into the fluid domain.

5.3 Linearity Assumptions

Linear potential flow theory is a computationally efficient method to solve flow problems and has become common practise in fluid related fields studying airfoils, groundwater and water waves. Although linearity is a convenient simplification, it can lead to erroneous results. This section will state the linearity assumption employed in the RCW matrix generation matrix and will touch on the assumptions employed in the

Cummin's equation and linear potential flow adding further uncertainty to the methodology presented.

In generating the RCW matrix, an FFT is conducted on the time series signals of a force and velocity. First and foremost, by taking the ratio of frequency resolved device power absorption and the power in the waves, one assumes the device will absorb power at the same frequency at which power entered the device. Within the OWC system, nonlinear power contributions exist including: drag (viscous, turbulence and vortex transport losses), mooring dynamics and air compression within the OWC chamber. It is possible that through non-linear behaviour, power that may have been intercepted by the device through one frequency bin, may manifest itself in another. This shifting of energy between frequency bins could be responsible for certain bins within the RCW matrix having values greater than one. In future work, a method must be developed to be able to track how power moves across the frequency domain such that energy will not have to be distributed to neighbouring bins.

Some assumptions made within this thesis and the larger body of knowledge pertaining to the wave energy field are presented. Addressing these issues is out of the scope of this thesis however the reader is reminded of these practises given these are potential sources of error in the methodology presented.

Chapter 6

Conclusions and Future Work

An objective of the current work was to measure the uncertainty in conducting annual energy production and far field impact studies of WEC arrays by examining differences in SNL-SWAN predictions when using different WEC representations. This work also demonstrates the utility and limitations of the WEC representations when using the 'obstacle' feature in SWAN as a framework. Finally, the sensitivity and uncertainty associated with the proposed WEC representations was analyzed across a large computational domain. This Chapter seeks to summarize the major developments and findings of the work presented in Chapters 3 through 5 and presents recommendations for future work in the field of modelling WEC arrays in a spectral wave model.

6.1 Conclusions

The purpose of this section is twofold. First, a summary of the technical developments presented in this thesis can be found by Section 6.1.1. Section 6.1.2 states a list of main findings that came to light after applying obstacle cases one, five and six are applied in a numerical test basin and in a field case.

6.1.1 Technical Developments

The obstacle command in SWAN was originally designed to represent breakwaters as straight line barriers that could be positioned along gridlines within the modeled domain. In SWAN, the location of an obstacle is defined by a sequence of node points used to represent line segments. Obstacles interrupt the propagation of the waves from one grid point to the next [101]. This interruption can be in the form of wave reflection, wave absorption or even a wave source, such as the injection of energy at a new frequency when a device radiates waves. In SWAN's representation of static obstacles, the transfer of energy through an obstacle is defined by the user with a transmission and or reflection coefficient. A transmission coefficient extracts a ratio of incident wave energy in space, as seen in Eq. (10). SNL-SWAN currently characterizes a WEC using either a power matrix or an RCW curve from which it calculates a transmission coefficient using Eq. (14). SNL's representation uses power performance information supplied by developers in order to derive a transmission coefficient. Derivation of a transmission coefficient from this data alone assumes that any effect the WEC has on the surrounding sea is represented solely by the captured power. In short, by using these pre-existing parameterizations perfect conversion from incident to captured power is assumed, and the energy removed from the incident waves is likely to be underestimated.

To better represent a device's hydrodynamic interaction with the surrounding fluid domain, the intercepted power was calculated by conducting a power balance on the power entering and leaving the device. In order to calculate the incident, radiated and by extension the absorbed power, force and velocity time series from a high fidelity 6 DOF hydrodynamic simulator were used. All pre-processing simulations were conducted with directionally spread waves with a primary wave direction of zero degrees. The power balance was deemed to be an effective approach as the difference between the right and

left hand sides of Eq. (26) was a root mean squared error of 4% across all 66 sea states simulated in ProteusDS.

As a case study, a BBDB OWC was chosen as it includes as many of the complicating dynamic factors as possible – moorings, surface piercing, and a full 6 DOF range of motion. *Obstacle cases five* and *six* were developed in an effort to include a device's hydrodynamic interaction with the surrounding fluid domain within a timeframe compatible with that of SWAN.

Obstacle case five bilinearly interpolates a transmission coefficient from an intercepted power matrix, uniformly reducing the variance in each frequency bin of the incident spectrum. The intercepted power is used to calculate the device's impact on the surrounding fluid domain while the captured power is used to determine the power produced by the device.

Obstacle case six applies a sea state and frequency dependent transmission coefficient to the incident variance spectrum. This transmission coefficient is calculated from the RCW Matrix. As in *obstacle case five,* the intercepted power is used to calculate the device's impact on the surrounding fluid domain while the captured power is used to determine the power produced by the device.

Without validation it is difficult to objectively state which of the two propose representations is the most accurate, however *obstacle case six* is a higher fidelity representation of a wave energy converter.

6.1.2 Main Findings

The proposed meta-models were tested in a variety of conditions ranging from synthetic controlled numerical test tanks to an actual field test case.

Single Device

Based on the results from flat domain simulations in Chapter 4, the incident spectrum is most affected by the device representation in the first 50 metres behind a device. Once the incident spectrum propagates to 200 metres behind the device, regardless of the representation, the device has recovered to its original spectral shape. With respect to the H_s in the device's lee, the greatest reduction is observed when the device's intercepted power is described with a constant transmission coefficient. Even though *obstacle case*

five removes the most power out of the incident sea, this representation also causes the surrounding wave field to recover the most quickly. A device may generate the greatest reduction in H_s directly in the lee of the device, however the wave field to the right and left of the device is also reduced roughly ten device widths to either side of the device.

Even though *obstacle case five* and *six* should theoretically remove the same amount of power, due to differences in the way the power in the waves is calculated, more explicitly described in Section 4.1.2, *obstacle case six* reduces the H_s in the lee of the device less than *obstacle case five*.

Devices in Series

The incident H_s to a device is reduced with every additional preceding device. Because *obstacle case five* removes the most power from the incident sea, it reduces the H_s to the incident device most of the three representations analyzed. The maximum decrease in H_s does not change drastically with each subsequent device however the lateral extent to which the H_s field around the device is modified increases, as seen in Figure 44. With respect to power production, the three representations seem to reach an asymptotic power value after a certain number of devices in series. When *obstacle case one* is employed, the power captured by the second device is reduced by 1.54% when compared to the first, while the power captured by the fifth device is only reduced by 2.30% at the first device. When *obstacle case five* is employed, the power captured by the second and fifth device is reduced by 5.56% and 6.00% respectively. Finally, when *obstacle case six* is employed, the power captured by the second and fifth device is reduced by 2.30% and 2.78% respectively.

Devices in an Array

When multiple rows of devices are placed in an array, the far field impact of these devices is exacerbated. The greatest reduction in H_s behind devices in the array is observed in the lee of the array and is reduced in amplitude as the waves propagate closer to shore. At the shoreline, *obstacle case one* reduced the H_s by 0.44% on average, with a maximum reduction of 0.57% at over the course of the year. *Obstacle case five* reduces the H_s by 1.28% on average and a maximum reduction of 1.80%. Finally, *obstacle case six* reduces the H_s by 0.84% on average and incurs a maximum reduction of 0.72% in H_s. By the time the wave spectrum reaches the shoreline, the WEC representation employed

(*obstacle case one, five,* or *six*) has little impact on the far field analysis. Similarly low differences in AEP are observed when obstacles five and six are compared to obstacle case one. Greater differences in array performance come to light in higher energy seas where greater variations in an individual device's power production can be observed depending on the WEC representation. When the *obstacle case five* device representation is employed individual devices will produce as much as 18% more power, or 14% less power than when represented with *obstacle case one*. *Obstacle case six* can decrease power by 18.5% for a particular device while increasing the power produced by another device by 15.4%. Drastic changes in power production are observed as the incident sea condition is more variable across the array.

In conclusion, the device representation has the greatest impact on the local surrounding wave field. Once the array's power production has been aggregated over time, or far field impact has been aggregated over a larger spatial extent, little difference can be observed between the three representations, indicating SWAN is not very sensitive to the way the device is being represented.

6.2 Future Work

Recommendations for future work to further the field of accurately representing a WEC's operation in a spectral wave model are largely related to the way in which the device is represented and the present work's lack of validation.

6.2.1 Device Representation

The approach used with which to model WECs in this work is hindered by the device's representation as a line connecting two grid nodes. As such, the author recommends that future iterations of such work represent the device as a node with a modified spectrum input at the node when SWAN is iterating towards a solution. The proposed approach is analogous to the Kochin function and wave generating circle recommended by Babarit et al. [79]. One of the drawbacks of the Kochin function is that it does not account for viscous losses as its water surface elevation is obtained from a BEM linear potential flow model. As such, the device's velocity time series output from ProteusDS could be

decomposed into its frequency components. This velocity will be affected by the viscous forces acting on the body over the course of the simulation. The non-dimensionalized radiation water surface elevation component output from a BEM model can be scaled by the body's velocity for a particular frequency allowing the user to determine the body's water surface elevation due to radiation at a field point. This water surface profile can be convolved to find the water surface elevation resulting from the device's operation in a particular sea state. As such, the device's power performance can be determined based on bulk parameters from the incident spectrum while far field impact could be realized by implementing the modified device spectrum at the node representing the device. Ideally, SWAN and ProteusDS could be coupled, allowing for the exact spectrum from SWAN to be propagated towards the device in the time domain model. However, given the inconsistency in evaluation times between ProteusDS and SWAN some kind of look-up procedure may be required to reduce total simulation execution times. This approach still needs to be refined and its impact of SWAN's convergence is yet to be determined however, it does pose as a potential solution to the issues that came to light during this thesis.

This representation would eliminate the need to define a capture width, by extension eliminating the need to rebin power absorbed by the device, as was required for certain RCW curves in Section 3.7.1.3. Furthermore, this representation would alleviate concerns regarding imprecise representations of the device's directional impact on the incident wave spectrum. This representation would also be suitable for implementation within an unstructured grid which would eliminate the need for nesting and reduce the total computational time of field simulations.

6.2.2 Validation

In order to most accurately validate *obstacle five* and *six*'s accuracy, a field case in which an array of devices was deployed would need to be conducted. As the WEC industry has not deployed many WEC arrays in the open ocean to date, and information pertaining to the perturbed wave field has not been collected, validating the new modules is a challenge. An alternative to field data is validating against tank test data, as has been done in the past.

Experimental tests have previously been conducted to validate SNL-SWAN [28], [32], [104]. Experimental tests were conducted with an array of five 1:33 scale Columbia Power Technology's Manta 3.1 WECs moored in the Oregon State University's Hinsdale Tsunami Wave Basin [28]. Trials were conducted with single devices and arrays of three and five devices in both regular and irregular waves. The frequency dependent switches within SNL-SWAN (*obstacle cases three* and *four*) performed better than those that employed a bulk parameter value (*obstacle cases one* and *two*). The author could not validate the new obstacle cases because there was not enough information available about the Manta 3.1 to generate a high-fidelity time domain model of the device.

Experimental measurements have been conducted as parts of larger research programs. At the DanWEC test site near the Port of Hanstholm, Denmark, the Wavestar WEC composed of a larger number of floating bodies attached to a structure, was deployed to verify the power production curves generated by the company and the device's reliability in storms [116]. Additionally, the UK Supergen Marine and EU Hydralab III progrmmes have conducted experimental tests on an array of five OWCs. Six wave probes were placed in and around the array to record the wave disturbance from the array [117]. These experiments were conducted in regular waves which are difficult to accurately recreate in a spectral action density model. Studies limited to a small number of devices also exist [61], [118],[16] however the WEC response, power output and wave field modifications are not publicly available.

Two larger experimental setups with arrays have been conducted. Stratigaki et al. conducted experiments at the Danish Hydraulic Institute's Shallow Water Wave Basin in Hørsholm, Denmark. Arrays of five, ten and 25 heaving point absorbers were tested in various geometric layouts and wave conditions. Wave gauges were placed in and around the array to record the wave field modifications [119]. Furthermore, under the PerAWaT project, Child and Weywada compared experimental results from three configurations of a 1:80 scale 22 WEC array to results from the numerical model WaveFarmer. The data from this study is not publicly available. In addition, the separating distance within the array was less than five device widths, as a result, phase-dependent interactions dominate, which would not be accurately captured within a spectral action density model like SNL-SWAN [63].

Even though a number of array studies have been conducted to date, few if any are publicly available creating a barrier in conducting a validation of the proposed methodologies. Ideally, a scaled WEC array can be experimentally tested in a large wave tank with multi-directional spectra propagated towards the WECs. Wave gauges can be placed within and behind the WEC array to determine the impact the waves have on the surrounding wave field. Spectra output from the corresponding SWAN simulations could be compared at the wave gauge locations determining which of the obstacle cases proposed best represents the array's far field impact. Tank trials analyzing far field impact however, are limited. In order to capture the various wave components in a spectrum, waves must propagate for a long time which may result in wave reflections near the tank edges so the most accurate measures of far field impact will be apparent when WEC arrays are deployed at sea.

Bibliography

[1] S. De Chowdhury, J. Nader, A. M. Sanchez, A. Fleming, and B. Winship, “A review of hydrodynamic investigations into arrays of ocean wave energy converters.”

[2] R. Waters, *Energy from Ocean Waves*. 2008.

[3] G. Reikard, B. Robertson, and J. R. Bidlot, “Combining wave energy with wind and solar: Short-term forecasting,” *Renew. Energy*, vol. 81, pp. 442–456, 2015.

[4] L. Holthuijsen, *Waves in Oceanic and Coastal Waters*. Delft: Cambridge University Press, 2007.

[5] K. Gunn and C. Stock-williams, “Quantifying the global wave power resource,” *Renew. Energy*, vol. 44, pp. 296–304, 2012.

[6] P. Mccullen, A. Cle, A. Fiorentino, F. Gardner, K. Hammarlund, G. Lemonis, T. Lewis, K. Nielsen, H. Christian, and T. Thorpe, “Wave energy in Europe : current status and perspectives,” vol. 6, pp. 405–431, 2002.

[7] F. Marvin, “Wave Motor,” 1502511 A, 1922.

[8] B. Czech and P. Bauer, “Wave Energy Converter Concepts: Design Challenges and Classification,” no. June, pp. 4–16, 2012.

[9] F. M. Nelson, “Wave Motor,” 1018678 A, 1912.

[10] B. Drew, A. R. Plummer, and M. N. Sahinkaya, “A review of wave energy converter technology,” vol. 223, pp. 887–902, 2009.

[11] A. A. E. Price, “New Perspectives on Wave Energy Converter Control,” no. March, pp. 1--319, 2009.

[12] A. Babarit, J. Hals, M. J. Muliawan, A. Kurniawan, T. Moan, and J. Krokstad, “Numerical benchmarking study of a selection of wave energy converters,” *Renew. Energy*, vol. 41, pp. 44–63, 2012.

[13] K. Budal, “Theory for the absorption of wave power by a system of interacting bodies,” *J. Sh. Res.*, vol. 21, 1977.

[14] P. Balitsky, “Modelling Controlled Arrays of Wave Energy Converters,” no. June, p. 110, 2013.

[15] D. L. L. Millar, H. C. M. C. M. Smith, and D. E. E. Reeve, “Modelling analysis of the sensitivity of shoreline change to a wave farm,” *Ocean Eng.*, vol. 34, no. 5–6,

pp. 884–901, 2007.

[16] A. Alexandre, T. Stallard, and P. K. Stansby, “Transformation of Wave Spectra across a Line of Wave Devices,” *Power*, no. Proceedings of the 8th European Wave and Tidal Energy Conference, Uppsala, Sweden, pp. 1–9, 2009.

[17] V. Venugopal and G. H. Smith, “Wave climate investigation for an array of wave power devices.”

[18] A. Combourieu, M. Lawson, A. Babarit, K. Ruehl, A. Roy, R. Costello, P. L. Weywada, and H. Bailey, “WEC 3 : Wave Energy Converter Code Comparison Project,” pp. 1–10, 2015.

[19] R. S. Nicoll, C. F. Wood, and A. R. Roy, “Comparison of Physical Model Tests With a Time Domain Simulation Model of a Wave Energy Converter,” in *ASME 2012 31st International Conference on Ocean, Offshore and Arctic Engineering.*, 2012.

[20] H. Bailey, B. Robertson, and B. J. Buckham, “Wave-to-Wire Simulation of a Floating Oscillating Water Column Wave Energy Converter.” 2016.

[21] S. J. Beatty, M. Hall, B. J. Buckham, P. Wild, and B. Bocking, “Experimental and numerical comparisons of self-reacting point absorber wave energy converters in regular waves,” *Ocean Eng.*, vol. 104, pp. 370–386, 2015.

[22] M. Pe, G. Giorgi, and J. V Ringwood, “A Review of Non-Linear Approaches for Wave Energy Converter Modelling,” no. 1, pp. 1–10, 2015.

[23] M. Pe, J. Gilloteaux, and J. V Ringwood, “Nonlinear Froude-Krylov force modelling for two heaving wave energy point absorbers,” pp. 1–10, 2015.

[24] B. F. M. Child and V. Venugopal, “Optimal configurations of wave energy device arrays,” *Ocean Eng.*, vol. 37, no. 16, pp. 1402–1417, 2010.

[25] R. Carballo and G. Iglesias, “Wave farm impact based on realistic wave-WEC interaction,” *Energy*, vol. 51, pp. 216–229, 2013.

[26] J. Abanades, D. Greaves, and G. Iglesias, “Wave farm impact on the beach profile: A case study,” *Coast. Eng.*, vol. 86, pp. 36–44, 2014.

[27] A. Palha, L. Mendes, C. J. Fortes, A. Brito-Melo, and A. Sarmento, “The impact of wave energy farms in the shoreline wave climate: Portuguese pilot zone case study using Pelamis energy wave devices,” *Renew. Energy*, vol. 35, no. 1, pp. 62–77,

2010.

[28] K. Ruehl, A. Porter, A. Posner, and J. Roberts, “Development of SNL-SWAN , a Validated Wave Energy Converter Array Modeling Tool,” *Proc. 10th Eur. Wave Tidal Energy Conf., Aalborg, Denmark,* 2013.

[29] G. Iglesias and M. Veigas, “Wave farm impact and wave-WEC interaction : a sensitivity analysis,” *Proc. 10th Eur. Wave Tidal Energy Conf., Aalborg, Denmark,* 2013.

[30] C. Beels, P. Troch, G. De Backer, M. Vantorre, and J. De Rouck, “Numerical implementation and sensitivity analysis of a wave energy converter in a time-dependent mild-slope equation model,” *Coast. Eng.*, vol. 57, no. 5, pp. 471–492, 2010.

[31] K. E. Silverthorne and M. Folley, “A New Numerical Representation of Wave Energy Converters in a Spectral Wave Model.”

[32] A. Porter, K. Ruehl, and C. Chartrand, “Further Development of Snl - Swan , a Validated Wave Energy Converter Array Modeling Tool,” *2nd Mar. Energy Technol. Symp.*, pp. 1–9, 2014.

[33] IEC, “TC114: Marine energy - Wave, tidal and other water current converters - Part 100: Electricity producing wave energy converters - Power performance assessment,” IEC/TS 62600-100 Ed. 1.0, 2012.

[34] P. Ricci, J. Saulnier, and A. F. D. O. Falcão, “Point-absorber arrays : a configuration study off the Portuguese West-Coast.”

[35] H. C. Soerensen, “Wave Dragon - from the 20 kW to the 7 MW Prototype,” 2006.

[36] US Department of Energy, “Marine and Hydrokinetic Technology Database,” 2015. [Online]. Available: http://en.openei.org/wiki/Marine_and_Hydrokinetic_Technology_Glossary. [Accessed: 26-May-2016].

[37] D. Bull, C. Smith, D. S. Jenne, P. Jacob, A. Copping, S. Willits, A. Fontaine, D. Brefort, G. Copeland, M. Gordon, and R. Jepsen, “Reference Model 6 (RM6): Oscillating Wave Energy Converter,” vol. 6, no. September, 2014.

[38] U.S DOE, “Reference Model Project (RMP),” 2014. .

[39] D. Bull and P. Jacob, “Methodology for creating nonaxisymmetric WECs to screen

mooring designs using a Morison Equation approach," in *Oceans. IEEE.*, 2012.

[40] J. C. C. Henriques, M. F. P. Lopes, R. P. F. Gomes, L. M. C. Gato, and a. F. O. Falcão, "On the annual wave energy absorption by two-body heaving WECs with latching control," *Renew. Energy*, vol. 45, pp. 31–40, 2012.

[41] US Department of Energy, "Adjustable Speed Drive Part-Load Efficiency," 2012.

[42] B. Robertson, C. E. Hiles, E. Luczko, and B. J. Buckham, "Quantifying the Wave Power and Wave Energy Converter Array Production Potential," *Int. J. Mar. Energy*, vol. 1, 2016.

[43] M. Folley, A. Babarit, B. F. M. Child, D. Forehand, L. O'Boyle, K. Silverthorne, J. Spinneken, V. Stratigaki, and P. Troch, "A Review of Numerical Modelling of Wave Energy Converter Arrays," in *ASME 2012 31st International Conference on Ocean, Offshore and Arctic Engineering*, 2012, pp. 1–12.

[44] WAMIT Inc., "WAMIT User Manual - Version 7.1," 2015.

[45] J. Falnes, *Ocean Waves and Oscillating Systems: Linear Interactions Including Wave Energy Extraction*. Cambridge: Cambridge University Press, 2004.

[46] C. Lee and F. Nielsen, "Analysis of oscillating-water-column device using a panel method," *International Workshop on Water Wave and Floating …*. 1996.

[47] C. H. Lee, J. S. Letcher, R. G. Mark, J. N. Newman, D. M. Shook, and E. Stanley, "Integration of geometry definition and wave analysis software," in *21st International Conference on Offshore Mechanics and Arctic Engineering*, 2002, pp. 721–733.

[48] P. B. Garcia-Rosa, R. Costello, F. Dias, and J. V Ringwood, "Hydrodynamic Modelling Competition - Overview and Approaches," in *ASME 2015 34th International Conference on Ocean, Offshore and Arctic Engineering*, 2015.

[49] B. Robertson, H. Bailey, D. Clancy, J. Ortiz, and B. Buckham, "Influence of wave resource assessment methodology on wave energy production estimates," *Renew. Energy*, vol. 86, pp. 1145–1160, 2016.

[50] Dynamic Systems Analysis, "ProteusDS 2015 Manual," Victoria, BC, 2015.

[51] B. J. Buckham, "Dynamics modelling of low-tension tethers for submerged remotely operated vehicles," 2003.

[52] Mathworks, "Simulation and Model-Based Design," 2016. [Online]. Available:

http://www.mathworks.com/products/simulink/. [Accessed: 16-May-2016].

[53] C. Josset and A. H. Clement, “A time-domain numerical simulator for oscillating water column wave power plants,” *Renew. Energy*, vol. 32, no. 8, pp. 1379–1402, 2007.

[54] W. E. Cummins, “The Impulse Response Function and Ship Motions,” 1962.

[55] B. R. D. Robertson, C. E. Hiles, and B. J. Buckham, “Characterizing the near shore wave energy resource on the west coast of Vancouver Island , Canada,” *Renew. Energy*, vol. 71, pp. 665–678, 2014.

[56] W. J. Pierson and L. Moskowitz, “A proposed spectral form for fully developed wind seas based on the similarity theory of S. A. Kitaigorodoski,” 1963.

[57] DNV, *Recommended practice DNV-RP-C205 environmental conditions and environmental loads*. 2010.

[58] DNV, “Recommended Practice. DNV-RP-H103. Modelling and Analysis of Marine Operations,” 2011.

[59] C. E. Hiles, B. J. Buckham, P. Wild, and B. Robertson, “Wave energy resources near Hot Springs Cove, Canada,” *Renew. Energy*, vol. 71, pp. 598–608, 2014.

[60] H. a. Wolgamot, P. H. Taylor, and R. Eatock Taylor, “The interaction factor and directionality in wave energy arrays,” *Ocean Eng.*, vol. 47, pp. 65–73, 2012.

[61] S. D. Weller, T. J. Stallard, and P. K. Stansby, “Experimental measurements of irregular wave interaction factors in closely spaced arrays,” *IET Renew. Power Gener.*, vol. 4, no. 6, p. 628, 2010.

[62] V. Stratigaki, *Experimental study and numerical modelling of intra-array interactions and extra-array effects of wave energy converter arrays*. 2014.

[63] B. F. M. Child and P. L. Weywada, “Verification and validation of a wave farm planning tool,” *Proc. 10th Eur. Wave Tidal Energy Conf., Aalborg, Denmark*, 2013.

[64] B. Borgarino, a. Babarit, and P. Ferrant, “Impact of wave interactions effects on energy absorption in large arrays of wave energy converters,” *Ocean Eng.*, vol. 41, pp. 79–88, 2012.

[65] K. Ruehl, C. Chartrand, and A. K. Porter, “SNL-SWAN User’s Manual,” 2014.

[66] N. Booij, R. C. Ris, and L. H. Holthuijsen, “A third-generation wave model for

coastal regions: 1. Model description and validation," *J. Geophys. Res.*, vol. 104, no. C4, pp. 7649–7666, 1999.

[67] A. Sharifahmadian, *Numerical Models for Submerged Breakwaters: Coastal Hydrodynamics and Morphodynamics*. Butterworth-Heinemann, 2015.

[68] K. D'Angremond, J. Van Der Meer, and R. De Jong, "Chapter 187. Wave transmission at low-crested structures," *Coast. Eng.*, pp. 2418–2427, 1996.

[69] Y. Goda, H. Takeda, and Y. Moriya, "Laboratory investigation of wave transmission over breakwaters," Yokosuka-City, 1967.

[70] P. A. Madsen, R. Murray, and O. R. Sorensen, "A new form of the Boussinesq equation with improved linear dispersion characteristics," *Coast. Eng.*, vol. 15, pp. 371–388, 1991.

[71] J. T. Kirby, "Boussinesq models and applications to nearshore wave propagation, surf zone processes and wave-induced currents," *Elsevier Oceanography Series*, vol. 67, no. C. pp. 1–41, 2003.

[72] N. Violante-Carvalho, R. B. Paes-Leme, D. A. Accetta, and F. Ostritz, "Diffraction and reflection of irregular waves in a harbor employing a spectral model," *An. Acad. Bras. Cienc.*, vol. 81, no. 4, pp. 837–848, 2009.

[73] Danish Hydraulic Institute, "Mike 21 Wave Modelling," 2015.

[74] L. Hamm, P. A. Madsen, and D. H. Peregrine, "Wave transformation in the nearshore zone: A review," *Coast. Eng.*, vol. 21, no. 1–3, pp. 5–39, 1993.

[75] L. Cavaleri, J. H. G. M. Alves, F. Ardhuin, A. Babanin, M. Banner, K. Belibassakis, M. Benoit, M. Donelan, J. Groeneweg, T. H. C. Herbers, P. Hwang, P. A. E. M. Janssen, T. Janssen, I. V. Lavrenov, R. Magne, J. Monbaliu, M. Onorato, V. Polnikov, D. Resio, W. E. Rogers, A. Sheremet, J. McKee Smith, H. L. Tolman, G. van Vledder, J. Wolf, and I. Young, "Wave modelling - The state of the art," *Prog. Oceanogr.*, vol. 75, no. 4, pp. 603–674, 2007.

[76] M. W. D. A.C. Radder, "Canonical equations for almost periodic, wekaly nonlinear gravity waves," *Wave Motion*, vol. 7, pp. 473–485, 1985.

[77] C. Beels, P. Troch, K. De Visch, J. P. Kofoed, and G. De Backer, "Application of the time-dependent mild-slope equations for the simulation of wake effects in the lee of a farm of Wave Dragon wave energy converters," *Renew. Energy*, vol. 35,

no. 8, pp. 1644–1661, 2010.

[78] J. C. W. Berkhoff, “Computation of combined refraction-diffraction,” *13th Int. Conf. Coast. Eng.*, pp. 471–490, 1972.

[79] A. Babarit, M. Folley, F. Charrayre, C. Peyrard, and M. Benoit, “On the modelling of WECs in wave models using far field coefficients,” *Eur. Wave Tidal Energy Conf. EWTEC*, pp. 1--9, 2013.

[80] National Academies Press, *Twenty-Second Symposium on Naval Hydrodynamics*. 2000.

[81] Research and Studies Directorate of the French Electricity Board, “ARTEMIS User Manual,” 2014.

[82] Danish Hydraulic Institute, “MIKE 21 EMS Elliptic Mild-Slope Wave Module,” 2007.

[83] N. Booji and L. Holthuijsen, “Propagation of ocean waves in discrete spectral wave models,” *J. Comput. Phys.*, pp. 307–326, 1986.

[84] SWAN, “SWAN Technical Documentation,” *Delft Univ. Technol. Netherlands*, 2007.

[85] R. Allard, W. E. Rogers, S. N. Carroll, and K. V. Rushing, “Validation Test Report for the Simulating Waves Nearshore Model (SWAN): Cycle III , Version 40 . 11,” p. 49, 2004.

[86] C. E. Greenwood, D. Christie, and V. Venugopal, “The Simulation of Nearshore Wave Energy Converters and their Associated Impacts around the Outer Hebrides,” *10th Eur. Wave Tidal Energy Conf. (EWTEC 2013)*, 2013.

[87] G. Newton-cross, “Implementation of wave energy converters in spectral wave models.”

[88] H. C. M. Smith, C. Pearce, and D. L. Millar, “Further analysis of change in nearshore wave climate due to an offshore wave farm: An enhanced case study for the Wave Hub site,” *Renew. Energy*, vol. 40, no. 1, pp. 51–64, 2012.

[89] A. K. Porter, “Laboratory Observations and Numerical Modeling of the Effects of an Array of Wave Energy Converters,” 2012.

[90] C. Chartrand and K. Ruehl, “Personal Communication.” 2015.

[91] G. Garcia-Medina, H. T. Ozkan-Haller, and P. Ruggiero, “Wave resource

assessment in Oregon and southwest Washington, USA," *Renew. Energy*, vol. 64, pp. 203–214, 2014.

[92] V. Venugopal and R. Nemalidinne, "Wave resource assessment for Scottish waters using a large scale North Atlantic spectral wave model," *Renew. Energy*, vol. 76, pp. 503–525, 2015.

[93] L. Liberti, A. Carillo, and G. Sannino, "Wave energy resource assessment in the Mediterranean, the Italian perspective," *Renew. Energy*, vol. 50, pp. 938–949, 2013.

[94] R. Alonso, S. Solari, and L. Teixeira, "Wave energy resource assessment in Uruguay," *Energy*, vol. 93, pp. 683–696, 2015.

[95] M. Folley and T. Whittaker, "Validating a spectral-domain model of an OWC using physical model data," *Int. J. Mar. Energy*, vol. 2, pp. 1–11, 2013.

[96] B. Robertson, "Wave Energy Assessments: Quantifying the Resource and Understanding the Uncertainty," 2016.

[97] L. H. Holthuijsen, A. Herman, and N. Booij, "Phase-decoupled refraction-diffraction for spectral wave models," *Coast. Eng.*, vol. 49, no. 4, pp. 291–305, 2003.

[98] E. Rusu, C. G. Soares, E. Rusu, and C. G. Soares, "Modeling Waves in Open Coastal Areas and Harbors with Phase-Resolving and Phase-Averaged Models," *J. Coast. Res.*, vol. 29, no. 6, pp. 1309–1325, 2013.

[99] M. Folley and T. Whittaker, "The adequacy of phase-averaged models for modelling wave farms," in *Proceedings of the ASME 2011 30th International Conference on Ocean, Offshore and Arctic Engineering*, 2011, pp. 1–9.

[100] B. Robertson, D. Clancy, H. Bailey, and B. Buckham, "Improved Energy Production Estimates from Wave Energy Converters through Spectral Partitioning of Wave Conditions," *Int. Soc. Offshore Polar Eng.*, p. 8, 2015.

[101] Delft University, "USER MANUAL SWAN - Cycle III version 41.01A," 2009.

[102] Delft University of Technology, "TECHNICAL DOCUMENTATION," 2006.

[103] J. Cruz, *Ocean Wave Energy*. 2008.

[104] A. Porter, K. Ruehl, C. Chartrand, and H. Smith, "Development and release of the open-source wave climate environment assessment tool SNL-SWAN," pp. 1–5,

2015.

[105] W. Bearman, J. Downie, and D. Obasaju, “Forces on cylinders in viscous oscillatory flow at low Keulegan-Carpenter numbers,” vol. 154, pp. 337–356, 1985.

[106] M. Gharib and A. Roshko, “The effect of flow oscillations on cavity drag,” *J. Fluid Mech.*, vol. 177, pp. 501–530, 1987.

[107] R. G. Dean and R. A. Dalrymple, *Water Wave Mechanics for Engineers and Scientists*. New Jersey: World Scientific, 2008.

[108] J. Ortiz, “The Influence of Mooring Dynamics on the Performance of Self Reacting Point Absorbers,” The University of Victoria, 2016.

[109] E. Luczko, H. Bailey, B. Robertson, C. Hiles, and B. Buckham, “Assimilating a time-domain representation of a wave energy converter into a spectral wave model,” *Int. Conf. Offshore Mech. Arct. Eng.*, pp. 1–10, 2016.

[110] Power Supply Engineering, “Executive Report on the Green Energy Study for British Columbia,” no. July, 2001.

[111] B. Robertson, “Ocean Wave Energy Generation on the West Coast of Vancouver Island and the Queen Charlotte Islands,” *Guelph Eng. J.*, no. 3, pp. 9–18, 2010.

[112] A. Cornett and J. Zhang, “Nearshore Wave Energy Resources, Western Vancouver Island, B.C.,” 2008.

[113] MacArtney Underwater Technology, “WEC Infrastructure Review,” 2016.

[114] J. Falnes and J. Hals, “Heaving buoys, point absorbers and arrays.,” *Philos. Trans. A. Math. Phys. Eng. Sci.*, vol. 370, no. 1959, pp. 246–77, 2012.

[115] J. Falnes, “Principles for Capture of Energy From Ocean Waves. Phase Control and Optimum Oscillation.,” 1997. [Online]. Available: http://www.waveenergy.civil.aau.dk/we_phd_course/2006/pdf/phcontrl.pdf.

[116] L. Marquis, M. Kramer, and P. Frigaard, “First Power Production figures from the Wave Star Roshage Wave Energy Converter,” *Int. Conf. Ocean Energy*, pp. 1–5, 2010.

[117] I. G. C. Ashton, L. Johanning, and B. Linfoot, “Measurement of the effect of power absorption in the lee of a wave energy converter,” *ASME 2009 28th Int. Conf. Ocean. Offshore Arct. Eng.*, pp. 1–10, 2009.

[118] S. Thomas, S. Weller, and T. Stallard, “Float Response within an Array: Numerical and Experimental Comparison,” *Proc. 2nd Int. Conf. Ocean Energy ICOE2008*, no. October, pp. 1–9, 2008.

[119] V. Stratigaki, P. Troch, T. Stallard, D. Forehand, J. Kofoed, M. Folley, M. Benoit, A. Babarit, and J. Kirkegaard, “Wave Basin Experiments with Large Wave Energy Converter Arrays to Study Interactions between the Converters and Effects on Other Users in the Sea and the Coastal Area,” *Energies*, vol. 7, no. 2, pp. 701–734, 2014.

Appendix

The author can be contacted for input files pertaining to the flat bathymetric bottom and field case simulations.